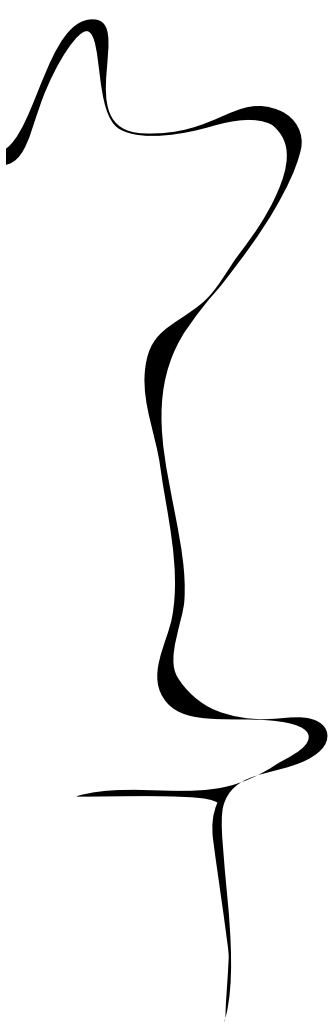


Frequency optimisation for damage identification using the Vibro-Acoustic Modulation method

Master Thesis

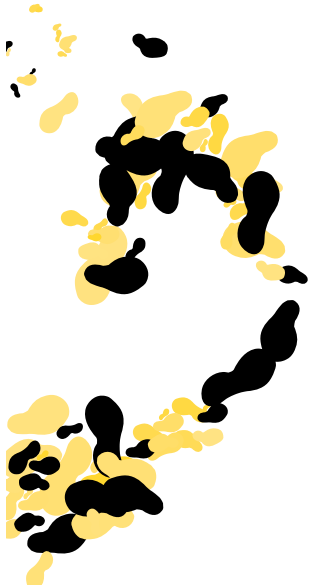


M. VENTERINK
s0190853

Date:
January 20, 2017

Examination committee:
prof. dr. ir. T. Tinga
dr. ir. R. Loendersloot
ir. J.S. Hwang
ir. J.P. Schilder

Document Number:
ET.17/TM.5790



Preface

This report is the result of my research for the Master Degree in Mechanical Engineering at the University of Twente. My master program in the faculty of Engineering Technology started by the chair Applied Mechanics but my final master assignment was carried out by the Dynamics Based Maintenance group.

Without the help of my supervisors it would not have been possible to finish my thesis. Richard Loendersloot and Jason Hwang helped me with their critical comments and insightful advises throughout my graduation project. Our discussions kept me going and I am very thankful for that. Not to forget Tiedo Tinga for his comments and advises. Then I would like to thank Axel Lok for his help on my experimental setup and Gert-Jan Nevenzel for the production of the composites plates at TPRC. Furthermore I would like to thank my fellow students from the 'MS3Bazen' room for the occasionally useful discussions and ofcourse the pleasant times.

Finally I would like to thank my family and friends for their support during the difficult times in 2016. Especially my girlfriend Pauline who has supported me to finish my master assignment and achieving my cycling goals at the same time.

Januari 2017, Enschede
Martijn Venterink

Summary

Composite aerospace structures are desired to have an extended service life and a reduction of maintenance costs without compromising safety. The presence and severity of possible damage has to be monitored to guarantee safety. Aerospace structures are especially sensitive to impact damage that results mostly in delaminations. The steady state Vibro-Acoustic Modulation (VAM-)method has shown to be a promising non-destructive technique for damage identification in a composite structure using two excitation frequencies: a low intense pump frequency (mostly a natural frequency) and a relative weak and high carrier frequency. Research on the influence of the carrier frequency selection, which is mostly done arbitrary, on the response signal modulations is however limited.

The main objective of this graduation assignment is to achieve an ideal combination of a pump and carrier frequency for a more efficient damage detection, localization and characterization on a composite with a delamination. The secondary objective is to explain the occurring signal modulations for different carrier frequencies.

Analytically derived nonlinear dynamic responses of a multi degrees of freedom system subjected to a two-tone forced harmonic, show the relation of amplitudes of the carrier, pump, higher harmonics and sidebands with the natural frequencies. These natural frequencies are separated into the global natural frequencies of the composite plate structure and the local natural frequencies of the delamination. The global and local eigenfrequencies of the composite plate are determined numerically such that the dimensions of the manufactured composite plate and its artificial delamination can be chosen.

Experimentally, the natural frequencies of the produced composite plate are also determined and a separation between local and global is made. The pump excitation with the expected clapping behavior that causes the most signal modulations is selected for the VAM-experiments, i.e. the delamination shows an opening and closing behavior by the operational deflection shape of the pump excitation. Finally the carrier frequency is varied with a constant carrier excitation amplitude.

Firstly, the VAM-method promises to be more effective in damage detection and localization when using a local natural frequency as the carrier. The modulations will increase more in the damaged location than in the undamaged location compared to using a global natural frequency as carrier. Secondly, the frequency modulation for varying carrier frequencies has shown to be very inconsistent. Therefore it is concluded that damage localization with amplitude modulation in the time domain is better than using the sidebands in the frequency domain, because sidebands are a function of both amplitude and frequency modulation. Finally, a framework has been considered for a practical application of VAM.

Samenvatting

Voor composiet structuren in de vliegtuigindustrie is het gewenst om een langere levensduur en een reductie van onderhoudskosten te hebben. De veiligheid mag niet in gevaar komen en daarom moet de aanwezigheid en heftigheid van mogelijke schade constant in de gaten gehouden worden. Composieten kunnen interne schades hebben die aan de buitenkant nauwelijks of niet zichtbaar zijn. Een delaminatie tussen twee lagen is een veelvorkomende schade in de vliegtuigindustrie ten gevolge van impact schade. De Vibro-akoestische modulatie (VAM-)methode is een veelbelovende niet-destructieve test techniek om zulke schade te identificeren in een composiet. Deze methode maakt gebruik van twee excitatie frequenties, een sterke en lage ‘pomp’ frequentie (meestal gelijk aan een eigenfrequentie) en een relatief zwakke en hoge ‘dragende’ frequentie. Het effect van de keuze van de dragende frequentie op de signaal modulaties is echter nog maar weinig onderzocht.

Het hoofddoel van deze afstudeeropdracht is om een betere combinatie van een pomp en dragende frequentie te vinden om zo een efficiëntere schade detectie, lokalisatie en karakterisatie te krijgen voor composieten met een delaminatie. Een subvraag van dit hoofddoel is het verklaren van de optredende signaal modulaties voor verschillende dragende frequenties.

Niet-lineaire dynamische responsies zijn analytisch afgeleid van een systeem met meerdere vrijheidsgraden die met twee harmonische krachten geëxciteerd wordt. Deze responsies tonen een relatie aan tussen de amplitudes van de pomp, de dragende, de hogere harmonische en de zogenaamde ‘sidebands’ met de natuurlijke frequenties van het systeem. Deze natuurlijke frequenties zijn vervolgens opgesplitst in de globale natuurlijke frequenties van de composiet plaat en de lokale natuurlijke frequenties van de delaminatie. Deze globale en lokale eigenfrequenties zijn eerst numeriek bepaald om zo vervolgens de afmetingen van de te maken composiet plaat en de bijbehorende delaminatie te kunnen bepalen. De daadwerkelijke natuurlijke frequenties van de geproduceerde plaat zijn vervolgens experimenteel bepaald, en een onderscheid is gemaakt tussen lokale en globale frequenties. Een pomp frequentie is vervolgens geselecteerd die het verwachte open en sluiten gedrag van de delaminatie veroorzaakt en die de meeste signaal modulaties veroorzaakt. Tot slot is de dragende frequentie gevarieerd met een constante excitatie amplitude.

Ten eerste is er geconcludeerd dat de VAM-methode efficiënter in het detecteren en lokaliseren van schade is wanneer er gebruik wordt gemaakt van een lokale natuurlijke frequentie als dragende frequentie. De signaal modulaties zullen heftiger zijn in het beschadigde gebied dan in de onbeschadigde gebieden. Ten tweede is er geobserveerd dat de frequentie modulatie voor verschillende dragende frequenties erg inconsistent is ten opzichte van de amplitude modulatie. Daarom is er ook geconcludeerd dat schade identificatie door middel van amplitude modulatie in het tijdsdomein beter is dan gebruik te maken van de zogenaamde ‘sidebands’ naast de dragende frequentie in het frequentie domein. Ten slotte is er een stappenplan gemaakt aan de hand van de resultaten in dit onderzoek, zodat VAM ook in de praktijk toegepast kan worden.

Contents

Preface	iii
Summary	v
Samenvatting	vii
Nomenclature	xi
1 Introduction	1
1.1 Composite structures	1
1.1.1 Damage categories	2
1.1.2 Damage types	2
1.1.3 Damage lay-out	3
1.1.4 Summary	4
1.2 Structural Health Monitoring	4
1.2.1 Techniques	5
1.2.2 Vibro-Acoustic Modulation (VAM)	6
1.3 Damage mechanisms and nonlinearities	7
1.3.1 Contact acoustic nonlinearity	7
1.3.2 Dissipative mechanisms	9
1.3.3 Summary	10
1.4 Goal of the study	10
1.5 Outline	11
2 Signal modulations	13
2.1 Modulation types	13
2.1.1 Amplitude modulation	14
2.1.2 Phase modulation	15
2.1.3 Frequency modulation	15
2.1.4 Differences between AM and FM	15
2.2 Nonlinearities causing AM and FM in VAM	16
2.3 Two-tone forced vibration of a nonlinear system	17
2.3.1 Quadratic displacement nonlinearity	18
2.3.2 Quadratic velocity nonlinearity	20
2.4 Selection of the excitation frequencies for VAM	21
2.4.1 The global eigenfrequencies of a composite plate	22
2.4.2 The local eigenfrequencies of the delamination	23
2.5 Signal extraction	25
2.5.1 Frequency spectrum	26
2.5.2 Signal demodulation procedures	27
2.6 Summary	29

3	Experimental work	31
3.1	Composite plate structures	31
3.1.1	Material	31
3.1.2	Production with the artificial delamination	32
3.1.3	Validation of the delamination	33
3.2	Experimental set-up	35
3.3	Experimental procedure	36
3.3.1	Global dynamic characterization	36
3.3.2	Local dynamic characterization	37
3.3.3	Vibro-acoustic modulation experiments	38
3.4	Experimental results of the dynamic characterization	40
3.4.1	Global results	40
3.4.2	Local results	41
3.4.3	Summary	43
4	Experimental results and discussion	45
4.1	Pump wave	45
4.1.1	Pump frequency	45
4.1.2	Pump amplitude	46
4.1.3	Pump wave selection	49
4.2	Carrier wave	49
4.2.1	Bandpass frequency spectra	50
4.2.2	Instantaneous amplitude	53
4.2.3	Instantaneous frequency	56
4.2.4	Carrier wave selection	58
4.3	Higher frequency ranges	58
4.4	Practical application	60
5	Conclusions and recommendations	63
5.1	Conclusions	63
5.2	Recommendations	64
	Bibliography	65
	Appendix A Frequency modulation	69
	Appendix B Perturbation Technique	71
	Appendix C Hilbert Transform	75
	Appendix D Hilbert-Huang Transform	77
	Appendix E Eigenfrequencies of a circular plate	79
	Appendix F Ultrasonic C-scans	81
	Appendix G Impedance Measurements	83
	Appendix H Dynamic characterization	85

Nomenclature

The Greek and Roman symbols, and the abbreviations used in this master thesis are categorized. Some symbols can represent multiple quantities, the exact meaning follows from the textual context. An overview of the most important abbreviations and symbols used in the present thesis is:

Abbreviations

AM	Amplitude modulation
BVID	Barely visible impact damage
C	Clamped
DOF	Degree(s) of freedom
FFT	Fast Fourier transform
FM	Frequency modulation
FRF	Frequency response function
HT	Hilbert transform
NDT	Nondestructive testing
NLR	National aerospace laboratories
ODS	Operational deflection shape
PM	Phase modulation
PZT	Piezo-electric transducer
SHM	Structural health monitoring
SS	Simply supported
VAM	Vibro-acoustic modulation

Greek symbols

β_{AM}	Amplitude modulation index	[-]
β_{FM}	Frequency modulation index	[-]
ϵ	Control factor for the nonlinear function	[-]
ν	Poisson's ratio	[-]
ρ	Density	[kg/m ³]
ϕ_{inst}	Instantaneous phase	[rad]
ϕ_p	Phase of the pump excitation signal	[rad]
ϕ_c	Phase of the carrier excitation signal	[rad]
ω	Frequency	[rad/s]
ω_p	Frequency of the pump excitation signal	[rad/s]
ω_c	Frequency of the carrier excitation signal	[rad/s]
ω_o	Natural frequency	[rad/s]
ω_{inst}	Instantaneous frequency	[rad/s]

Roman symbols

a	Distance between delamination and weldspot	[mm]
A_c	Carrier amplitude	[m]
A_p	Pump amplitude	[m]
A_{sb1}	Left sideband amplitude	[m]
A_{sb2}	Right sideband amplitude	[m]
A_{inst}	Instantaneous amplitude	[mm/s]
d	Distance between grid-point and edge	[mm]
D	Delamination	[-]
e	Distance between grid-points	[mm]
E	Young's modulus	[N/m ²]
F_c	Excitation carrier amplitude	[N]
F_p	Excitation pump amplitude	[N]
f	Frequency	[Hz]
f_{res}	Resolution frequency	[Hz/bin]
f_c	Carrier excitation frequency	[Hz]
f_p	Pump excitation frequency	[Hz]
f_s	Sampling frequency	[Hz]
f_{inst}	Instantaneous frequency	[Hz]
f_{global}^n	Global natural frequency	[Hz]
f_{local}^n	Local natural frequency	[Hz]
H_{Fv}	Frequency response function (mobility= velocity/force)	[(mm/s)/N]
H_{Vv}	Frequency response function (mobility= velocity/Voltage)	[(mm/s)/V]
H	Thickness of the plate	[mm]
H_2	Thickness of the delamination	[mm]
J_n	Bessel function of the first kind	[-]
L	Length of plate	[mm]
L_1	Length to delamination	[mm]
L_2	Length to delamination	[mm]
M_a	Amplitude modulation	[mm/s]
M_f	Frequency modulation	[Hz]
m	Mass	[kg]
n	Number	[-]
\mathbf{q}	Displacement vector	[m]
q_{bp}	Bandpass filtered displacement response	[m/s]
R	Delamination radius	[mm]
S_{Fv}	Cross-power spectral density (force - velocity)	[(Nmm/s)/Hz]
S_{Vv}	Cross-power spectral density (voltage- velocity)	[(Vmm/s)/Hz]
S_{FF}	Auto-power spectral density (force - force)	[V ² /Hz]
S_{VV}	Auto-power spectral density (voltage - voltage)	[N ² /Hz]
t	Time	[s]
V	Voltage	[V]
v_{vp}	Bandpass filtered velocity response	[m/s]
v	Velocity response	[m/s]

Chapter 1

Introduction

The selection criteria for using composites is to obtain a lighter and stiffer construction. Nowadays, composite structures are also desired to have an extended service life and a reduction of maintenance costs [1]. These demands contradict each other, making it difficult to get an optimal solution. A disadvantage of using composites is that the structure is more prone to (impact-)damage [2]. Non-destructive testing (NDT-)techniques are a promising technique for damage detection, especially Structural Health Monitoring (SHM). It has the potential to reduce maintenance costs because some SHM techniques are capable to detect damage early on in specific circumstances. The development of these SHM techniques are a widely discussed topic in the literature. They have mainly been applied to very different structures and this makes it very hard to compare all the different techniques. The Vibro-Acoustic Modulation (VAM-)technique shows to have great potential. Different VAM-methods already exist and one will be the topic of this thesis.

1.1 Composite structures

Composites are used in many lightweight engineering structures due to their high specific strength, low density and their resistance to fatigue and corrosion. Composites also have flexibility in design. This flexibility allows for the production of complex shapes such as curved panels and skin-stiffener structures. Applications of composites are mostly in demanding environments, such as: wind turbines, space and aircraft structures but also high-end sports, like motor-racing and cycling. In particular the use of composites in the aerospace industry is advancing very fast, even though the application in this industry is very conservative.

A composite consists of a matrix and reinforcements. The matrix consists of a polymer when applied to aerospace structures. The reinforcement improves the composite's overall properties but will result in anisotropic properties. Typical materials for fiber reinforcements in polymer composites are glass and carbon, but also high strength polymers such as aramid and high temperature resistant silicon-carbide could be used as fibers.

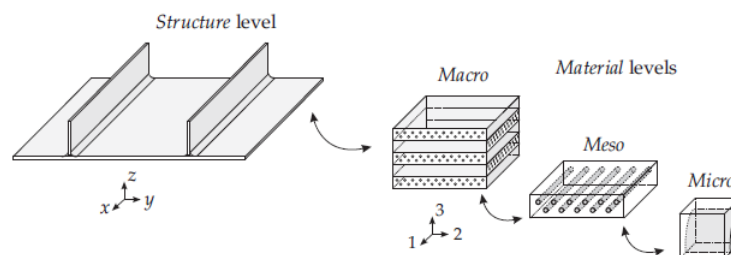


Figure 1.1: The multi-scale levels related to fiber reinforced plastics as in [3].

The fibers, the matrix, an individual layer and the stacked layers all behave on a different scale. The scale of the fibers and the matrix are of a lower level than the scale of an individual layer. A laminate is build from different layers and is therefore of a higher scale. The structure level is the highest level. An complete overview of these different levels is given in figure 1.1 and can be used to indicate where a specific damage can occur.

1.1.1 Damage categories

The disadvantage of using composite materials in aerospace applications is that these structures are more sensitive to damage than metals. Shock, impact or repeated cyclic stresses can cause damages to composites but also to the widely used aluminum structures. Aluminum is very sensitive to repeated cyclic stresses since it does not have a distinct fatigue limit. Composites are especially sensitive to impact damage [4]. Damages in composite aerospace structures can be categorized according to their severity [5]:

1. Allowable damage that may go undetected by scheduled or direct field inspection, for example allowable manufacturing defects, but also non-allowable damage: Barely Visible Impact Damage (BVID), e.g. caused by debris or hailstones.
2. Damage detected by scheduled or directed field inspection at specified intervals, e.g. exterior skin damage or interior stringer blade damage.
3. Obvious damage detected within a few flights, e.g. accidental damage to lower fuselage or a lost bonded repair patch.
4. Discrete source damage immediately known by the pilot limiting flight maneuvers, e.g. rotor disk cut through fuselage or severe rudder lightning damage.
5. Severe damage created by anomalous ground or flight events.

The first category contains damage that can easily go undetected. The other categories all contain damage that will likely be detected by a scheduled or a direct field inspection and most of the time can be clearly visual spotted. Damages in the categories 1 to 4 have to be taken into account during aircraft design and for the damages of category 2 to 5 repair scenarios are required. The first category is the most interesting one because damage from this category is not directly harmful for the functioning of an airplane. However timely detecting damage in this category results in less maintenance costs before it expands into a severer damage category.

1.1.2 Damage types

A damage in a composite structure can have different origins. The type of damage can be categorized in the following three groups [5]:

- Accidental damage
- Fatigue damage
- Environmental damage

From these three groups accidental damage is the biggest hazard for composite aerospace structures. An example of an accidental (impact) damage which led to catastrophic results is the Space Shuttle Columbia [6]. During take-off, a carbon composite tile on the leading edge of the wing of the space shuttle fractured when impacted by a piece of foam. When the vehicle re-entered the Earth's atmosphere on 1 February 2003, it disintegrated killing all seven crew members. Damage inflicted by impact is a big and common problem for aerospace structures, the damage patterns are very distinctive. In metals the impact energy is dissipated through elastic and plastic deformations and the structure still retains a good margin of structural integrity. In fiber reinforced composite materials however, the damage is usually more extensive than what can be seen on the surface. With increasing damage, the remaining load capacity will decrease. This determines the safe life of a structure.

Different damage types can occur which are unknown to homogeneous materials. Failure can happen on the macro, meso and micro scales which are mentioned in figure 1.1. Delaminations, matrix breakage, debonding, fiber failure are shown to be the main failure modes of impact damage [2]. These damage types are likely to cause severe degradation of the mechanical properties and critical failure of the part/structure if they are not discovered in time.

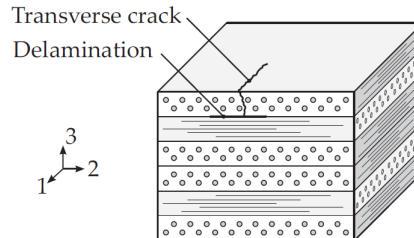


Figure 1.2: Schematic representation of transverse crack and delamination in a $[0/90/0]_s$ laminate [3].

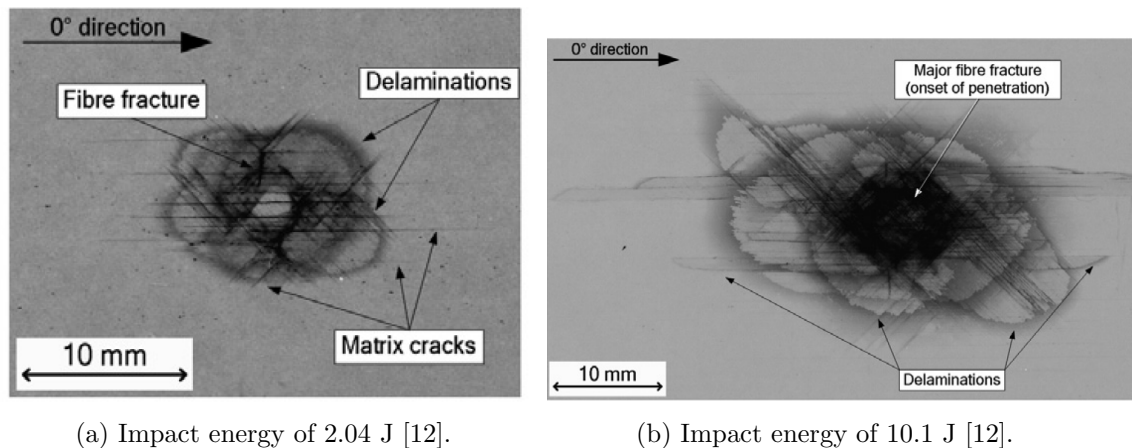
A schematic representation of a delamination and a matrix crack is given in figure 1.2. Delaminations (with matrix cracks present) are the most discussed failures of a composite in the literature [7, 8]. Laminated composites are especially susceptible to delamination owing to their weak transverse tensile and inter-laminar shear strengths as compared to their in-plane properties.

1.1.3 Damage lay-out

Failure of composite structures is quite complex and usually involves the combination of several failure modes. All kinds of different inflicted damages on composites are discussed in the literature [4]. The focus in this study will be on the high-velocity low-mass impact damage that most likely will cause BVID with delaminations. Which failure modes are present in a test-specimen depends on the technique that is used to apply the damage. An impact test will result in more realistic damage and will likely contain different kinds of failure modes over one or multiple layers [2].

An artificial damage can be created to control the damage such that only a specific failure mode is present in the specimen. For example inserting a piece of Teflon between two layers in the production process will only contain one specific delamination between two layers in the test-specimen [3, 9, 10]. If the Teflon is inserted before consolidating the structure in the autoclave, the Teflon will evaporate because of the high temperature. This artificial delamination will differ from an actual delamination. Such a real life delamination can still have fibers crossing in the delamination, the artificial delamination will not have those fibers crossing in the delamination. The shape of the delamination will be very well controllable with this technique.

Another option that can inflict damage (delamination) in a controllable situation is a three point bending loading technique. This is used in a different study to create damage in a composite plate [11]. Different loadings are used for different test-specimens. Delaminations and matrix cracks are created in each specimen with a different damage severity. This already demonstrates that the inflicted damage is not that controllable as in the previous discussed artificial delaminations.



(a) Impact energy of 2.04 J [12].

(b) Impact energy of 10.1 J [12].

Figure 1.3: Two impact tests with a different impact energy, as in [12].

A final and the most realistic option representing impact damage for creating a delamination in a test-specimen is an impact test. An example of damage on a carbon/epoxy plate which is created with an impact test is studied by Aymerich and Staszewski [12]. A drop-weight impact testing tower with a 2.2 kg impactor and a hemispherical indenter of 12.5 mm diameter was used. Multiple impacts are prevented and the plate was simply supported on a steel plate. The impact was subjected in the middle of the plate and different impact energies of 2.04 J and 10.1 J were used to introduce different levels of damage in the laminated panel. Both scenarios are shown in figure 1.3(a) and 1.3(b). Damage induced by the 2.04 J mainly consisted of multiple delaminations developing along several interfaces across the thickness, together with a dense network of 0 and 45 degrees matrix cracks. Short fiber fracture paths are also noticed on the contact area which was struck by the indenter. For the 10.1 J impact test, extensive delaminated areas, major fiber fracture on both sides and a much larger indentation are observed. This energy level approached the laminate penetration threshold. Similar findings can be seen in [2] but also a more peanut shaped delamination that will be formed with higher impact energies. The shape of the delaminations (and the presence of other damages) with impact tests will be no so good controllable as with an artificial delamination.

1.1.4 Summary

Composite structures are used in many applications for their low density, high stiffness and their flexibility for design. However their build-up from separate fibers in a polymer matrix and from different layers, makes a composite prone to damage. Composite aerospace structures are very sensitive to impact damage which can easily result in BVID. These BVID's most of the time contain delaminations since impact during flight consist of low-mass and high-velocity impact. An actual damage scenario on an airplane structure can be simulated on a test specimen in a laboratory. An artificial damage results in a clean delamination such that the behavior can be predicted analytically. A more realistic damage scenario can be created with an impact test but this method will most likely result in a complicated damage scenario and is therefore difficult to simulate analytically or numerically.

1.2 Structural Health Monitoring

Non-destructive testing (NDT)-techniques are applied to detect the previously discussed damages. It is a big research area that focuses on the detection of damage in composites, but also in other materials. Conventional NDT-techniques are still very labor-intensive, time consuming and often very expensive. Examples are visual inspection, X-ray radiography, electromagnetic testing and ultrasonic testing. A promising alternative to complement these NDT's, is Structural Health Monitoring (SHM). SHM is the multidisciplinary process of implementing a strategy for

damage identification in a way that nondestructive testing becomes an integral part of the structure. SHM however will still be an expensive process, since experts are needed to implement it. The SHM process involves the observation of a system over time using periodically sampled response measurements from an array of sensors, the extraction of damage-sensitive features from these measurements, and the (statistical) analysis of these features to determine the current state of system health. For long term SHM, the output of this process is periodically updated information whether the structure can keep performing its intended function. SHM is used for rapid condition screening and aims to provide reliable information regarding the integrity of the structure in a limited amount of time. Summarizing, the diagnostic part of the SHM process can be divided in a four-step process:

1. Operational evaluation
2. Data acquisition
3. Feature extraction
4. Classification

1.2.1 Techniques

A large research area in the literature is dedicated to techniques for SHM that use the dynamics of a structure, to be more specific: they use structural vibrations [13]. Next to dynamic techniques, also optic, electric, magnetic and electromagnetic techniques can be employed for damage identification purposes, see figure 1.4. Different methods in the time, frequency and modal domain can be distinguished for structural vibration techniques, see figure 1.4. Modal methods use for example the change in natural frequencies or mode shapes to detect, localize and estimate the size of present damage(s). The vibrational linear methods have shown good applicability to detect or sometimes localize the damage but most of these methods still struggle to predict the size of the damage. Small damages are hard to detect with these methods which use relatively low frequencies and thus long wavelengths.

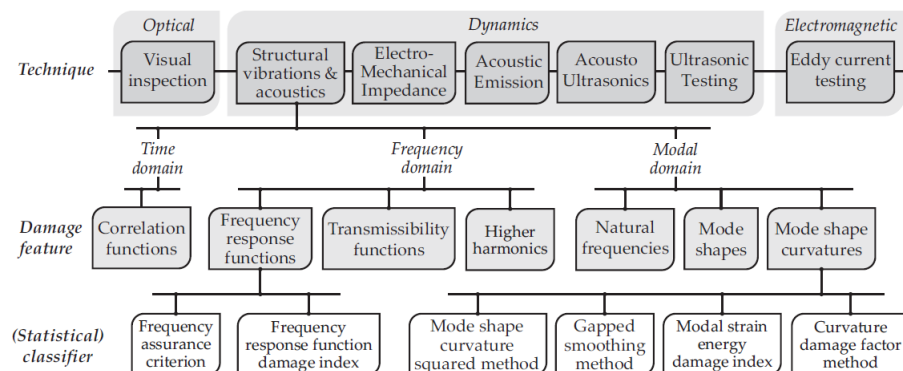


Figure 1.4: A summary of the wide range of damage identification approaches [3]

Traditional vibration based methods typically rely on linear system descriptions, neglecting possible nonlinearities [14]. Nonlinear damage identification methods show to be more promising [3]. Nonlinear features that are used multiple times for damage identification are for example the generation of sub-/higher harmonics in the structural response [15, 16]. These nonlinear methods rely on the fact that nonlinearities will be more present in a damaged structure than a pristine one. Localizing and estimating the severity of the damage is already done successfully [3, 17]. The nonlinear Vibro-Acoustic Modulations (VAM) for the detection, localization and characterization of impact damage in a composite structure is currently a promising nonlinear damage identification method [8]. The understanding of the occurring signal modulations is however still limited. Modulation occurs when a high-frequency wave is effected by a more intense

low-frequency vibration in the presence of structural nonlinearities. The amplitude and/or frequency of the excitation high-frequency wave can be modulated by the low-frequency vibration and they will therefore be fluctuating in the time domain. The use of these modulations for damage detection makes VAM a non-baseline technique that has the promising capabilities of verifying the presence of damage, determining the location of damage and estimating the severity of the damage. The focus of this master thesis will therefore be on this VAM-technique.

1.2.2 Vibro-Acoustic Modulation (VAM)

The nonlinear vibro-acoustic modulation (VAM)-technique is discussed a lot in the literature, an overview is given in [8]. The VAM-technique is also referred to as the nonlinear acoustic modulation method, the combination-frequency method and as the nonlinear wave modulation spectroscopy [10]. The VAM-technique is already successfully applied to a lot of different structures and materials, even on a human trabecular bone [18]. The VAM-technique relies on a standing wave field, spanning the whole specimen. A weak high-frequency ultrasonic wave ('carrier') is applied simultaneously on the structure together with the relatively strong low-frequency ('pump'). The pump signal will excite the structure, and consequently also effect the damage. The more sensitive carrier signal is used to excite the damage locally. A linear system without nonlinearities will give a response with only the two fundamental frequency components present in the frequency response spectrum. When there is damage present in the structure, a nonlinearity, the response will contain more frequencies than only the two original signals. The two excitation frequencies will interact and this will result in modulation of the carrier signal by the pump signal in amplitude, frequency or both. The occurrence of amplitude and frequency modulations are analytically proven for some nonlinearities [3, 19]. When there is damage present, sidebands around the carrier frequency and higher harmonics will be noticed in the response signal because of these nonlinearities. A more extensive literature review is done by the present author [20].

Frequency and time domain

The output of the VAM-method can be analyzed in the frequency and time domain. The frequency domain is most commonly used, however the time domain shows to be more promising [3]. An overview of the current research state of the VAM-method separated in different aspect by the frequency domain, time domain and the occurring signal modulations can be summarized as follows:

- Frequency domain
 - Sidebands around the carrier frequency in the output spectrum can be used as damage identifiers.
 - Sidebands coinciding with a resonance frequency increase in amplitude [21].
 - The central carrier peak is related to the presence, type and severity of damage and can be used as a damage quantifier. However the amplitude modification of this central carrier peak does not always show the same behavior and therefore the damage quantifier is not consistent [11].
 - A damage quantifier based on sideband amplitudes is investigated but is not sensitive enough for a lot of carrier frequencies [11].
 - Sidebands containing frequency modulation together with amplitude modulation do not give a proper indication of the severity of the damage [21]. The problem is that sidebands consisting of amplitude and frequency modulations cannot be separated in the frequency domain.
 - A variation of the input carrier and pump frequency has a lot of influence on the output frequency spectrum. Especially the choice of carrier frequency is important for the sensitivity of the VAM-technique to damage but research on the selection of the carrier frequency is very limited.

- Time domain
 - Analytically, only amplitude modulations are expressed for a quadratic displacement non-linearity using a perturbation technique based on a power series [3].
 - Numerically, amplitude and frequency modulations are shown to occur for different nonlinearities but only for a simplified single degree of freedom system [3].
 - Experimentally, amplitude modulations are shown to be sensitive to the damage location [3]. Frequency modulations do not contribute to damage identification.
 - Most studies consider traveling waves [8], however Ooijevaar’s study considers a steady state situation for his VAM-method in the time domain [3].
 - The physical mechanisms that produce amplitude (or frequency) modulation are not understood [8].

1.3 Damage mechanisms and nonlinearities

The physical mechanisms that possibly cause the signal modulations are briefly discussed in the literature study review by the present author [20]. Nonlinearities are categorized in non-classical and classical [8]. The classical nonlinear acoustics uses the theory of elasticity. This theory assumes homogenous materials and due to fatigued or damaged materials (inhomogeneities), nonlinearities in the waves arise. The nonlinear stress-strain relation leads to distortion of the wave and the generation of higher harmonics in the signal response spectra.

The mechanisms inducing the non-classical nonlinear behavior of a damaged structure are often very complex [22]. The amplitudes of the higher harmonics do not decay as fast as in the classical case and there are mostly higher orders present in frequency spectra. The non-classical nonlinearities are much stronger. Examples of mechanisms that are responsible for these non-classical nonlinearities are: dissipative mechanisms, contact acoustics, the Luxembourg-Gorky effect and hysteretic behavior. These mechanisms result in considerable response signal nonlinearities that can be observed for damage detection in VAM. The nonlinear contact dynamics is shown to be the (most) common mechanism that causes the modulation of acoustic waves [3, 12]. Therefore the focus of this thesis will be primarily on the contact acoustic nonlinearities.

1.3.1 Contact acoustic nonlinearity

This type of contact is caused by the inter-facial (rough) surfaces subjected to vibrations with a large amplitude [23]. A delamination can be considered as two separate elastic surfaces. In the most simplified one-dimensional case the delamination can be treated as a spring with a nonlinear stiffness. An elastic wave applied to the structure causes the surfaces to be pressed together in the compression phase and separated in the tensile phase, see figure 1.5. The carrier wave is free to vibrate in the open state, see figure 1.5(b) and is compressed in the closed state, see figure 1.5(c). The resulting amplitude modulation M_a is illustrated in figure 1.5(a). A realistic contact mechanism can be explained by ‘clapping’ or ‘rubbing/kissing’ behavior [3]. These two types can be seen as the opening and closing of the damage but also include friction, adhesion and thermo-elasticity [24, 25].

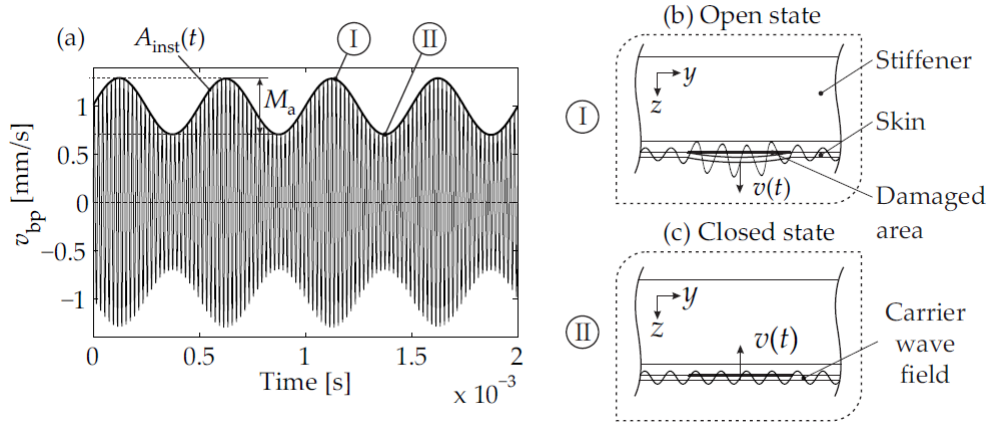


Figure 1.5: A bandpass filtered velocity response (a) with clear amplitude modulation effects A_{inst} . The opened state (b) and closed state (c) of the delamination are clearly illustrated and highlighted in (a). The open delamination (b) is free to vibrate, whereas the carrier amplitudes are compressed in the closed state (c). This simplified and schematic explanation can be found in [3].

Clapping

The clapping nonlinearity is due to asymmetrical dynamics of the contact stiffness. Clapping can be seen as impacts between the damaged surfaces that are not as smooth as compared to the simplified bi-linear stiffness model [25, 26]. The frequency spectrum of the nonlinear vibrations contains odd and even higher harmonics. The contact stiffness is apparently higher in a compression phase than that for the tensile phase when the crack is only assumed to be supported by the edge-stresses and as soon as the contact surfaces lose contact, the threshold of clapping is achieved. The latter can be seen in figure 1.6(b), higher excitation amplitudes only show the clapping behavior. An opening, closing and contact phase can be separated during the excitation of a lower harmonic frequency [3], see figure 1.6(b) for an example of these three phases in a phase portrait of a clapping mechanism.

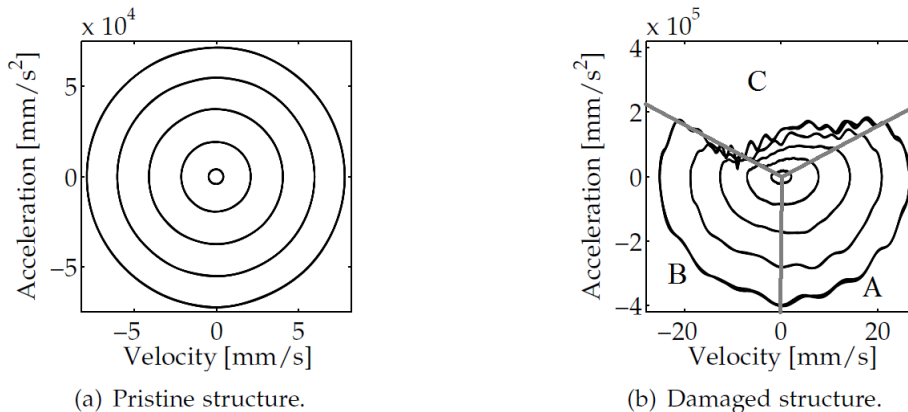


Figure 1.6: Phase portrait for a clapping mechanism on a damaged and pristine structure when excited with the 4th bending mode with 5 different amplitudes on a skin-stiffener structure in the same location [3]. The capitals refer to the opening (A), closing (B) and contact (C) phase.

These physical phenomena that can be concluded from the observations are that the amplitude modulations have the frequency of the pump excitation signal [3]. During the open state the skin is allowed to vibrate by the carrier frequency. In the closed state the amplitude of the vibration is expected to be smaller. As a result the high-frequency carrier wave predominantly experiences periodic modulations of the amplitude. Another observation on clapping in the study by Ooijevaar is that the skin starts to behave nonlinearly when the skin and stiffener are

approaching each other [3]. This contact phase can also be seen in figure 1.6(b). The skin-stiffener interaction is considered as the most likely reason why the modulation effects develop. The clapping mechanism will be triggered when the damage is symmetrically oriented between two nodal points of the operational deflection shape.

Rubbing/Kissing/Rolling

The rubbing (or kissing) contact also consists of the delaminated faces moving forced by the applied load and is less discussed in the literature than the clapping mechanism. In the study by Ooijevaar also the rolling behavior is investigated [3]. Phase portraits of the damaged and pristine structure for different excitation amplitudes can be seen figure 1.7 [3]. The phase portrait is overall smoother and the amount of high frequency scattering is smaller. The wrinkles at the zero crossings of the acceleration are the indication of a rolling motion. This rolling/kissing/rubbing mechanism will be excited when the damage is aligned off-center between two nodal points of the operational deflection shape.

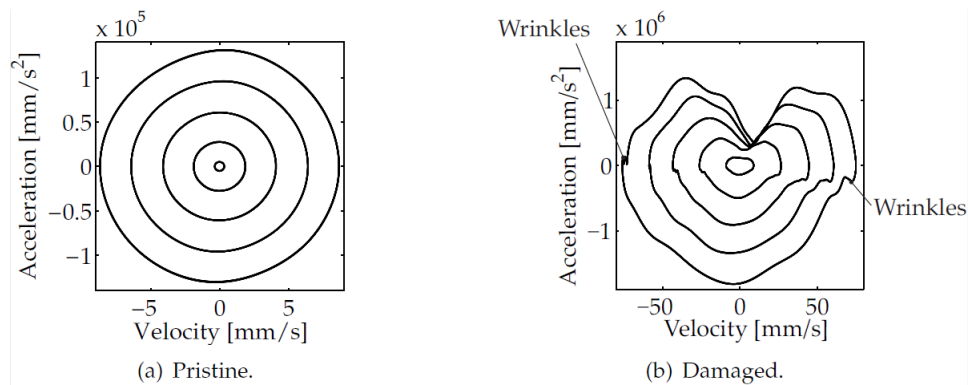


Figure 1.7: Phase portrait for a kissing mechanism on a damaged and pristine structure when excited with the 6th bending mode with 5 different amplitudes on a skin-stiffener structure in the same location [3].

1.3.2 Dissipative mechanisms

Klepka et al. [27] show three different damage behaviors for a fatigue cracked aluminum plate that is commonly applied in aircrafts, see figure 1.8. Opening and closing of the crack is not noticed in every VAM-test (Mode-1), however signals modulations are noticed in every scenario. So the crack does not have to be open to cause signal modulations, but the rate of modulation intensity increases when the crack is opened and closed. This experimental study also shows that energy dissipation is a major mechanism associated with vibro-acoustic modulations.

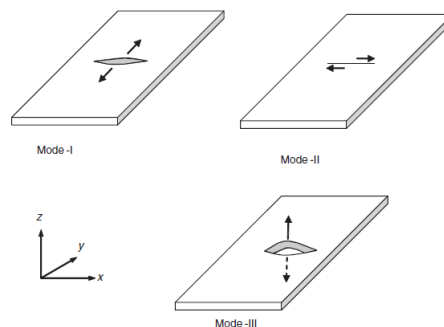


Figure 1.8: Different crack modes of an aluminum plate, as in [27].

Another study on a composite plate by Klepka et al. [17] showed that the movement of delaminated plies enhances nonlinear effects. This behavior is particularly observed when weaker

vibration modes and smaller excitation amplitudes are used. When the in-plane motion of delaminated plies is involved, relatively small amplitude excitation levels lead to relatively strong nonlinearities. When the delaminated plies produce the out-of-plane motion, damage related nonlinearities are much weaker. The mechanism of higher harmonics generation due to damage is associated with dissipation (friction and/or hysteresis) rather than with elasticity, because cracks do not have to be fully opened for modulations to occur.

Meo et al. [28] show that nonlinear material behavior caused by hysteresis is responsible for the signal modulations. Dissipative mechanisms seem also to be the mechanism that could explain the signal modulations on a human trabecular bone [18].

1.3.3 Summary

It is difficult to get a clear understanding about the physical mechanisms that explain the acoustic modulations. A lot of different materials, structures and input signals are used. Damage behaviors that cause the signal modulations could possibly be very different between other materials and/or structures. For example a T-stiffener in the neighborhood of a delamination will greatly enhance the stiffness on one side of the delamination [3]. Then again it can be concluded that a damage does not have to show opening and closing behavior for modulations to occur, even if opening and closing behavior amplifies the modulations [27]. Dissipation has lately been appointed as the main contributor for signal modulations together with contact acoustic nonlinearities. The problem of understanding the physical mechanisms is that similar nonlinear effects can be caused by different physical mechanisms and vice versa, even though different nonlinearities cause different higher harmonics in the frequency spectrum [25].

1.4 Goal of the study

Different pump and carrier frequencies are likely to give totally different response signals. Even though the selection of these frequencies for a structure with an unknown damage size or type is almost impossible, more insight on the effects of choosing a certain input frequency will contribute to a better functioning VAM-method. The selection of a carrier frequency does have a lot of influence on the acoustic modulations and therefore on the sensitivity of the VAM-method. A better understanding of the consequences on choosing such a carrier frequency will result in a better applicable SHM technique.

The steady state VAM-method of Ooijevaar [3] has shown to be more promising than the VAM-methods that use traveling carrier waves. These more traditional methods use sidebands for damage identification. The steady state VAM-method of Ooijevaar [3] focuses on the modulations in the time domain to localize damage. Therefore the present master thesis will mainly focus on the work of Ooijevaar [3] but also takes the modulation effects in the frequency domain into account. The research question of this study is formulated as follows:

How can an optimal selection of the pump and carrier frequency be achieved for efficient damage identification using VAM and can the obtained modulations be understood?

The goal will be to improve the steady state VAM-method by getting more insight on the selection of the carrier frequency. A composite plate with an artificial damage will be created such that damage behavior and the dynamic properties can be more easily predicted compared to an impact damage. Answering the following research questions will help by achieving the main goal:

1. How can amplitude and frequency modulations be expressed analytically?
2. How can amplitude and frequency modulations from a quadratic velocity and a displacement nonlinearity be expressed analytically?
3. Can the local natural frequencies of the delamination be separated and used for the carrier frequency selection?

4. What are the differences in the frequency spectrum for varying pump and carrier excitations and different spatial points?
5. What are the different modulations in the response signal for varying carrier frequencies and varying spatial points?
6. How can the (possible) differences in signal modulations be explained?
7. How do the results relate to the obtained results from Ooijevaar [3]?

Delimitations

The VAM-method is still a relatively new SHM technique and a lot is still unknown. Therefore not every aspect can be considered in this master thesis. The following aspects will not be considered:

- The physical mechanisms that can explain the modulations.
- Variation of the excitation carrier amplitude.
- Damage quantification and localization.
- A (detailed) numerical model of the damaged structure with the VAM-method.

1.5 Outline

In this chapter, the different studies on the VAM-technique were discussed. The research on varying the carrier frequency is discussed briefly together with the physical mechanisms responsible for the modulations. More information can be found in the previously executed literature review [20]. Chapter 2 discusses the theoretical descriptions of modulations in a general way. Two different systems with a 2-tone forced excitation and a velocity or displacement nonlinearity are solved and their response signal is discussed. To analyze the modulated response signals, a signal decomposition approach (and a FFT) is applied lastly in chapter 2. The obtained instantaneous characteristics can be used to obtain the amplitude and frequency modulation. Chapter 3 discusses the fabrication of the composite plate structures, the experimental setup and the experimental process with 3 different steps. Chapter 4 will show the results of the VAM-experiments and will discuss the obtained results. Possible explanations are given and they are also compared with different studies, especially with the steady state VAM-method of Ooijevaar [3]. Finally, chapter 5 will forward the conclusions and give some recommendations for further research.

Chapter 2

Signal modulations

The severity of the modulations is dependent on the choice of the pump and carrier frequency but also on the type of damage(behavior). The type of nonlinearities that cause the signal modulations is dependent on this type of damage(behavior) that is present in the structure. The approach on studying the signal modulations analytically and numerically is already done briefly in [3, 21]. It has been shown by Ooijevaar [3] for a simplified approach that amplitude modulations are amplified when the carrier and pump frequency are equal to a natural frequency. In this chapter the amplitude and frequency modulations are first described analytically. With these expressions the different modulations can be better understood and recognized in the response of a simplified nonlinear multi-DOF system with two forced vibrations. This response signal is further investigated and expanded to multi-DOF compared to the previous works in [3, 21]. This is followed by a signal decomposition approach to extract the instantaneous amplitude and frequency from the modulated (carrier) response. This approach is used in the experimental part. Since the choice for the carrier and pump frequencies is dependent on the natural frequencies of the structure, these are also determined theoretically in this section. The eigenfrequencies and mode shapes of a pristine composite plate are determined with ANSYS. The eigenfrequencies and mode shapes of the locally delaminated surface are estimated using analytical derivations of a circular plate with varying boundary conditions.

2.1 Modulation types

Modulation is the process of varying one or more properties of a periodic waveform called the carrier signal. This process is done actively with radio signals, where signal modulation is used to transport information. The process that creates the modulations can also be passive, the VAM-technique uses this as a damage feature. Nonlinearities in the vibrating structure caused by a damage behavior, could result in the modulation of the carrier signal by the pump signal. In telecommunications, the modulating pump signal contains information which will be transmitted onto the carrier signal. The main modulation types are amplitude modulation (AM) and angle modulation. The latter can be divided into frequency modulation (FM) and phase modulation (PM). In each of the three modulation types, the property (amplitude, frequency or phase) of the carrier signal is varied in accordance with the amplitude of the pump signal. Phase modulation is not used in any VAM-method since there has no relation be found to the damage. However in the work by Ooijevaar [3], a phase difference between different spatial points and between different excitation carrier frequencies has been observed. Therefore phase modulation will also be discussed briefly. Note that the signal modulation discussed in this section are forced upon the carrier signal as is the case in telecommunications.

2.1.1 Amplitude modulation

When considering a carrier wave of a frequency ω_c , a phase ϕ_c and an amplitude A_c , the time dependent displacement function $q_c(t)$ describing carrier wave can be expressed as:

$$q_c(t) = A_c \cos(\omega_c t + \phi_c) \quad (2.1)$$

The carrier amplitude will be multiplied with $(1 + q_m(t))$, which represents the (active) amplitude modulation and the time dependent displacement function $q(t)$ describing the amplitude modulated signal can be expressed as:

$$q(t) = A_c(1 + q_m(t)) \cos(\omega_c t + \phi_c) \quad (2.2)$$

When the modulating signal $q_m(t)$ (pump wave) is a sinusoid with a pump frequency ω_p , a pump amplitude A_p and a pump phase of ϕ_p the signal will be become:

$$q(t) = A_c(1 + A_p \cos(\omega_p t + \phi_p)) \cos(\omega_c t + \phi_c) \quad (2.3)$$

Equation (2.3) can be rewritten using trigonometry as:

$$q(t) = A_c \cos(\omega_c t + \phi_c) + \frac{A_c A_p}{2} [\cos((\omega_c - \omega_p)t + \phi_c - \phi_p) + \cos((\omega_c + \omega_p)t + \phi_c + \phi_p)] \quad (2.4)$$

In the frequency spectrum, the amplitude modulated carrier signal produces an output signal with a carrier frequency f_c and the two adjacent sidebands $f_c \pm f_p$. Note that only two sidebands are displayed for this case and that the pump signal is not present in the response since it is, in this signal modulation example, only used for varying the amplitude (and not actively excited on a structure).

The AM modulation index is a measure based on the ratio of the modulation of the response frequency signal to the level of the unmodulated carrier. So the AM modulation index β_{AM} can be defined as:

$$\beta_{AM} = \frac{q^{\max}(t)}{A_c} = \frac{A_p}{A_c} \quad (2.5)$$

An AM modulation index of $\beta_{AM} = 0.5$ results in a carrier amplitude which varies 50% above and 50% below its unmodulated level, see figure 2.1(a). The carrier signal is 5 kHz with an amplitude of 1 m/s and the pump signal is 500 Hz with an amplitude of 0.5 m/s for 50% modulation and 1.5 m/s for 150% modulation. The amplitude modulation of 150% is shown in figure 2.1(b).

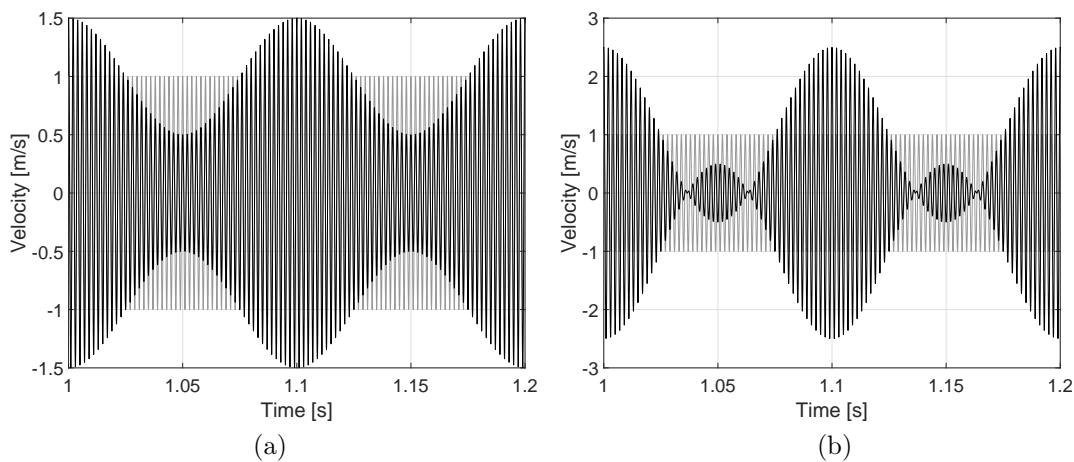


Figure 2.1: 50% Amplitude modulation (a) and 150% Amplitude modulation(b). The unmodulated signal is shown in light gray with a constant amplitude of 1 m/s.

2.1.2 Phase modulation

Phase modulation (PM) is closely related to frequency modulation (FM) and is often used as an intermediate step in transmitting radio waves to get frequency modulation. A carrier signal which is modulated in phase by $m(t)$ can be expressed as:

$$q(t) = A_c \cos(\omega_c t + m(t) + \phi_c) \quad (2.6)$$

This shows how $m(t)$ modulates the phase. As previously mentioned PM is closely related to FM, $m(t)$ has influence on the instantaneous frequency and instantaneous angle of the carrier signal. From PM the carrier frequency modulation (FM) is given by the time derivative of the phase modulation, see appendix A. The instantaneous angular frequency of the modulated signal is defined as:

$$\omega(t) = \frac{d}{dt}[\omega_c t + m(t) + \phi_c] = \omega_c + \frac{d(m(t))}{dt} \quad (2.7)$$

2.1.3 Frequency modulation

Frequency modulation (FM) is a specific case of phase modulation (PM). The time dependent displacement function $q_c(t)$ describing carrier wave can be expressed the same as in equation (2.1):

$$q_c(t) = A_c \cos(\omega_c t + \phi_c) \quad (2.8)$$

The carrier signal will be modulated by the pump amplitude A_p and pump frequency ω_p . The total response of the modulated signal can be expressed for a simplified case with only two sidebands as:

$$q(t) = A_c \cos(\omega_c t) - \frac{k_f A_c A_p}{2\omega_p} [\sin((\omega_c - \omega_p)t + \phi_c - \phi_p) + \sin((\omega_c + \omega_p)t + \phi_c + \phi_p)], \quad (2.9)$$

The total derivation can be found in appendix A. The frequency modulation index β_{FM} is defined as:

$$\beta_{FM} = \frac{k_f A_p}{\omega_p} \quad (2.10)$$

However equation (2.9) only holds for a very small frequency modulation index β_{FM} , more sidebands have to be taken into account to get a proper representation of the frequency modulated signal. ‘Chownings’ complete version of frequency modulation is as follows [21]:

$$q_{FM}(t) = J_0 A_c \cos(2\pi f_c t) + \sum_{n=1}^{\infty} (-1)^n J_n A_c [\cos((2\pi(f_c - n f_m)t) - \cos(2\pi(f_c + n f_m)t))], \quad (2.11)$$

in which $J_n(\beta_{FM})$ ($n = 0, 1, 2, 3, \dots$) refers to the Bessel functions of the first kind for the desired β_{FM} . These Bessel functions of the first kind are the solutions of the Bessel differential equation and are not in the scope of this thesis.

The signal $q_{FM}(t)$ is a spectrum of a sinusoidal signal multiplied by a constant (Bessel function). The FM spectrum consists of a carrier response plus an infinite number of sideband components at frequencies $f_c \pm n f_m$ ($n = 1, 2, 3, \dots$). To get a precise representation of the FM signal in the time domain, a wide range of frequencies has to be included in the expression of the frequency modulated signal.

2.1.4 Differences between AM and FM

The differences between AM and FM are in the amplitude of the central carrier response and in the amplitudes of the corresponding sidebands. The relative amplitude of the spectral components of a FM signal depend on the values of $J_n(\beta_{FM})$. The amplitude of the central output carrier depends on $J_0(\beta_{FM})$ and its value depends on the modulating signal, as can also be seen in equation (A.12) in appendix A. The amplitude of some sidebands may become zero for

specific values of the frequency modulation index β_{FM} . This is unlike AM modulation where the amplitude of the carrier does not depend on the value of the modulating signal.

When β_{FM} is very small, the (visual) power spectrum does not show whether the signal is modulated in amplitude or frequency because both modulations only have 2 sidebands around the carrier signal. This is also the reason why it is impossible to separate AM and FM in the frequency spectrum. Therefore signal demodulation needs to be performed to extract the instantaneous amplitude and frequency [3]. The basic expressions for (active) modulations in telecommunications are discussed in this section, the next section will focus on signal modulations from two excitation signals caused by nonlinearities (VAM).

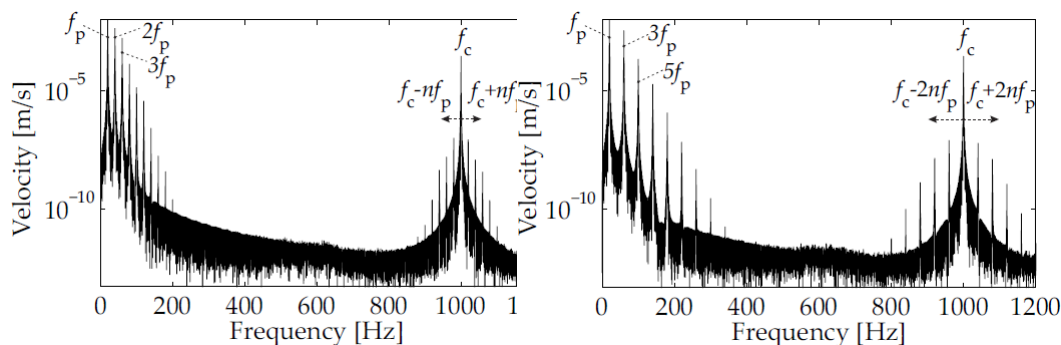
2.2 Nonlinearities causing AM and FM in VAM

The physical phenomena discussed in section 1.3 that are able to cause the amplitude and frequency modulations with the VAM-method can be caused by different classical and non-classical nonlinearities that are already discussed in different studies [8]:

- Velocity nonlinearities
 - Quadratic
 - Cubic
- Displacement nonlinearities
 - Quadratic
 - Cubic

One or a combination of the above mentioned nonlinearities can cause the creation of the signal modulations used in VAM. A quadratic nonlinearity will give odd and even sidebands, and odd and even higher harmonics [24]. A cubic nonlinearity will only give even sidebands and even higher harmonics in the response frequency spectrum [24]. This has also been concluded in (simplified) numerical simulations in [3], see figure 2.2(a) and 2.2(b). Another conclusion from these numerical simulations is that the displacement nonlinearities in that specific model will only show amplitude modulated responses and that a system containing nonlinearities in terms of velocities will show an amplitude and a frequency modulated response. This relates to the fact that the response of an undamped system will be in phase with its excitation and the response of a (viscous) damped system can exhibit a phase deviation.

It has also been shown in this study by Ooijevaar [3] experimentally that the pump frequency of the 4th natural frequency on this structure tends to a more quadratic (displacement) type of nonlinearity when compared with the previous mentioned numerical results. It has been shown in section 1.3.1 that the 4th natural frequency is a clapping mechanism.



(a) Quadratic nonlinearity: $f(q^2)$ as in [3]. (b) Cubic nonlinearity: $f(q^3)$ as in [3].

Figure 2.2: Fourier transformed response signals for a system containing a quadratic (a) and cubic nonlinearity (b) with respect to displacement $q(t)$ showing sidebands at $f_c \pm n f_p$ and $f_c \pm 2n f_p$ (with $n = 1, 2, 3, \dots$) respectively. This figure is taken from [3].

The underlying physical phenomena are still not understood, see section 1.3. However most obvious is a varying stiffness across the damage interface. These asymmetric stiffness effects and energy dissipative mechanisms such as friction, hysteresis and thermo-elastic phenomena can also be possible physical phenomena. When the pump and carrier frequencies are both applied to the previous discussed structure in [3], mostly amplitude modulations are present in the damaged region. The latter can be seen in figure 2.3. Both the clapping and kissing damage behaviors result in mainly amplitude modulations in the damaged area. It can therefore be concluded that the nonlinearity will be of a displacement type. Frequency modulation does also occur in the structure. Since this FM is not concentrated in the damaged region, it can only be used to globally indicate if this specific structure is damaged or not.

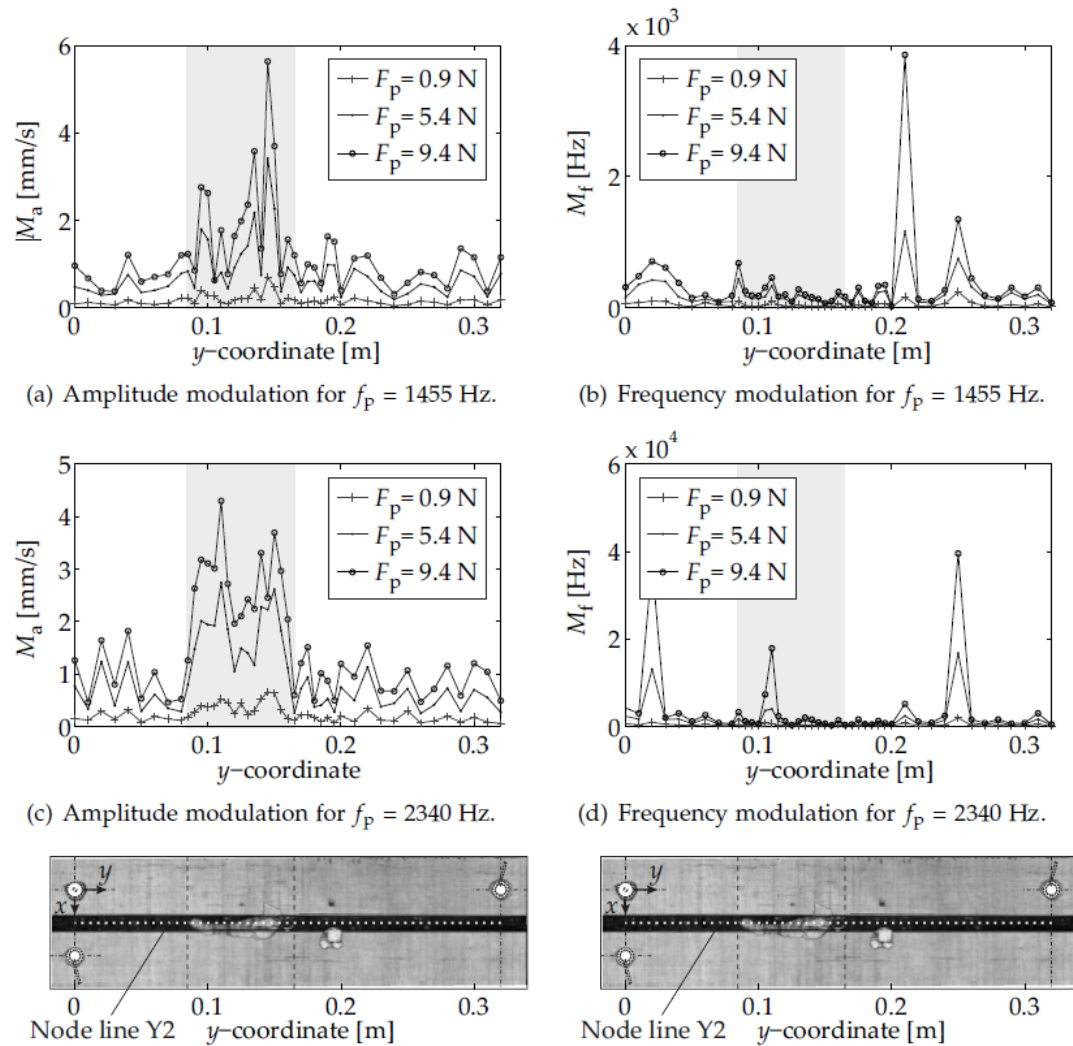


Figure 2.3: The (a, c) amplitude and (b, d) frequency modulation distributions of the carrier response for three pump excitation amplitudes. The results for $f_p = 1455$ Hz (clapping mode) are shown in (a, b), while (c, d) show the results for $f_p = 2340$ Hz (kissing mode). The carrier frequency was 50 kHz for all cases. This figure and information is taken from [3].

2.3 Two-tone forced vibration of a nonlinear system

To get a better understanding how the nonlinearities result in a modulated signal, an analytical obtained response of a simplified 1-DOF nonlinear system is discussed by Ooijevaar [3]. These analytical derivations will be discussed and expanded in this section.

2.3.1 Quadratic displacement nonlinearity

The clapping and kissing behaviors can probably best be approached with a quadratic displacement nonlinearity as concluded in [3]. This type of nonlinearity is analytically investigated by Ooijevaar for 1-DOF nonlinear system. There is however no mention how to verify that the obtained signal is only modulated in amplitude. The next section will focus on the same derivations in more detail and also provide a quadratic velocity nonlinearity.

A nonlinear multi-DOF system, the first part containing linear terms and the second part containing nonlinear terms, can be expressed as:

$$\ddot{\mathbf{q}} + \omega_{n,0}^2 \mathbf{q} = -\epsilon f(\mathbf{q}, \dot{\mathbf{q}}), \quad (2.12)$$

in which $\ddot{\mathbf{q}}$, $\dot{\mathbf{q}}$ and \mathbf{q} are the normalized acceleration, velocity and displacement vectors in one direction. Note that the eigenfrequency ω_0 is a scalar. There are however multiple solutions for the eigenvalue problem; the number of eigenfrequencies n corresponds to the number of independent equations of the system n . A multi-DOF system with a quadratic displacement nonlinearity and two tones forced vibrations can be expressed analytically as:

$$\ddot{\mathbf{q}} + \omega_{n,0}^2 \mathbf{q} = -\epsilon \mathbf{q}^2 + F_p \cos(\omega_p t + \phi_p) + F_c \cos(\omega_c t + \phi_c) \quad (2.13)$$

When using a perturbation technique based on a power series, the first-order steady state solution $\mathbf{q}(t)$ is expressed as:

$$\begin{aligned} \mathbf{q}_{\text{total}}(t) = & A_{p,n} \cos(\omega_p t + \phi_p) + A_{c,n} \cos(\omega_c t + \phi_c) - \frac{\epsilon}{2\omega_{n,0}^2} (A_{p,n}^2 + A_{c,n}^2) \\ & - \frac{\epsilon}{2(\omega_{n,0}^2 - 4\omega_p^2)} A_{p,n}^2 \cos(2\omega_p t + 2\phi_p) - \frac{\epsilon}{2(\omega_{n,0}^2 - 4\omega_c^2)} A_{c,n}^2 \cos(2\omega_c t + 2\phi_c) \\ & + A_{sb1,n} \cos((\omega_c - \omega_p)t + \phi_c - \phi_p) + A_{sb2,n} \cos((\omega_c + \omega_p)t + \phi_c + \phi_p), \end{aligned} \quad (2.14)$$

in which:

$$\begin{aligned} A_{sb1,n} &= \frac{-\epsilon A_{p,n} A_{c,n}}{\omega_{n,0}^2 - (\omega_c - \omega_p)^2}, & A_{c,n} &= \frac{F_c}{\omega_{n,0}^2 - \omega_c^2}, \\ A_{sb2,n} &= \frac{-\epsilon A_{p,n} A_{c,n}}{\omega_{n,0}^2 - (\omega_c + \omega_p)^2}, & A_{p,n} &= \frac{F_p}{\omega_{n,0}^2 - \omega_p^2}. \end{aligned}$$

When only a narrow band response around the carrier frequency is considered, equation (2.14) can be expressed as:

$$\begin{aligned} \mathbf{q}_{\text{bp}}(t) = & A_{c,n} \cos(\omega_c t + \phi_c) + A_{sb1,n} \cos((\omega_c - \omega_p)t + \phi_c - \phi_p) \\ & + A_{sb2,n} \cos((\omega_c + \omega_p)t + \phi_c + \phi_p), \end{aligned} \quad (2.15)$$

This is, according to Ooijevaar [3] in the 1-DOF presentation, an amplitude modulated response signal. When equation (2.15) is elaborated the total narrow band response is expressed as:

$$\begin{aligned} q_{\text{totalbp}}(t) = & \sum_{k=1}^n (A_{c,k} \cos(\omega_c t + \phi_c) + A_{sb1,k} \cos((\omega_c - \omega_p)t + \phi_c - \phi_p) \\ & + A_{sb2,k} \cos((\omega_c + \omega_p)t + \phi_c + \phi_p)), \end{aligned} \quad (2.16)$$

where $k = 1, 2, 3, \dots, n$ are the degrees of freedom with n the total amount of DOF's. Note that $q_{\text{totalbp}}(t)$ is a scalar and not a vector anymore. When it is assumed that the terms with a certain frequency (ω_p, ω_c and the sidebands ($\omega_c \pm \omega_p$)) will only contribute to the total response when their frequency corresponds with an eigenfrequency of the system ($\omega_{p,0}, \omega_{c,0}$ and the sidebands ($\omega_{(c \pm p),0}$)), the total narrow-band response will become:

$$\begin{aligned} q_{\text{totalbp}}(t) = & A'_c \cos(\omega_c t + \phi_c) + A'_{sb1} \cos((\omega_c - \omega_p)t + \phi_c - \phi_p) \\ & + A'_{sb2} \cos((\omega_c + \omega_p)t + \phi_c + \phi_p) \end{aligned} \quad (2.17)$$

in which:

$$A'_{sb1} = \frac{-\epsilon A'_p A'_c}{\omega_{(c-p),0}^2 - (\omega_c - \omega_p)^2}, \quad A'_c = \frac{F_c}{\omega_{c,0}^2 - \omega_c^2},$$

$$A'_{sb2} = \frac{-\epsilon A'_p A'_c}{\omega_{(c+p),0}^2 - (\omega_c + \omega_p)^2}, \quad A'_p = \frac{F_p}{\omega_{p,0}^2 - \omega_p^2}.$$

Compared to section 2.1, the narrow-band signal shows differences with an actively modulated signal. The carrier amplitude is in the output signal multiplied by the term:

$$\frac{1}{[\omega_{c,0}^2] - \omega_c^2}. \quad (2.18)$$

The amplitude of the sidebands are multiplied by the term:

$$\frac{(\omega_{p,0}^2 - \omega_p^2)(\omega_{c,0}^2 - \omega_c^2)}{(\omega_{(c\pm p),0}^2 - (\omega_c \pm \omega_p)^2)}. \quad (2.19)$$

From equation (2.18) it can be concluded that the amplitude of the central carrier in the output response is not constant for different carrier frequencies, compared to the active amplitude modulation in section 2.1. From the second statement in equation (2.19) the observations in [19] are proven, certain combinations of the carrier and pump frequency do give the highest signal modulations. Also concluding from equation (2.19) is that the signal modulations will be the highest if for the carrier, pump and sideband frequencies, natural frequencies of the system are chosen as is shown in [29]. The latter can be visualized. The expression for the narrow band response in equation (2.15) is plotted with $F_p = 8 \text{ N}$, $F_c = 1 \text{ N}$, $\epsilon = 0.04$, $\omega_p = 2 \cdot \pi \cdot 10 \frac{\text{rad}}{\text{s}}$ and $\omega_c = 2 \cdot \pi \cdot 500 \frac{\text{rad}}{\text{s}}$, see figure 2.4. The terms from equation (2.18) and (2.19) give a difference between a natural frequency of the structure with the carrier frequency and the sideband frequencies. These have to have minimal difference such that the sidebands can be noticed in the frequency spectrum, so a difference of $(\omega_{c,0}^2 - \omega_c^2) = 1 \frac{\text{rad}}{\text{s}}$, $(\omega_{p,0}^2 - \omega_p^2) = 1 \frac{\text{rad}}{\text{s}}$ and $(\omega_{(c\pm p),0}^2 - (\omega_c \pm \omega_p)^2) = 1 \frac{\text{rad}}{\text{s}}$ is chosen for figure 2.4. This consequently shows that the carrier frequency should be a lot closer to a natural frequency than the pump frequency due to the quadratic terms.

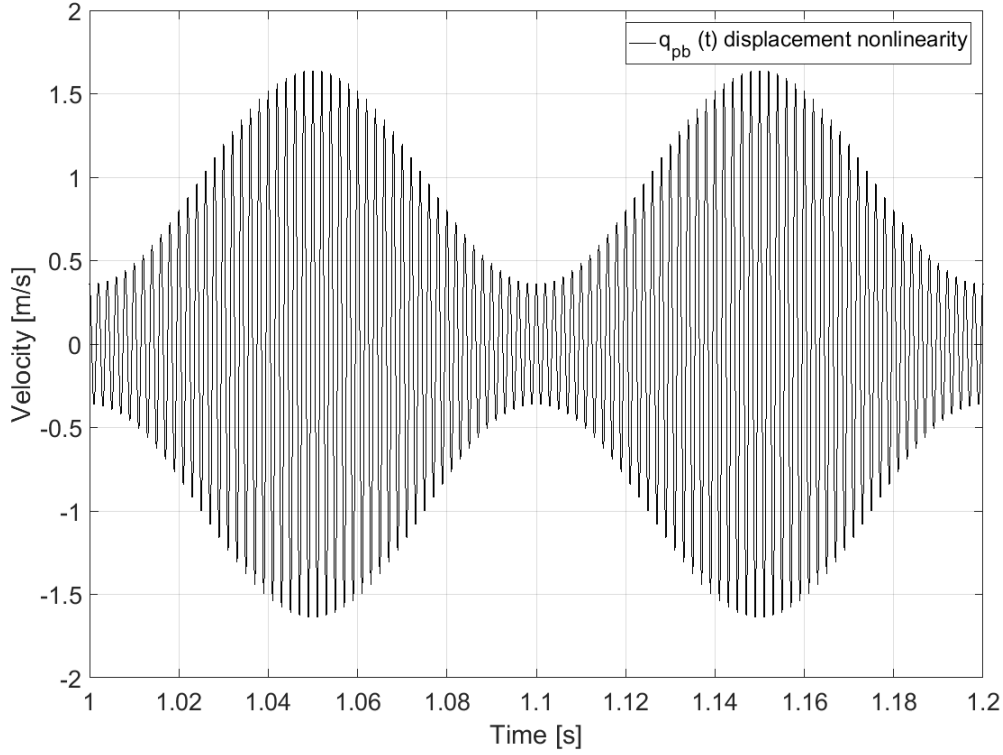


Figure 2.4: The bandpass filtered and modulated carrier response of $f_p = 10$ Hz, $f_c = 500$ Hz and $e = 0.04$ caused by a quadratic displacement nonlinearity.

2.3.2 Quadratic velocity nonlinearity

Not only nonlinearities in terms of displacement could cause the signal modulations in VAM. The dissipative nonlinearities such as hysteresis are most likely caused by a quadratic velocity nonlinearity. This nonlinearity will be investigated in this section with the same method as in section 2.3.1. A multi-DOF system with a quadratic velocity nonlinearity and two tones forced vibrations can be expressed analytically as:

$$\ddot{\mathbf{q}} + \omega_{n,0}^2 \mathbf{q} = -\epsilon \dot{\mathbf{q}}^2 + F_p \cos(\omega_p t + \phi_p) + F_c \cos(\omega_c t + \phi_c) \quad (2.20)$$

The complete derivation can be found in appendix B. When the first order nonlinear solution is considered and when only the frequencies around the carrier signal are taken into account, the following narrow band response is obtained:

$$q_{bp}(t) = A'_c \cos(\omega_c t + \phi_c) - A'_{sb1} \omega_p \omega_c \cos((\omega_c - \omega_p)t + \phi_c - \phi_p) - A'_{sb2} \omega_p \omega_c \cos((\omega_c + \omega_p)t + \phi_c + \phi_p) \quad (2.21)$$

$$A'_{sb1} = \frac{-\epsilon A'_p A'_c}{\omega_{(c-p),0}^2 - (\omega_c - \omega_p)^2}, \quad A'_c = \frac{F_c}{\omega_{c,0}^2 - \omega_c^2},$$

$$A'_{sb2} = \frac{-\epsilon A'_p A'_c}{\omega_{(c+p),0}^2 - (\omega_c + \omega_p)^2}, \quad A'_p = \frac{F_p}{\omega_{p,0}^2 - \omega_p^2}.$$

The obtained narrow band response signal of a quadratic velocity nonlinearity in equation (2.21) differs from that of a quadratic displacement nonlinearity in equation (2.15) in the amplitudes of the two sideband components caused by the signal modulations. These amplitudes are multiplied by the term $\omega_p \omega_c$. When it is assumed that the quadratic velocity nonlinearity would cause only

frequency modulation, the extra term $\omega_p \omega_c$ would mean the difference between AM and FM. When comparing this assumption with equation (2.4) and (2.9), it is however not in line with the obtained expressions for the active controlled AM and FM. The difference between the active AM and FM in equation (2.4) and (2.9) is that the amplitudes of the sidebands are multiplied with $\frac{1}{\omega_p}$ and not with $\omega_p \omega_c$.

The expression in equation (2.21) is plotted in figure 2.5 with again the same values: $F_p = 8$ N, $F_c = 1$ N, $\epsilon = 0.04$, $\omega_p = 2 \cdot \pi \cdot 10 \frac{\text{rad}}{\text{s}}$, $\omega_c = 2 \cdot \pi \cdot 500 \frac{\text{rad}}{\text{s}}$, $(\omega_{c,0}^2 - \omega_c^2) = 1 \frac{\text{rad}}{\text{s}}$, $(\omega_{p,0}^2 - \omega_p^2) = 1 \frac{\text{rad}}{\text{s}}$ and $(\omega_{(c \pm p),0}^2 - (\omega_c \pm \omega_p)^2) = 1 \frac{\text{rad}}{\text{s}}$. The amplitude of the plotted function is considerable higher than in figure 2.4. This is caused by the multiplication of the amplitudes of the sidebands by $\omega_p \omega_c$. It is also clear that there is more than 100 % amplitude modulation when figure 2.4 is compared with figure 2.1(b).

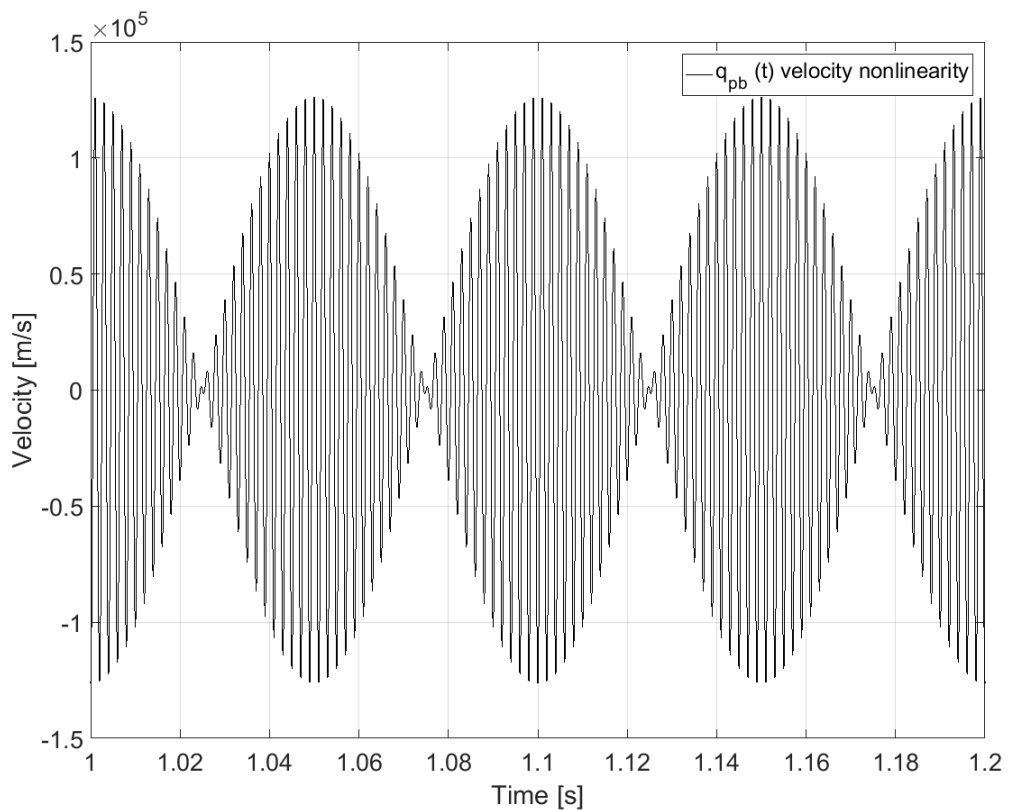


Figure 2.5: The bandpass filtered and modulated carrier response of $f_p = 10$ Hz, $f_c = 500$ Hz and $e = 0.04$ caused by a quadratic velocity nonlinearity.

2.4 Selection of the excitation frequencies for VAM

From the previous section it can be concluded that the excitation frequencies for VAM have to be close to a natural frequency of the investigated structure to give noticeable signal modulations. This has also been concluded in different studies in the literature [3, 29]. The damages in these studies are however not controlled and therefore it is very hard to find a relation between the natural frequencies of a damage(d structure) and the carrier frequency. In this thesis a composite plate with an artificial delamination is considered, such that the global eigenfrequencies of the entire plate and the local eigenfrequencies of the delamination can be determined. Note that the modal density of the global eigenfrequencies will become higher in higher frequency ranges. The selection of the pump frequency seems to be not that difficult for a test specimen. The frequency response functions can be determined for different spatial points in a controlled test

setup and the accompanied operational deflection shapes can be visualized. A global natural frequency in the lower frequency ranges is selected as pump frequency with a desired operational deflection shape. It should however be stated that the pump frequency selection is more complicated when only the pristine global dynamic behavior is known and the (size of the) damage is unknown: the natural frequencies and accompanied operational deflection shapes will differ depending on the damage (size). The global natural frequencies with their operational deflection shapes are first determined numerically for the pristine case. Also the local frequency behavior will be approximated analytically for an artificial delamination. In section 3.3.1, the natural frequencies of the plate will be determined experimentally for the damaged scenario.

2.4.1 The global eigenfrequencies of a composite plate

The global eigenfrequencies of the plate are used in section 3.1.2 to determine the dimensions of the experimental specimens. Limitations on the dimensions and the lay-up are caused by the production method and the measuring equipment, therefore only the numerical model is briefly discussed in this section. The numerical model is created in Ansys Mechanical APDL 14.0, a rectangular composite plate. Shell elements can be assigned with a shell section that contains the number of plies, the ply thickness and the ply orientation. An area-based model with shell elements can be used for a composite plate since the thickness of the plate is relative small compared to the length and width. Another option is creating a model in Ansys based on solid elements. Every ply has to be meshed separately in this case and the material properties have to be calculated for every ply since a certain ply orientation has influence on these properties due to the anisotropic properties of a composite ply. However a numerical model based on solid elements is not very suitable for this thin walled structure. It requires a very dense grid in-plane which will result in a lot of elements since a large aspect ratio will give poor results. Moreover there is a high risk of locking since the dominant deformation mode is bending.

An area-based model of a pristine composite plate is created with a lay-up of $[0/90/45/-45]_{2,s}$. The shell181 element is used, which is a four-noded element with six degrees of freedom at each node. The ply thickness is chosen to be 0.1375 mm with 3 integration points and the dimensions of the plate are 300×300 mm. A modal analysis is used to extract the first 20 eigenfrequencies and mode shapes. In figure 2.6, the 4th bending mode can be seen. This mode shape corresponds with [30] and will be used later on to determine the location of the artificial damage in the plate to activate the clapping mechanism discussed in section 1.3.1. This Ansys model can be adjusted and used to determine the appropriate pump frequencies for the composite structure used in the experimental part.

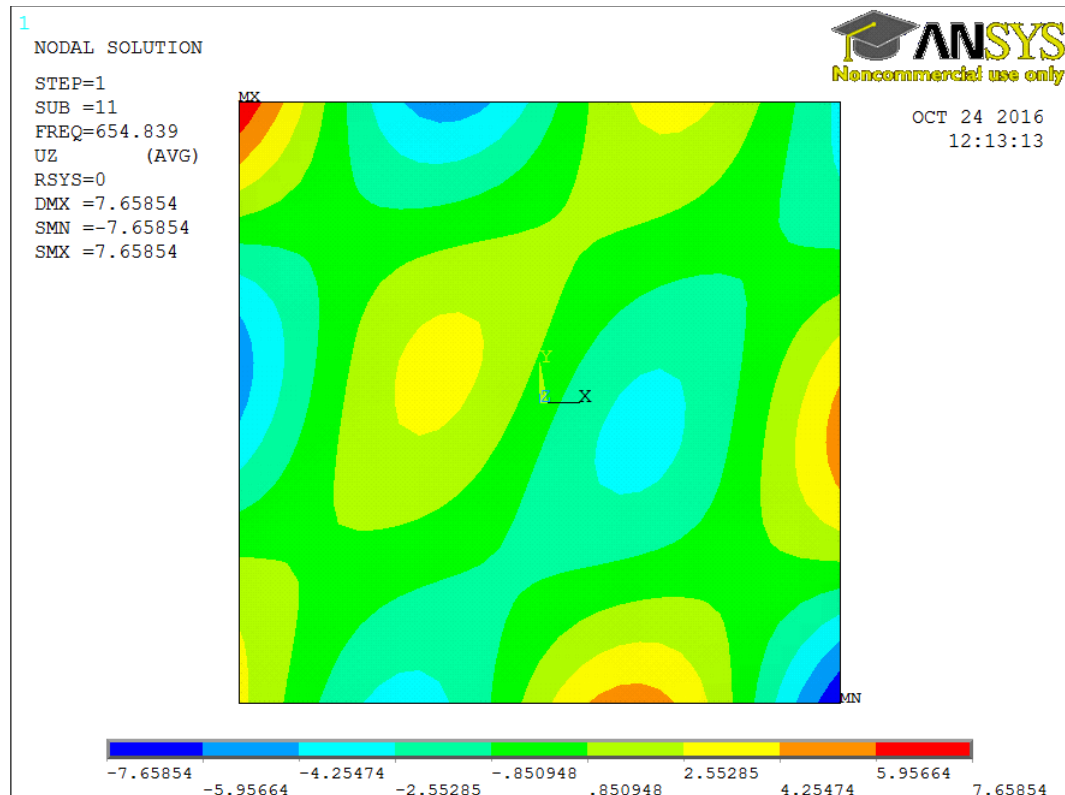


Figure 2.6: The 11th mode of $[0/90/45/-45]_2$, s composite plate, obtained with Ansys.

2.4.2 The local eigenfrequencies of the delamination

The damaged composite plate with the artificial delamination can be represented as in figure 2.7. When $H_2 \ll H$, the volume with thickness H_2 and radius R will be assumed to show the clapping behavior [31] and it is therefore assumed that this volume has to be excited by the carrier wave. The volume with thickness H_2 and radius R will therefore be treated as a separate circular plate with specific boundary conditions, this is called ‘the free model theory’. This model has shown to be physically inadmissible [31], the delaminated layers deform freely without touching each other. The ‘constrained theory’ in which the delaminated layers are assumed to kiss each other and are allowed to slide over each other is physically admissible [31]. The local eigenfrequencies will be estimated with the ‘the free model theory’ in this thesis, even though the ‘constrained theory’ model will give more accurate results. The actual local eigenfrequencies are assumed to be in between the eigenfrequencies of a boundary condition of clamped (upper limit) and simply supported (lower limit).

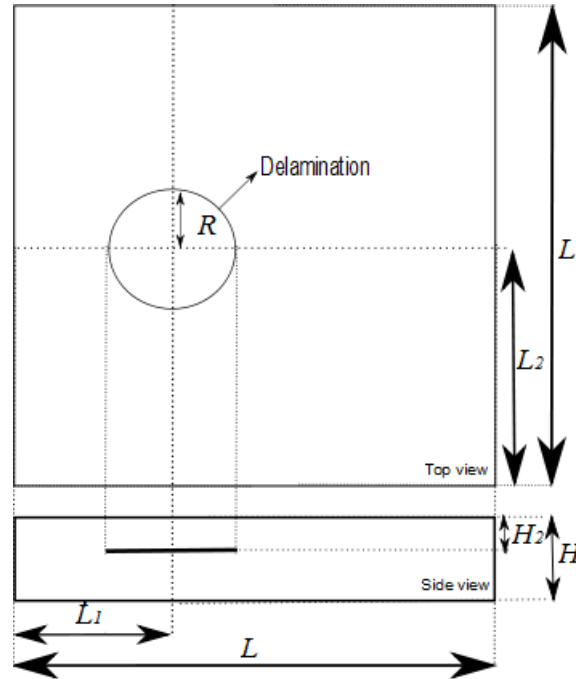
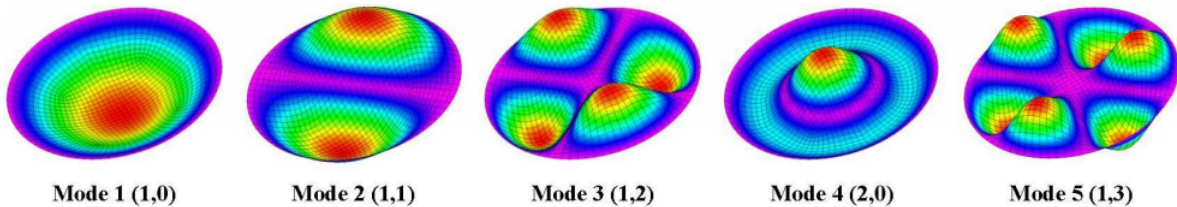


Figure 2.7: Top and side view of a composite plate with a delamination.

When the thickness H_2 , the radius R of the artificial delamination, the material properties, the number of layers with their respective thickness and orientation, and the material properties are known, the flexural natural vibrations can be calculated with two different boundary conditions: simply supported and clamped. The different modes are given in figure 2.8 as can be seen in [32].

SS



C

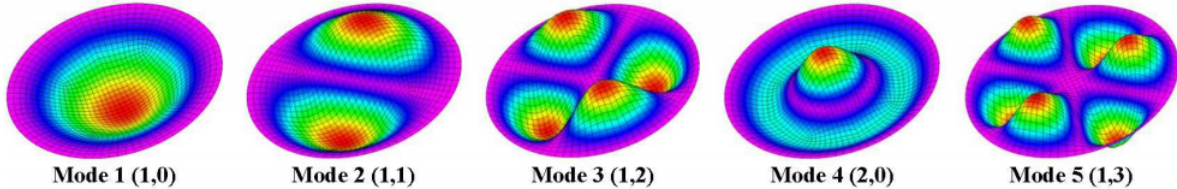


Figure 2.8: The first 5 modes of simply supported (SS) and a clamped (C) circular plate as in [32]. The mode i refers to the number of circular nodes j of the circular plate and the number of nodal diameters k .

The differential equation describing the circular plate in a polar coordinate system can be expressed as [32]:

$$\Delta_r \Delta_r W_b + \omega^2 \frac{J}{D} \left(1 + \frac{mD}{JS}\right) \Delta_r W_b + \omega^2 \frac{m}{D} \left(\frac{\omega^2 J}{S} - 1\right) W_b = 0, \quad (2.22)$$

in which the solution (natural vibrations) can take the form of $W_b(r, \phi, t) = W(r, \phi) \sin \omega t$ and $W(r, \phi)$ is the vibration amplitude with ω the corresponding natural frequency. The complete

derivation and solution can be found in [32]. The following non-dimensional frequency parameter is obtained for flexural vibrations:

$$\Omega = \omega R^2 \sqrt{m/D}, \quad (2.23)$$

in which R is the diameter of the circular plate, $D = \frac{EH^3}{12(1-\nu^2)}$ and m is the mass.

The goal is to obtain local natural frequencies of the delamination that can be measured with the available equipment at the University of Twente. Also note that the delamination does not become too large and is produce-able, meaning that a too large delamination will cause ripples in the delamination during the production process. The boundary conditions for a clamped circular plate are zero displacement and zero velocity at the edge of the circular delamination. For a simply supported circular delamination the displacement is also zero at the edge and also the moment will be zero at this boundary. The modulus of elasticity of the thin laminate is determined for a [0/90] laminate. The natural frequencies for a clamped and simply supported circular plate with thickness of 0.26 mm are given in table 2.1. These frequencies are used to determine the size and thickness of the delamination of the test specimens in section 3.1.2. The actual local natural frequencies of the test specimens will be determined experimentally in section 3.3.2. In appendix E, the eigenfrequencies of a simply supported and clamped circular plate are listed for a diameter of 50 mm and 100 mm.

Table 2.1: Eigenfrequencies for a clamped (C) and simply supported (SS) circular plate with a diameter of 100 mm and thickness of 0.26 mm. The mode i refers to the number of circular nodes j of the circular plate and the number of nodal diameters k .

Eigenfrequencies		[kHz]	[kHz]	[kHz]	[kHz]
Mode i (j, k)		1	2	3	4
1	SS	1.4	4.0	7.4	11.5
	C	2.9	6.1	10.0	14.7
2	SS	8.6	14.0	20.2	27.3
	C	11.5	17.5	24.4	32.0
3	SS	21.4	29.6	38.7	48.6
	C	25.7	34.6	44.3	54.9
4	SS	39.9	51.0	62.9	75.7
	C	45.6	57.4	69.8	83.3

2.5 Signal extraction

The response of a structure with a two-tone forced excitation mentioned in the previous sections, can be studied in the frequency and time domain. Since the focus of this thesis is mainly on the carrier frequency response and its potential sidebands, a zero-phase bandpass FIR (i.e. finite impulse response) filter in a narrow frequency band around the carrier frequency is used to separate this frequency band from the rest of the total response. This can be tested by considering a modulated velocity response signal by a quadratic displacement nonlinearity from equation (2.17):

$$q(t) = A_p \cos(\omega_p t) + A_c \cos(\omega_c t) + \sum_{k=0}^n \left[\frac{1}{k} \frac{1}{2} \epsilon A_p^2 \cos(k\omega_p t) \right] + \sum_{k=0}^n \left[\frac{1}{k} \frac{\epsilon A_p A_c}{(\omega_{0(c \pm p)}^2 - (\omega_c \pm \omega_p)^2)} [\cos((\omega_c \pm k\omega_p)t)] \right] \quad (2.24)$$

in which $k = 0, 1, 2, 3, \dots, 10$ refers to the number of higher harmonics (the first summation) and the number of sidebands (the second summation). The higher harmonics and sidebands are multiplied with $\frac{1}{k}$ since higher order harmonics and sidebands will decrease in amplitude. This is only an approximation and can also be proven by taking a higher nonlinear solution than only the first order nonlinear solution that is considered in equation (2.17). From experimental results it is also clear the higher order sidebands decrease in magnitude [3].

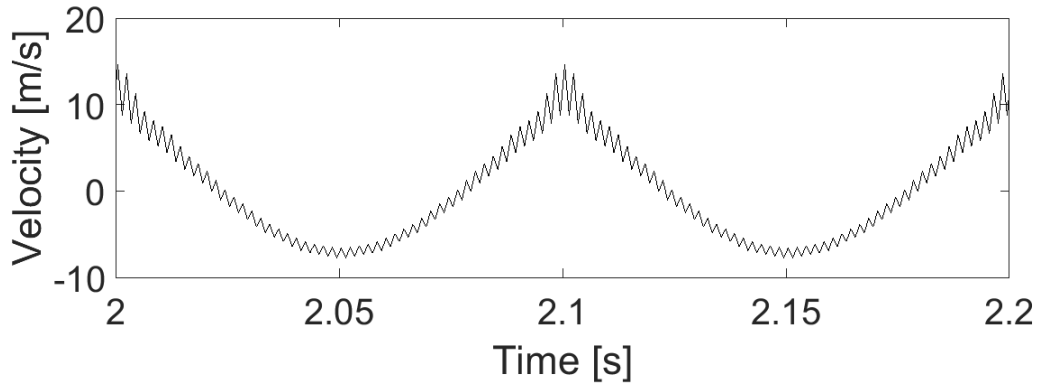


Figure 2.9: Time signal of the total response signal with higher harmonics and sidebands.

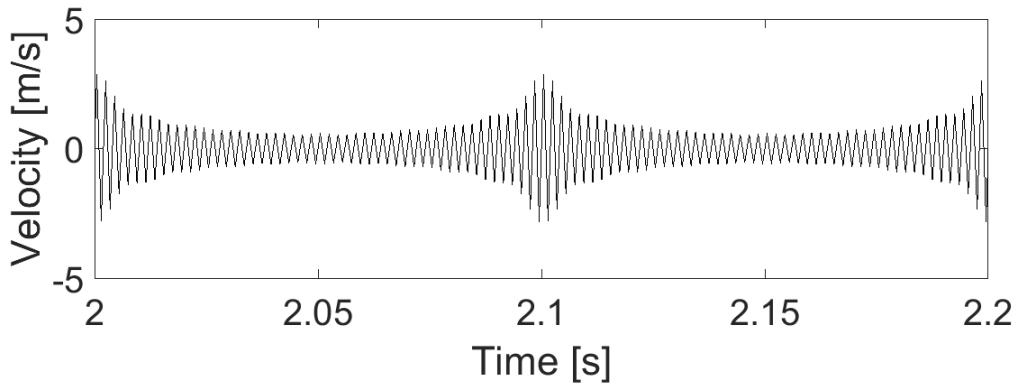


Figure 2.10: Time signal of the bandpass filtered response signal.

When the zero-phase FIR filter in a frequency band between $f_{cutoff1} = 350$ Hz and $f_{cutoff2} = 650$ Hz is applied, the pump frequency and its higher harmonics are filtered out. The total and filtered response signal are plotted in the time domain (with $F_p = 8$ N, $F_c = 1$ N, $\epsilon = 0.04$, $\omega_0 - \omega_{c/p/n \cdot p/c \pm n \cdot p} = 1 \frac{\text{rad}}{\text{s}}$, $\omega_p = 2 \cdot \pi \cdot 10 \frac{\text{rad}}{\text{s}}$ and $\omega_c = 2 \cdot \pi \cdot 500 \frac{\text{rad}}{\text{s}}$) in figure 2.9 and figure 2.10. It can be clearly seen that the lower frequencies with their higher amplitudes are not present in the filtered response. The narrow-band response can be studied in the frequency and time domain using different techniques. These are discussed in the following sections.

2.5.1 Frequency spectrum

To obtain the frequency spectrum of the narrow-band response, a Fast Fourier Transform (FFT) can be applied. When applying this FFT to equation (2.24), the frequency spectrum of the total response can be seen in figure 2.11(a). A comparison with the bandpass filtered response illustrated in figure 2.11(b) shows that the frequency content around the carrier frequency does not change. The statement made in section 2.3 that the frequencies of the pump, carrier, higher harmonics and sidebands have to be close to a natural frequency of the structure to have a noticeable magnitude can also be verified by the present example and its FFT. For example when the difference $\omega_0 - \omega_{c \pm p} \gg 1 \frac{\text{rad}}{\text{s}}$ the sidebands have a much smaller magnitude in the frequency spectrum.

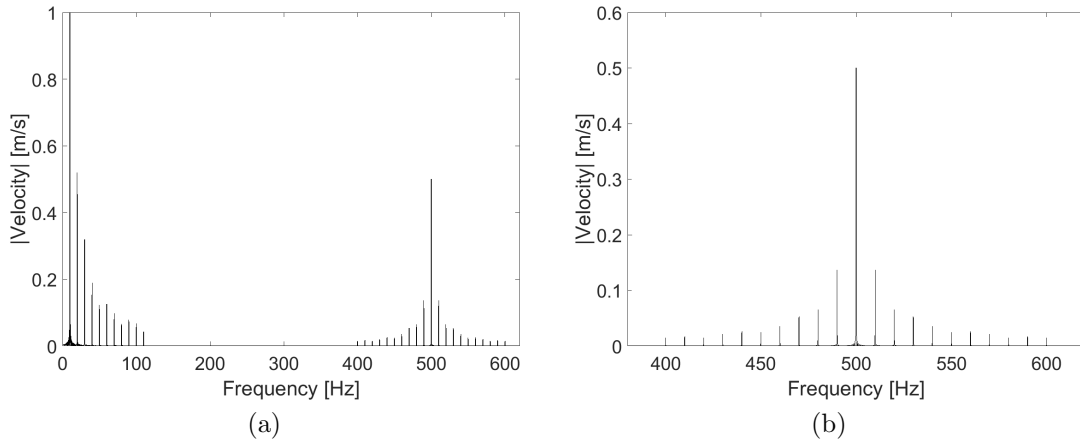


Figure 2.11: Fourier spectra of the total (a) and bandpass filtered (b) response.

An important aspect for separating all the frequencies properly is the resolution f_{res} in the frequency spectrum obtained by the FFT:

$$f_{\text{res}} = \frac{f_s}{N_{\text{samples}}} = \left[\frac{\text{Hz}}{\text{bin}} \right] \quad (2.25)$$

in which N_{samples} is the total number of samples of the measured signal and f_s the sampling frequency. The frequency resolution can thus be increased by acquiring a longer time signal or decreasing the sampling rate. Another option will be to apply averaging in the FFT. Note that with a fixed sampling frequency, the increasing frequency resolution decreases temporal resolution. Effectively all time information is lost in the frequency spectrum.

2.5.2 Signal demodulation procedures

To obtain the instantaneous amplitude (or envelope function), the instantaneous phase and the instantaneous frequency for narrow-band signals, the Hilbert Transform (HT) can be used. The HT method is explained in appendix C. Since the HT is limited to smaller frequency windows, another option is the Hilbert-Huang transform (HHT) [21]. The HHT can be used for any type of signal with varying frequency content and decomposes the signal into so-called intrinsic mode functions (IMF) along with a trend to obtain the instantaneous data. These IMF's all contain a certain frequency band. Note that the HHT method is an empirical analysis and not strictly necessary in this thesis so it will not be discussed anymore. Appendix D discusses the HHT in more detail.

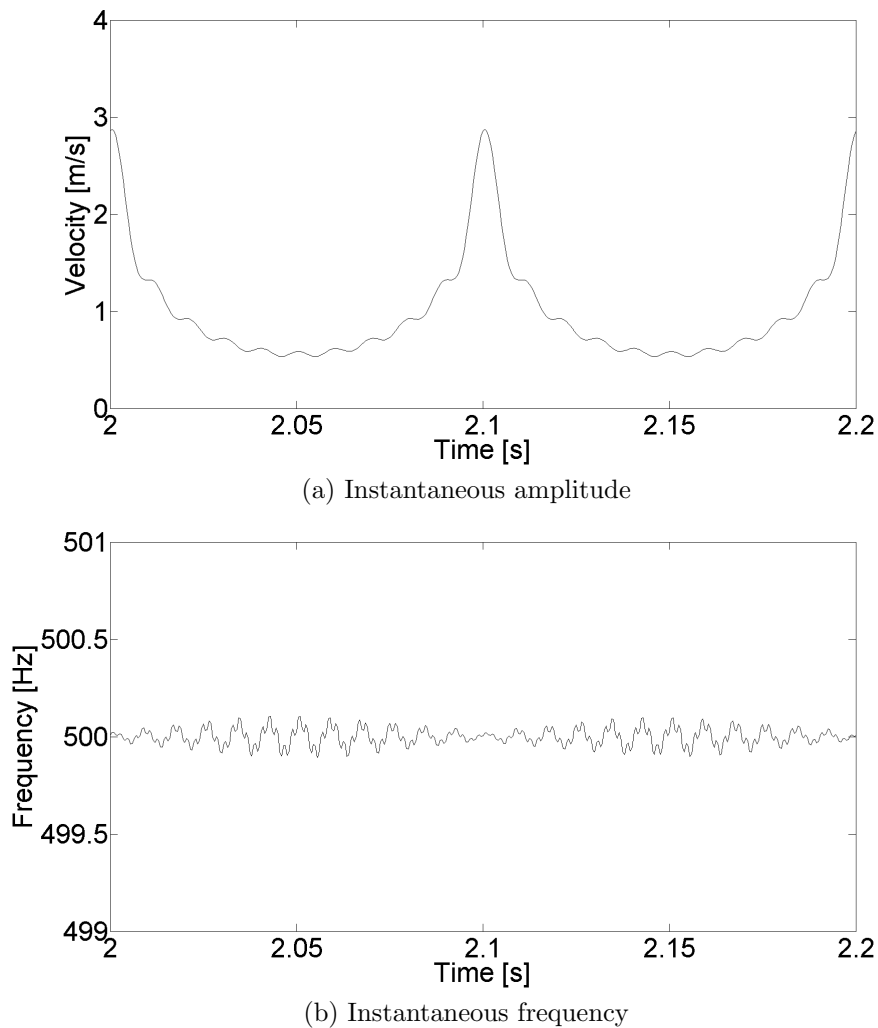


Figure 2.12: The instantaneous amplitude (a) and frequency (b) of the bandpass filtered response.

When the HT is applied to the narrow-band response signal of equation (2.24), the obtained instantaneous properties displayed in figure 2.12 are obtained. A variation in the amplitude is clearly visible (amplitude modulation) because the instantaneous amplitude does not show a constant value. This is also the case for the instantaneous frequency (frequency modulation). The latter is however less pronounced. The fact that there is just a small variation in the instantaneous frequency, seems to depend on the number of sidebands that are taken into account. When only one sideband at each side of the carrier frequency is considered, hardly any frequency modulation is detected. The instantaneous amplitude and frequency can be seen in figure 2.13. The reverse statement does not have to apply, so many sidebands do not automatically prove that a signal is frequency modulated. There is still some frequency modulation present in figure 2.13(b). This indicates that the narrow band response signal is still modulated minimal in frequency. The reason for the small amount of frequency modulation can likely be the result of numerical errors.

The difference between odd, even and the previous discussed even+odd sidebands on the instantaneous frequency and amplitude is also briefly investigated. It seems that the presence of only odd sidebands does not indicate that there is only FM or AM. The same holds for even sidebands.

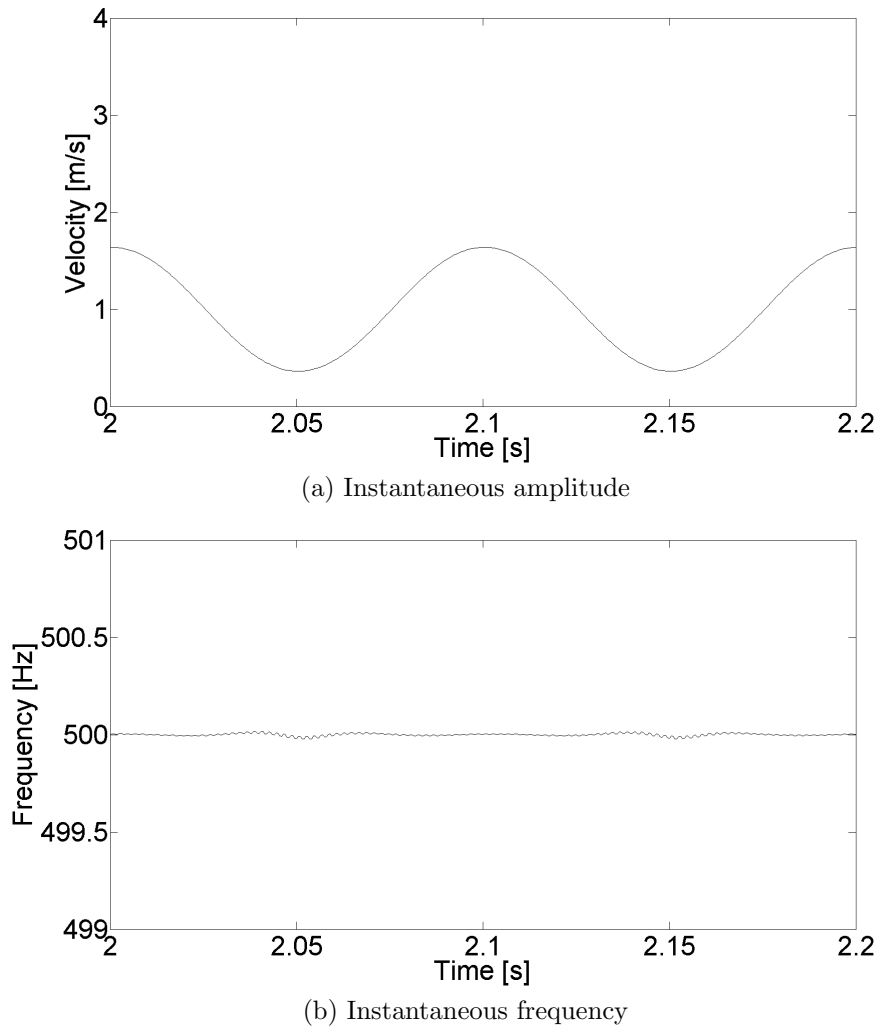


Figure 2.13: The instantaneous amplitude (a) and frequency (b) of a bandpass filtered response with only one sideband.

2.6 Summary

This chapter has given more insight on the excitation frequencies for the VAM-method. A multi-DOF system with a two-tone harmonic excitation and a velocity or displacement quadratic nonlinearity is solved. From the first order steady state solution it is concluded that choosing the pump and carrier frequency equal to an eigenfrequency of the structure greatly enhances the amplitude of the frequency content in the narrow band response signal. Especially the carrier frequency should be chosen close to an eigenfrequency. The amplitude of the sidebands in the frequency spectrum are a function of the underlying frequency response of the system but also of the selection of the pump and carrier frequency, see equation (2.19). A signal demodulation procedure is applied to an analytical response based on the first order solution of a quadratic displacement nonlinearity that can be used in the experimental part. A zero-phase FIR filter is applied around the carrier frequency and with the Hilbert Transform the envelope of this bandpass response is determined together with the instantaneous frequency. A Fast Fourier Transform is applied to reveal the frequency content of the total and bandpass response. These can all also be applied to the experimental data.

Chapter 3

Experimental work

This chapter introduces the experimental work. The manufacturing of the two composite structures with two different delamination is discussed first, followed by the experimental setup. The final part of this section discusses the three-step experimental procedure used to measure the vibro-acoustic modulation behavior.

3.1 Composite plate structures

Two identical composite plates are manufactured at the Thermoplastic composites Research Center (TPRC) located in Enschede for the experimental work. The composite plates have a different delamination size but only one plate will be used for the VAM-experiments. The structure is schematically illustrated in figure 3.1. The material, production process and delamination are discussed in this section.

3.1.1 Material

The VAM-method is applied to a lot of different materials in the literature. Returning resin types are epoxy and PEEK/PEKK which are mostly reinforced by carbon or glass fibers. To relate the results of this research to research in the literature, the same material is used as in [3]. The plate has a lay-up of 16 individual plies of unidirectional AS4D fibers with a thermoplastic PEKK-FC material (Cytec, Boeing spec). A lay-up of $[0/90/45/-45]_{2,s}$ is chosen such that a quasi-isotropic laminate is achieved, the in-plane properties are isotropic. This makes analytical and numerical simulations easier. Every ply has a thickness of 0.13 mm which should result in a laminate thickness of 2.08 mm.

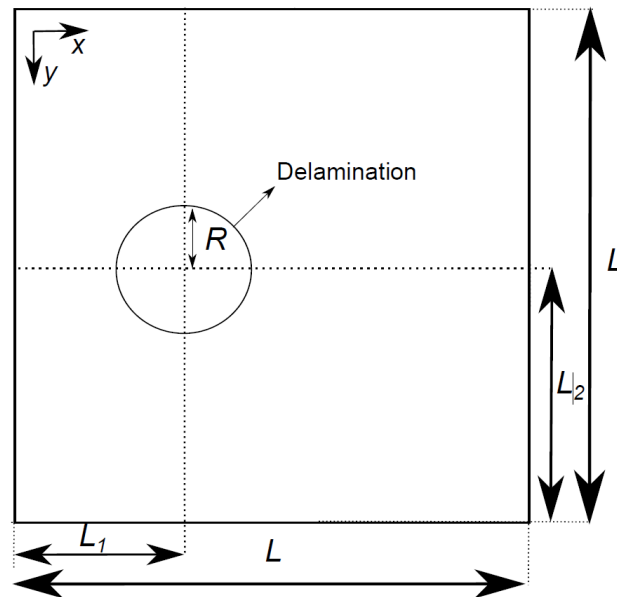


Figure 3.1: Top view of the composite plate structure with outer dimensions L . The delamination with radius R and location L_1 and L_2 is indicated.

3.1.2 Production with the artificial delamination

For the production of the thermoplastic PEKK/AS4D plates, different methods can be used. The Netherlands Aerospace Centre (NLR) made this material available in pre-preg form, therefore the production techniques are limited. TPRC gave the opportunity to fabricate the panels in their workshop. Standard available molds are 305 by 305 mm (12 by 12 inch) or 610 by 610 mm (24 by 24 inch). The smaller one is chosen because the UD fibers could ‘split’ at the sides for larger molds, and because a fabrication error in the thickness of 0.125 mm for every 300 mm is likely to occur in the press. A numerical model of the pristine case is made in section 2.4 to study the different eigenfrequencies and mode shapes for different dimensions and different laminate lay-ups of the plate. With the dimensions of 305 by 305 mm and the lay-up of $[0/90/45/-45]_{2,s}$, the eigenfrequencies are easy to separate (only the 6th, 7th and 8th eigenfrequency are close together) and they are in the range of the measuring/actuation capabilities. Sufficient deflection can also be conveniently measured with the equipment available at the laboratory at the University of Twente, discussed in section 3.5.

To create an artificial delamination in the test-specimens an insert is used between two adjacent plies. The inserts are made from Kapton and will not be affected by the pressing temperatures. To achieve separation (a delamination) the Kapton has to be treated with Frekote 700-NC release agent because Kapton will bond with the PEKK. Due to the orientation of the delamination the Kapton insert will stay in the delamination and could therefore influence the experimental results. When a thickness of $12.5 \cdot 10^{-6}$ m is used (approximately a tenth of a ply thickness) the mass will be low and in combination with a low stiffness (a tensile modulus of only 2 GPa), it is assumed that the Kapton insert will not influence the results. To prevent wrinkling and moving of the insert, weldspots are placed 5-10 mm away from the boundary of the insert, see figure 3.2.

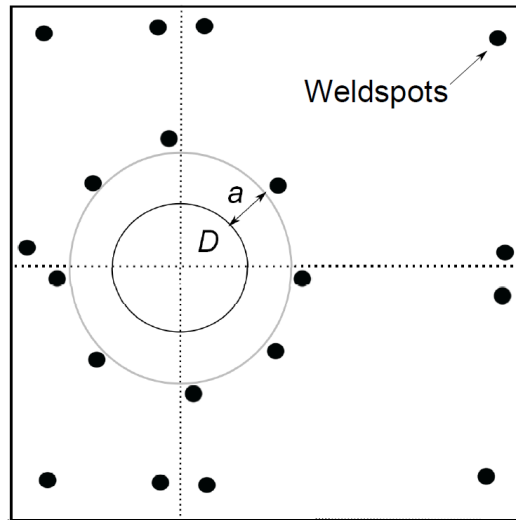


Figure 3.2: Top view of the composite plate structure. The delamination D is placed on a distance a from the weldspots. The weldspots are marked as solid dots.

The numerically calculated mode shapes of the pristine plate are used to determine where the delamination has to be placed. For the current research and most probably future research, it is desirable that the delamination can show clapping and kissing behavior. The delamination is not placed on the sides because this will not result in realistic boundary conditions of the delamination. The delamination is placed between the 14th and 15th ply, since this stimulates the opening and closing behavior of the delamination. When exciting the composite plate in its bending modes and the delamination is placed between the two mid-plane layers, the delamination will not show the opening-closing behavior.

Impact tests in the literature have shown to result in delaminations in the plies near the surface regions [2]. The delaminations in this impact test do however show to extend more in the 90° direction than the 0° direction, and the shape becomes more peanut-shaped with increasing velocity of the impact projectile [33]. Another observation is that the delamination formed with high-velocity impact and low-velocity impact are very similar. For this research, delaminations in the shape of a circle are used and still resemble a delamination obtained by an impact test in [2]. The main reason for choosing a circular delamination is that the behavior of the delamination can be more easily predicted and analytically described. Two different sizes of the delamination are used with a radius R of 25 and 50 mm located on $L_1 = \frac{1}{3}L$ and $L_2 = \frac{1}{2}L$. The minimum size of the delamination is again dependent on the capabilities of the measuring equipment which is present at the University of Twente. The smaller the delamination will be, the higher the carrier frequency has to be due to the assumption that the carrier frequency should be equal to the local natural frequency. These excitation carrier frequencies are already investigated in section 2.4.2.

3.1.3 Validation of the delamination

The two manufactured panels are analyzed with an ultrasonic C-scan to check the location of the delaminations. A distinct location of the delamination cannot be seen. It appears that the $12.5 \cdot 10^{-6}$ m thickness of the Kapton inserts is too small to be properly detected by the C-scan at TPRC. The location of the delaminations can however still be spotted with prior knowledge and when the plate is placed with the delamination facing upwards, see figure 3.3. See appendix F for all the original obtained C-scan figures.

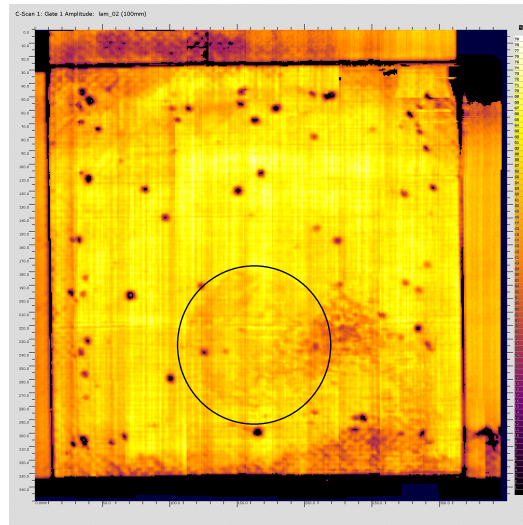


Figure 3.3: Ultrasonic C-scan of laminate 2 with a delamination of $R = 50\text{mm}$. The location of the delamination is highlighted in black. The weldspots be clearly seen.

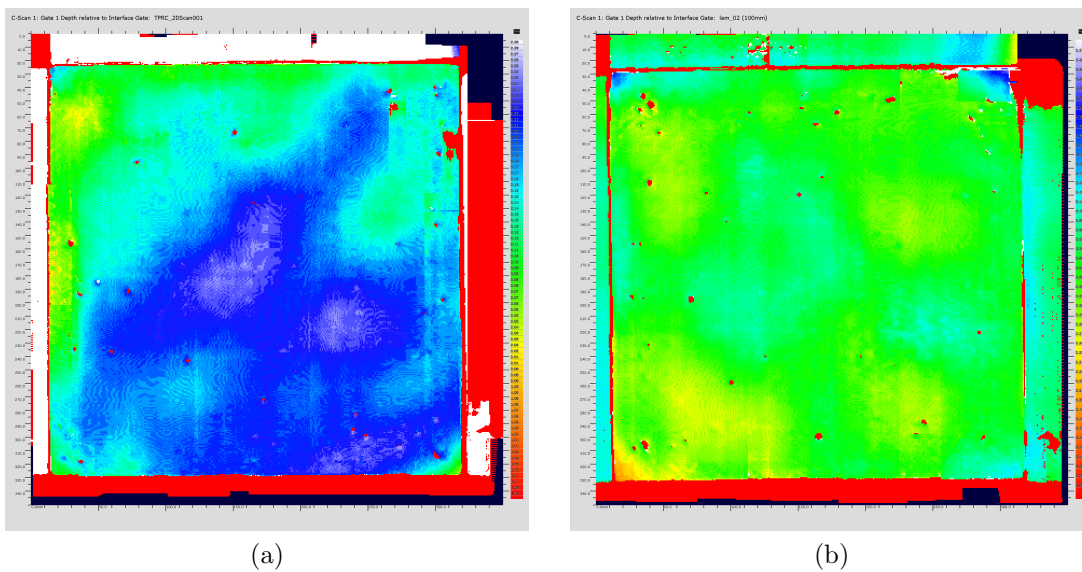


Figure 3.4: The thickness distribution of laminate 1 (a) and laminate 2 (b) with different scaling. Yellow corresponds to $\pm 2.03\text{ mm}$, and white with $\pm 2.28\text{ mm}$ for laminate 1 (a). Yellow corresponds to $\pm 2.20\text{ mm}$, and blue with $\pm 2.40\text{ mm}$ for laminate 2 (b).

The thickness of the panels is also determined with the C-scan, see figure 3.4. The first laminate fluctuates mainly between the 2.15 mm and the 2.25 mm , see appendix F. The second laminate has a thickness mainly fluctuating between the 2.27 mm and 2.37 mm . Weighing the panels, laminate 1 shows to be 327 grams and laminate 2 to be 347 grams . When also considering that the thickness of a single layer is approximately $0.13\text{-}0.14\text{ mm}$, it could indicate that laminate 2 has an extra layer. However an extra layer in laminate 2 will be highly unlikely, since only 16 layers per laminate were available during the laminate build-up. An alternative explanation for the differences in mass and thickness, could be the fabrication process. Both laminates are produced in the same mould and are separated with a metal insert. The PEKK material is therefore allowed to flow from one laminate to the other. Laminate 2 has more mass and a uniform thickness compared to laminate 1, see figure 3.4. This can indicate a material flow of PEKK of laminate 1 to laminate 2. Note that the error in the centering of the press most likely caused the non-uniform thickness.

3.2 Experimental set-up

A schematic overview of the set-up and data acquisition systems used for all experiments is illustrated in figure 3.5. The composite plate structures and the shaker are freely supported using an elastic wire, in order to isolate the structure from environmental vibrations. The electromechanical shaker is connected by a stringer and a force transducer to a corner using bee wax and is used for the low-frequency pump waves. A piezoelectric transducer (PZT), which will introduce the high-frequency carrier waves, is connected to the other corner on the other side using an adhesive and will be discussed in the next paragraph. A laser vibrometer, mounted on a x/y traverse system, measures the velocities at different points on the composite structure. The PZT and the laser vibrometer both act on the same side where the delamination is the thinnest. The PZT will be controlled by an acquisition system which will send the excitation carrier signal and acquire the velocity response. The shaker is controlled by a different acquisition system, which will send the excitation pump signal and acquire the force response.

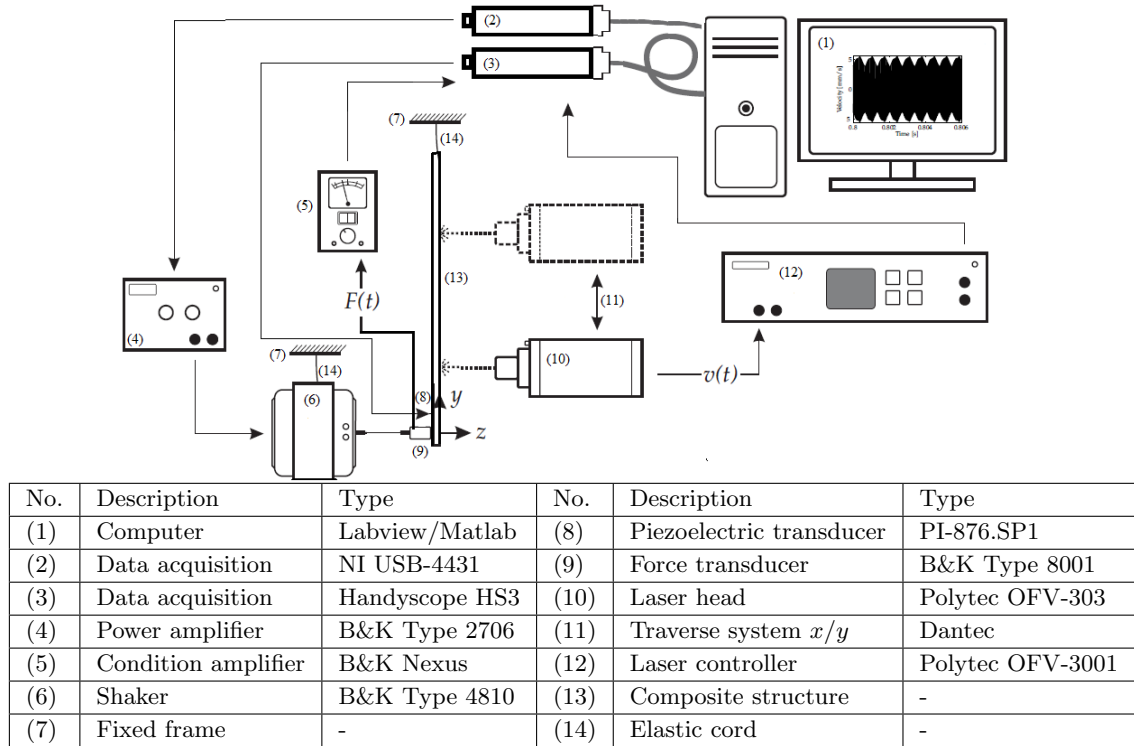


Figure 3.5: Experimental set-up, adapted from [3].

In this work, transducers from the PI Company are chosen for the creation of the carrier wave. According to the product manual [34], these transducers have an operating voltage of -100 to 400 Volt. A PZT transducer is chosen due to its small size and light weight. The drawbacks of this type of transducers are their extreme fragility and their vulnerability to damage (in the bonding) during the attachment procedure.

To investigate the bonding quality between the piezoelectric transducer and the composite structure, impedance measurements are performed. The susceptance spectrum which is the imaginary part of the admittance spectrum can be used to judge the quality of the bond between transducers and structure in SHM systems [35, 36, 37, 38]. The admittance spectrum is the reciprocal of the impedance spectrum, which could also be used for the identification of debonded transducers [39]. A M-bond 200 adhesive [40] and a Loctite epoxy adhesive [41] can be used. The details of the glue-process and the results of the impedance measurements can be found in appendix G.

3.3 Experimental procedure

The experimental process consists of multiple steps. Before the actual vibro-acoustic modulation experiments can be done, the excitation frequencies for the damaged panels should be determined. The pump frequency has to be equal to a natural frequency of the structure. These natural frequencies are only determined numerically for a pristine plate structure in section 2.4.1, and therefore the natural frequencies for both damaged structures have to be determined experimentally since there will be a different frequency shift for both delaminations. Note that there will be a difference anyway, even in pristine condition of the plates, due to the variation in thickness and other non-ideal circumstances. Finally, the interesting vibrational modes of the structures are selected from the natural frequencies. The second step consist of a high frequency sweep by the fixed PZT onto the composite structure. The velocity response is measured in the area of the delamination and on other undamaged points on the plate structure. The local natural frequencies of the delamination can then be separated from the global natural frequencies of the plate. These local natural frequencies have been determined analytically in 2.4.2. The frequencies of the first two steps can then be used as input of the final step: the vibro-acoustic modulation experiments. These three steps are described in the following three subsections and the results of the dynamic characterizations are discussed in the following section 3.4.

3.3.1 Global dynamic characterization

In the first set of experiments, the global dynamic behavior of the damaged structures is determined in terms of natural frequencies and their operational deflection shapes (ODS). During these experiments the PZT is not present on the structure and the data acquisition is done with the NI USB-4431. An excitation signal composed of a linear sweep between 250 and 3000 Hz is sent to the shaker using Labview. Using a lower starting frequency caused too much noise and irregularities in the velocity response of the laser. These irregularities seem to be caused by the higher displacement amplitudes of the measured structure and also by a cable fault, as was noticed later on. The force response is only measured at the fixed excitation point. The velocities are acquired at 49 (7×7) points, see figure 3.6.

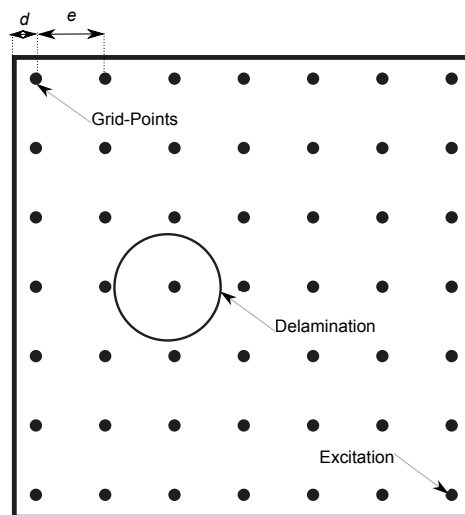


Figure 3.6: The composite plate with the delamination (circle) and the measuring grid (7×7 points). The grid-points are distributed equally with a distance $e = 50$ mm and are placed $d = 2.5$ mm from the plate edges. The excitation location is the same as the measuring location in the lower right corner but on the backside of the plate.

All signals are sent and acquired for 4 seconds with a sampling frequency of 48 kHz, which results in a 0.25 frequency resolution in the frequency spectrum of the signal. For every point these measurements are repeated 6 times. All the time responses are then multiplied with a Hanning window, Fourier transformed and averaged to obtain the power spectral densities. To

obtain the mobility frequency response functions (FRF's) $H_{F_n v_i}(\omega)$ between the fixed excitation point n and the measuring points i , the cross-power spectral density $S_{F_n v_i}(\omega)$ is divided by the auto-power spectral density $S_{F_n F_n}(\omega)$.

3.3.2 Local dynamic characterization

In the second set of experiments the local dynamic behavior of the delamination is determined in terms of natural frequencies. Differences in the frequency response functions between the locations inside and outside of the delaminated area are assumed to be the result of the local dynamic behavior of the delamination. The 'extra' peaks (natural frequencies) are assumed to be caused by the local dynamic behavior of the delamination, see figure 3.7 for a simplified and schematic example of a FRF inside a delaminated area and of a FRF mirrored around a symmetry axis of the structure. When the frequency response functions are expected to have the same structural response of the structure, an 'extra' peak can most probably be explained by a local natural frequency of the delamination.

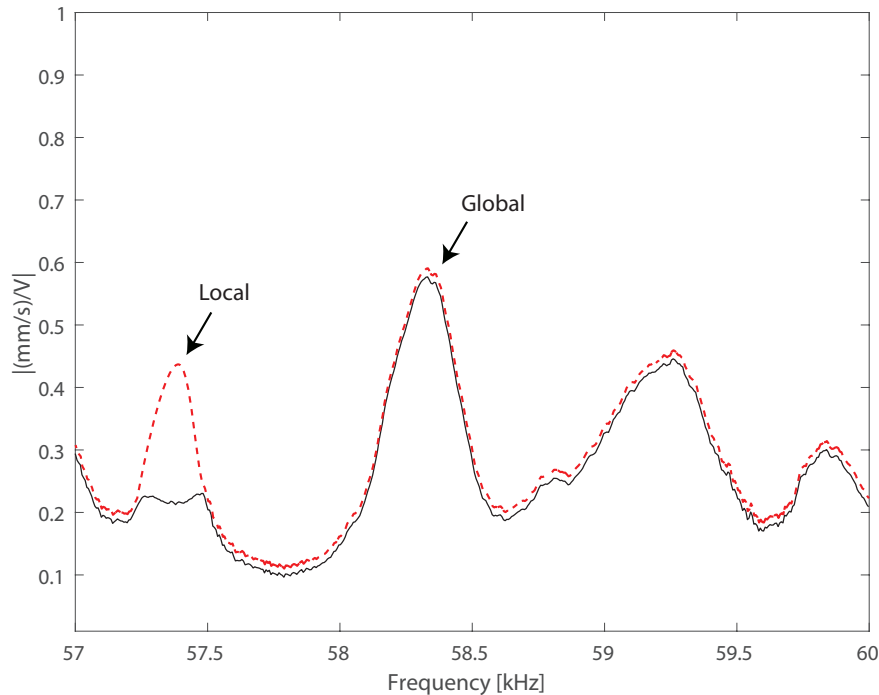


Figure 3.7: A simplified and schematic FRF inside a delaminated area (red dashed line) and of a FRF outside the delaminated area (black line) mirrored around a symmetry axis of the structure. A global natural frequency that is present for both functions is highlighted and a local natural frequency only occurring in the delaminated area is also highlighted.

The operational deflection shapes of these local modes are not in the scope of this thesis due to limitations on the experimental setup: the number of grid points are limited. An excitation signal composed of a linear sweep between 30 and 60 kHz with intervals of 1 kHz is sent to the patch transducer and the velocity response signal is measured on several locations: (1), (2), (3), (4), (5), (6) and (7), see figure 3.8. These locations correspond with the coordinates: $(x, y) = (61.6, 155), (101.6, 150), (101.6, 155), (106.6, 155), (141.6, 155), (161.6, 155), (204.3, 155)$ mm. The locations (2) and (3), (5) and (6), and (3) and (7) are mirrored around a symmetry axis of the structure, such that local and global natural frequencies can be more easily separated. The center of the delamination is expected to be around $(x, y) = (101.6, 152.5)$ mm. So the locations (2), (3) and (4) are in the middle of the delamination, (1) and (5) are located at the edge of the delamination and the remaining points are located outside of the delamination. The excita-

tion voltages of the signal for the patch transducer are also available in the time domain with a sampling frequency of 1 MHz. The response signal is acquired with a sampling frequency of 200 kHz for $\frac{128000}{200000} = 0.64$ seconds, since the buffer length of the data acquisition system is limited to 128000 samples.

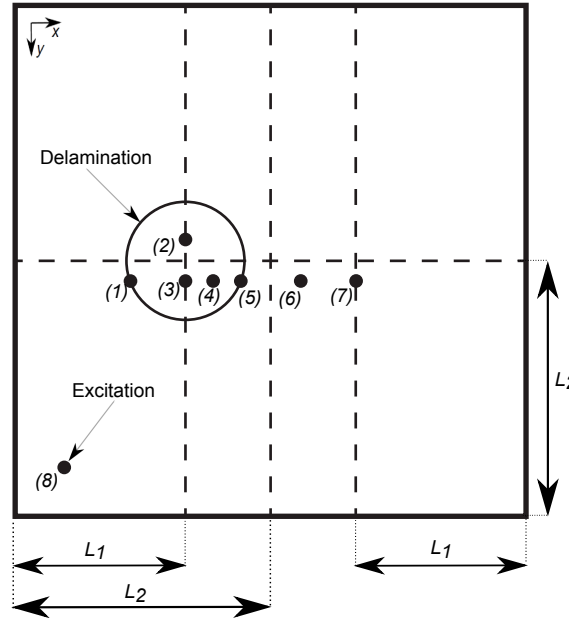


Figure 3.8: The composite plate structure with the dimensions $L_1=101.6$ mm and $L_2=152.5$ mm. The locations of the delamination, the excitation (8) and measuring points (i) (for $i=1,2,\dots,7$) are also displayed.

For every point these measurements are repeated 10 times. All the time signals are then multiplied with a Hanning window and Fourier transformed to obtain the power spectral densities. To obtain the mobility frequency response functions (FRF's) $H_{V_n v_i}(\omega)$ between the fixed excitation point n (point (8) in figure 3.8) and the measuring points i , the cross-power spectral density $S_{V_n v_i}(\omega)$ is divided by the auto-power spectral density $S_{V_n V_n}(\omega)$. Note that the frequency content of the excitation signal must cover the frequency range of interest or the results will not be valid for the portion of the frequency range not covered. Therefore the discrete sampled points in the time window of the sweep excitation are extracted and only this data set is used for the frequency response functions. This time window is dependent on the sampling frequency of the function generator of the Handyscope acquisition system because there is also a limited amount of data points available (2^{17}) for the function generator.

3.3.3 Vibro-acoustic modulation experiments

The final set of experiments are the actual vibro-acoustic measurements. Two single-tone harmonic signals with a different amplitude and frequency are simultaneously sent to the shaker (pump wave) and the patch transducer (carrier wave). The excitation amplitude and frequency of the pump frequency will be varied in the first set of experiments to find the settings that will yield in considerable signal modulations. The carrier sideband components should be sufficiently high in magnitude in the frequency spectrum. The excitation amplitude of the carrier signal is kept constant for all experiments at 12 Volt (also the maximum available voltage of the current system) since this resulted in the most sidebands and the most amplitude modulations, as also been seen in the VAM-experiments of Ooijevaar [3]. The carrier frequency is changed for different sets of experiments. These excitation carrier frequencies are equal to global natural frequencies, local natural frequencies and 'random' frequencies equal to a natural frequencies with a difference of a multiple of the pump frequency. The different results of using a global or a local natural frequency can then be investigated in the time and frequency domain.

The velocity responses and the excitation carrier voltage are simultaneously acquired at a sample rate of 1 MHz for 0.128 seconds. This is the maximum measurement time since only 128000 samples can be stored in the sampling device per measurement. A lower sampling frequency would result in a longer time period but will also result in higher amplitude errors of the sampled signal. No averaging is applied and only the steady state is considered in these VAM-experiments. A period of 2 seconds has shown to be long enough for start-up effects to disappear. The pump and carrier wave reach a steady state after the transient response has disappeared and the measuring time of 0.128 seconds is still sufficiently long to capture enough data in the steady state response. Finally the captured time responses are Fourier transformed to obtain the power spectral densities and are processed by the time domain signal decomposition approach discussed in section 2.5.2. All the results are discussed in the next chapter in detail.

The location of the velocity response measurement will however be fixed for all VAM-experiments on $(x, y)=(106, 155)$ mm, since problems of the laser vibro-meter started occurring during movement of the positioning-table due to a cable breakage. The repeatability of the VAM-experiments is therefore a point of attention. Another aspect is the fixation of the shaker to the structure, which is vulnerable for shear stresses and can influence the results. A slightly different position of the shaker will result in different response amplitudes due to the structural response on a specific position. Therefore a set of measurements is only saved when there is no replacement of the shaker and the signal strength of the laser vibrometer is kept constantly at full strength. A replacement of the shaker will be discussed and noted in the following chapter.

3.4 Experimental results of the dynamic characterization

The results of the first two sets of experiments from section 3.3.1 and section 3.3.2 are presented in this section. The relevant results used for the actual VAM-experiments are also summarized. The results of the final VAM-experiments are presented and discussed in more detail in the following chapter 4.

3.4.1 Global results

The magnitude of the total set of FRF's of the damaged plate can be seen in figure 3.9. The sharp peaks correspond with natural frequencies and are extracted in MEScope using peak picking, the bending and torsion natural frequencies are listed in table 3.1. The natural frequencies of the second fabricated plate with the smaller delamination can be found in appendix H.

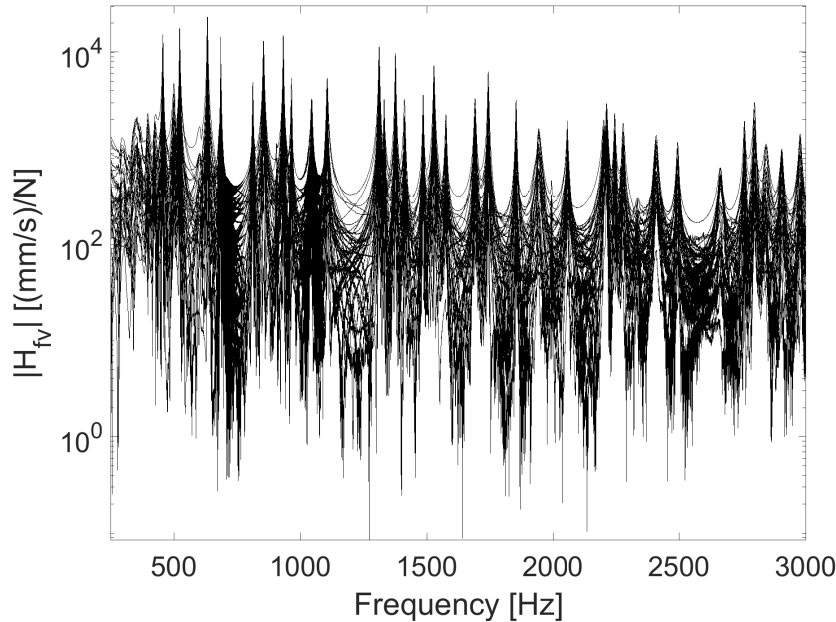


Figure 3.9: Frequency response functions $H_{F_n v_i}(\omega)$ of the damaged plate for the $i=49$ grid-points.

The accompanied ODS's are extracted at the natural frequencies and correspond with the numerically obtained mode shapes with only some differences. These differences with the numerical results are to be expected and can be explained by the present damage in the experimental structure and by the imperfect structure, see section 3.1.3. For two specific operational deflection shapes of the natural frequencies of 523 Hz and 633 Hz, see appendix H. The focus in this thesis will be on the bending dominated operational deflection shapes, since these will most probably cause the clapping behavior as stated in section 1.3.1.

Table 3.1: Natural frequencies of plate 2.

Mode	Bending B_{yz}		Torsion T_y	
n	Anslys f_B^n [Hz]	Exp f_B^n [Hz]	Anslys f_T^n [Hz]	exp f_T^n [Hz]
1	145	-	78	-
2	174	-	215	-
3	392	356	469	501
4	415	425	530	523
5	467	457	873	855
6	652	633	967	965
7	691	685	-	-
8	813	-	-	-
9	916	812	-	-
10	1047	1110	-	-

3.4.2 Local results

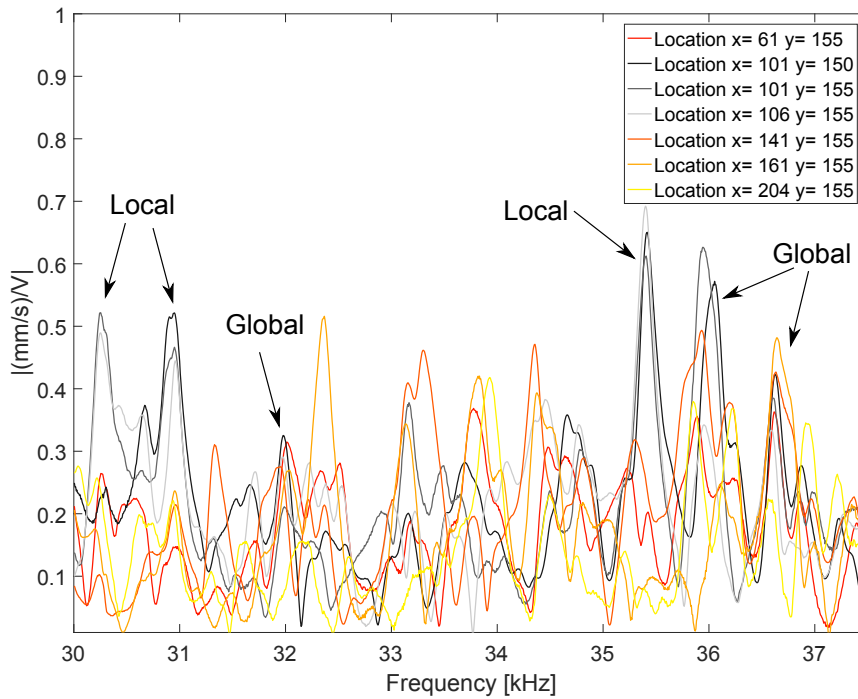
To determine local natural frequencies two different frequency windows are considered, see figure 3.10(a) and figure 3.10(b). The local and global natural frequencies can be identified and separated as been discussed in section 3.3.2 and are listed in table 3.2.

Even though that the FRF's in figure 3.10(a) and figure 3.10(b) are complex, irregular and limited in locations as compared to figure 3.9, there are still some natural frequencies recognizable. The frequencies around 30.3, 31.0, 35.4 and 59.3 kHz show to have a significant different response compared to the other points. A local frequency could also be identified around 59.9 kHz due to the fact that the locations $(x, y)=(101,150), (101,155)$ mm have a slightly different structural response compared with the other locations. The location $(x, y)=(106,155)$ mm, which is also in the center of the delamination, does not show that same behavior of structural response. However this can be explained that the location $(x, y)=(106,155)$ mm is a nodal point in the ODS of that specific local natural frequency. Comparing these experimental local natural frequencies with the obtained frequencies in section 2.4.2 is however impossible. There are only limited measuring points available and the operational deflection shapes are not re-constructable.

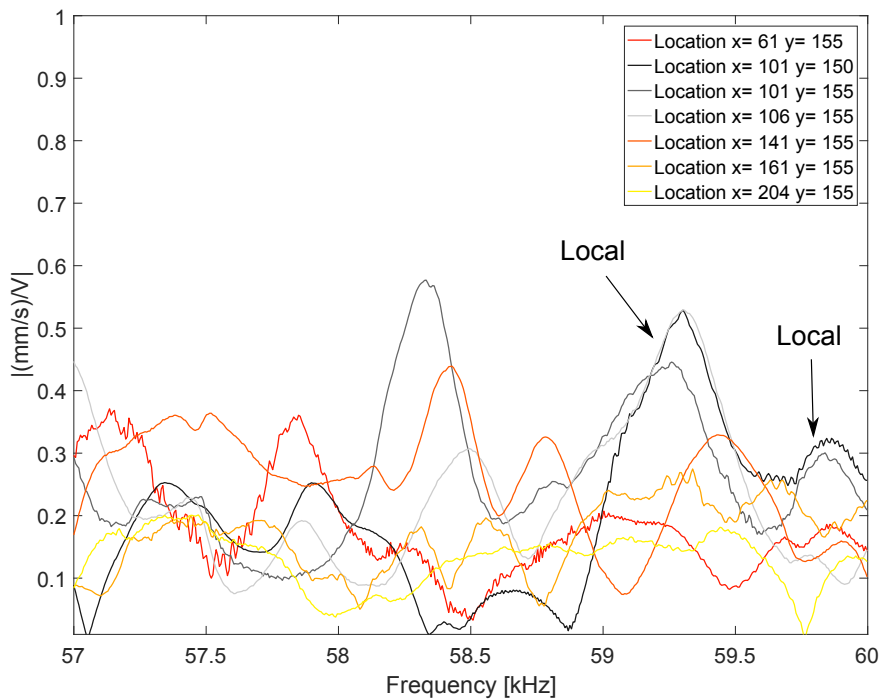
Table 3.2: Identified higher natural frequencies marked as a local or a global natural frequency.

Nature	f [kHz]
Local natural frequency	30.3
Local natural frequency	31.0
Global natural frequency	32.0
Local natural frequency	35.4
Global natural frequency	36.6
Global natural frequency	40.5
Global natural frequency	41.7
Local natural frequency	59.3
Local natural frequency	59.9

The frequencies of 32.0 kHz and 36.6 kHz in figure 3.10(a) and table 3.2 are examples of natural frequencies that are noticeable in most measured locations and can therefore be appointed as global natural frequencies that are also discussed in the previous section 3.3.1. The frequency around 32.0 kHz shows a peak for most locations and can therefore also be categorized as a global mode. The FRF of location $(x, y)=(204,155)$ mm does not show a 'peak' exactly on this frequency even though it is expected due to the symmetry of the measuring points. The difference can be explained by the imperfectness of the plate structure as discussed in section 3.1.2 or a small error in the measuring location. Not all the peaks from figure 3.10(a) and figure 3.10(b) are discussed in this thesis because a relation between different functions cannot be made due to the limited measuring points.



(a) FRF's of the frequency range 30 - 37.5 kHz.



(b) FRF's of the frequency range 57 - 60 kHz.

Figure 3.10: Frequency response functions of plate 2. The locations $(x, y)=(101,150),(101,155),(106,155)$ mm correspond to the center of the delaminated area and are colored gray/black. The locations $(x, y)=(61,155),(141,155)$ correspond to the edges of the delamination.

3.4.3 Summary

The results from section 3.4.1 and section 3.4.2 can be used for the final VAM-experiments. The lower natural frequencies discussed in section 3.4.1 with the bending dominated operational deflection shape can be used as pump frequency for the clapping behavior. Other natural frequencies can be used to study the signal modulations for those excitation pump waves. The excitation amplitude of the pump and the carrier frequency will stay constant through these first set of experiments. The carrier frequency is equal to the 50 kHz as also used by Ooijevaar [3]. For the second set of VAM-experiments the gain of pump is varied for the optimization of the pump excitation amplitude. Now that the excitation parameters of the pump wave are determined, the carrier wave can be optimized. The final set of VAM-experiments contains the variation of the carrier frequency and the frequencies from section 3.4.2 can be used. The excitation carrier frequencies are equal to global natural frequencies, local natural frequencies and ‘random’ frequencies equal to a natural frequencies with a difference of a multiple of the pump frequency. The location of the velocity response measurement will however be fixed for all VAM-experiments since problems of the laser vibro-meter started occurring during movement of the positioning-table due to a cable breakage. Note that the fixation of the shaker also has to stay intact for the measurement set to be added in the final chapter with the VAM-experiments. All these final results of the VAM-experiments are discussed in the next chapter in detail and a repositioning of the shaker will be noted in between different sets of measurements.

Chapter 4

Experimental results and discussion

The experimental results of the VAM-experiments are presented and discussed in this chapter. All the results are for a single measurement point $(x, y) = (106, 155)$ mm in the delaminated area on plate with a delamination of $R = 50$ mm for a steady state caused by the two single-tone harmonic excitation signals. The results are compared with the work of Ooijevaar [3] and possible explanations are formulated and discussed. The main topic is the effect of the underlying dynamic behavior on the measured modulations. The selection of the carrier frequency for the discussed VAM-method influences the occurring amplitude modulations that are used by Ooijevaar for damage detection [3].

4.1 Pump wave

For the first VAM-experiments the complete frequency spectra of the total response signal are discussed for different excitation parameters. The different frequency components such as potentially higher harmonics and sidebands can be identified. A selection for the pump frequency and amplitude is done in the following two sections with a constant carrier wave of 50 kHz and 12 Volt. This is followed by a section that discusses the excitation carrier wave. Ooijevaar uses two pump frequencies with a clapping and kissing operation deflection shape with a constant carrier frequency of 50 kHz [3]. This section illustrates that the selection of the pump wave is not that straightforward and simple. The desired damage mechanisms for this thesis is a clapping behavior. The expected natural frequency for clapping will be 633 Hz as shown in table 3.1 due to location of the maximum structural response. The numerically obtained mode shape for this bending frequency is illustrated in figure 2.6. The excitation amplitude of the pump wave has to be high enough to cause opening and closing behavior.

4.1.1 Pump frequency

The natural frequencies of the composite plate are listed in table 3.1. All the bending and torsion modes are used as the pump frequency but the natural frequencies of 423, 501, 633 and 685 Hz are only discussed since these give the most interesting results. The Fourier spectra of the velocity responses are shown in figure 4.1 and the time response of the pump frequency of 633 Hz is given in 4.2. All the spectra show even and odd sidebands and higher harmonics and indicate that the nonlinearity in the structure tends to be more a quadratic than a cubic type of nonlinearity, as is indicated in figure 2.2. Figure 4.1(b) and (c) clearly give the most sidebands and higher harmonics. This can be explained by the fact that these frequencies have the highest structural response, as can be seen in figure 3.9. The sidebands (and higher harmonics) in figure 4.1(c) have in their turn the highest amplitude and are therefore the most present in measured response signal. The central carrier peak in the response also has the highest amplitude of the 4 different carrier frequencies. When taking into account the ODS of the 501 and 633 Hz pump

frequencies, the first one is a torsion mode with a higher structural response than predicted with the numerical model and the latter is a bending mode. The 633 Hz is assumed to cause the opening and closing of the delamination and the plate is designed such that the delamination lays in a maximum of the accompanying ODS. The largest number of signal modulations is expected and also occurs for this pump frequency. The amplitude modulation M_a [mm/s] of these 4 different cases are respectively: 0.16, 0.21, 0.24 and 0.13 mm/s.

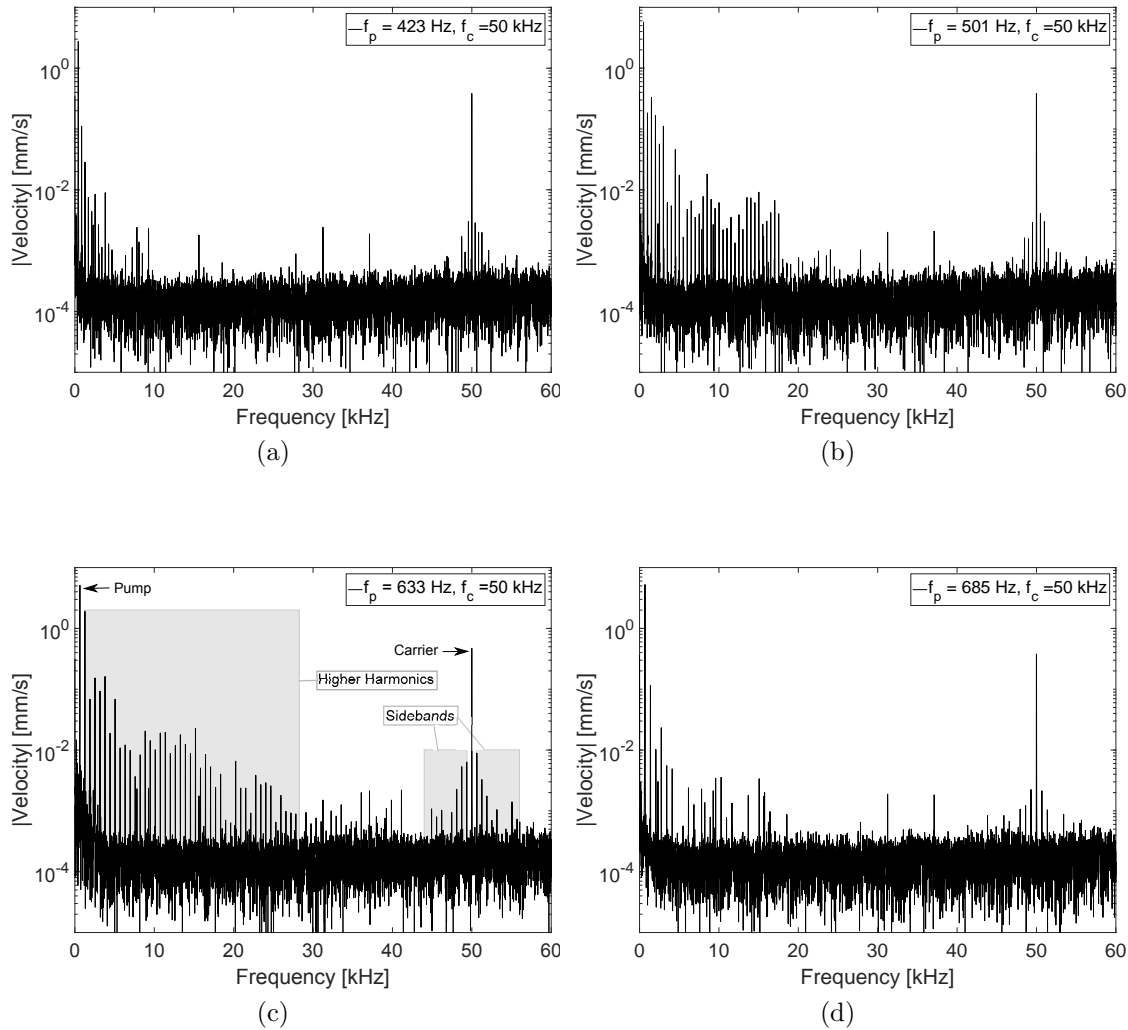


Figure 4.1: The Fourier spectra up to 60 kHz of the velocity responses with the pump frequency equal to 423 Hz(a), 501 Hz(b), 633 Hz(c) and 685 Hz(d). The excitation amplitude of both the carrier and pump are kept constant as is the carrier frequency of 50 kHz. The pump and carrier frequency are highlighted in (c). The frequency ranges containing the higher harmonics nf_p , the sidebands $f_c - nf_p$ and the sidebands $f_c + nf_p$ are also highlighted in (c) (for $n=1,2,3,\dots$).

4.1.2 Pump amplitude

The current section discusses the excitation amplitude of the previously chosen pump frequency. Three different excitation gains G_p are used for the pump wave: a weaker, an average and a stronger gain. The first two are plotted respectively in figure 4.2 for a specific time domain.

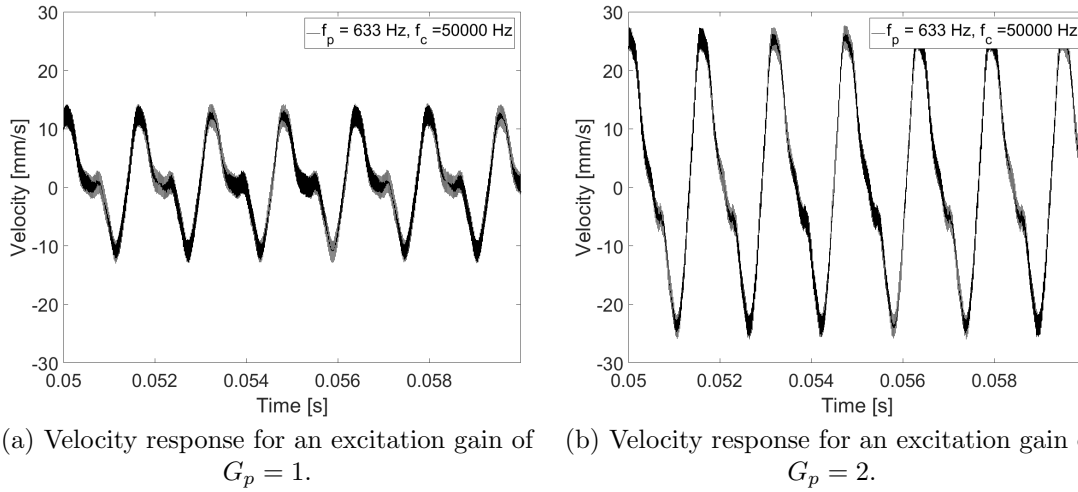


Figure 4.2: The time signal for a specific time window for a pump frequency of 633 Hz with varying excitation amplitudes. The carrier wave is 50 kHz with an excitation amplitude of 12 Volt.

Ooijevaar [3] has shown that increasing the pump amplitude will result in increasing amplitude modulations. The measuring location (undamaged or damaged) does have a strong influence on the relation between the amount of amplitude modulation and excitation pump amplitude, even though this relation is not consistent, see figure 2.3. To see what this relation is for the current structure and damage scenario in the location $(x, y) = (106, 155)$ mm, the high frequency response is separated by using the bandpass filter as discussed in section 2.5 to the discussed signals in figure 4.2. The three different phases caused by the clapping mechanism, seen in figure 1.6, can be distinguished in these time responses. The discontinuity is representative for the contact phase in which the wave is mostly distorted. A narrow band filter is applied at a frequency window around the carrier frequency between $f_c - 10$ kHz and $f_c + 10$ kHz to obtain a bandpass response with only the carrier frequency and the dominant sideband components. The resulting narrow band velocity response is shown in figure 4.3. The oscillating signal envelope indicates that amplitude modulation effects are present, especially for the response with the higher pump gain.

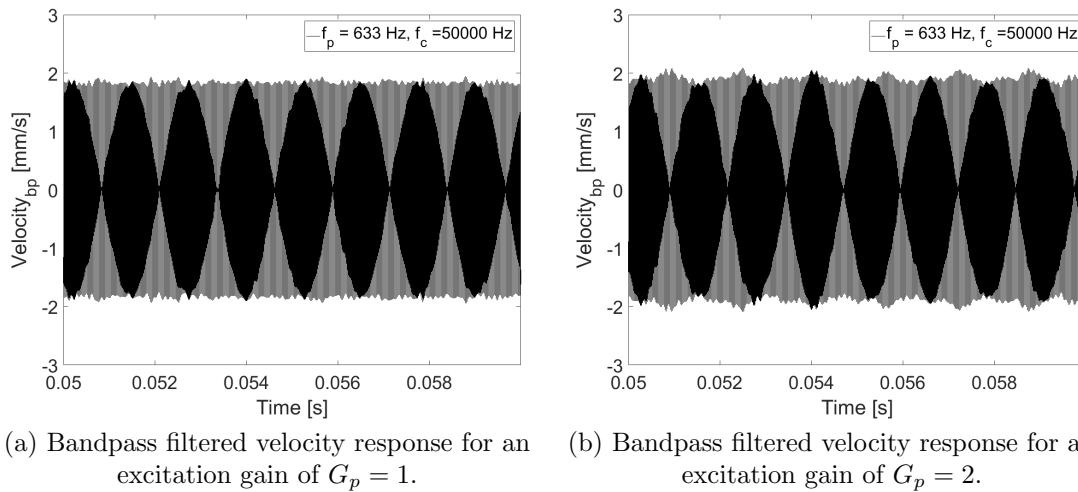
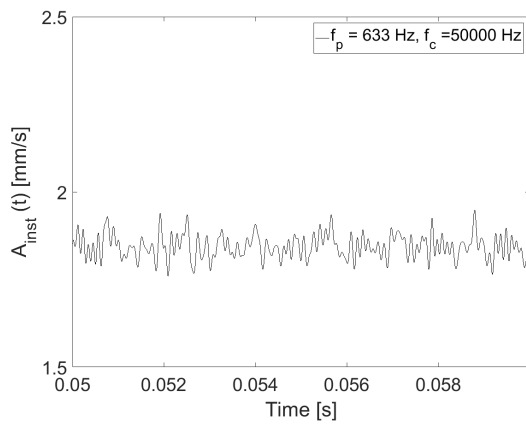


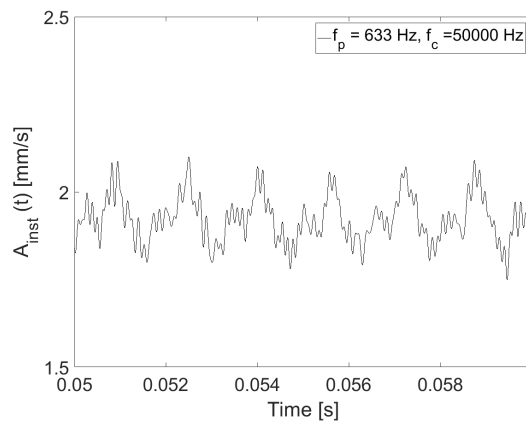
Figure 4.3: The bandpass filtered velocity response within a $f_c \pm 10$ kHz frequency range for a specific time window for a pump frequency of 633 Hz with varying excitation amplitudes. The carrier wave is 50 kHz with an excitation amplitude of 12 Volt.

To obtain this amplitude modulation for both the responses the Hilbert Transform has to be

applied to the signals in figure 4.3, as was described in section 2.5 and appendix C. The obtained instantaneous amplitude is shown in figure 4.4(a) and 4.4(b). The amount of amplitude modulation (peak-to-peak value) for the pump gain of 1 is equal to 0.19 m/s and for the pump gain of 2 is equal to 0.35 m/s. The amount of amplitude modulation clearly increases for higher pump amplitude levels but not linearly. The minimum value of both instantaneous amplitude functions is roughly the same, only the maximum value increases for the higher gain. This can be explained by the opening and closing behavior that is most probably not that strong for a gain of $G_p=1$ than for a gain of $G_p=2$. For higher pump excitation forces that cause the opening and closing of the delamination, the higher carrier excitation has the capability for a higher amplitude response in the opened delamination state. However a limit is expected on the amplitude modulation, it will most probably not increase above a certain pump excitation amplitude during elastic deformations.



(a) Instantaneous amplitude for a gain of 1.



(b) Instantaneous amplitude for a gain of 2.

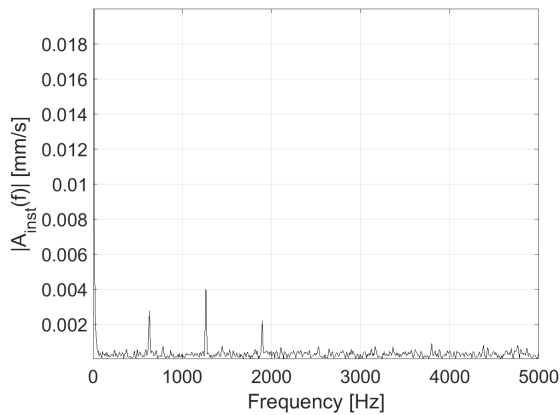
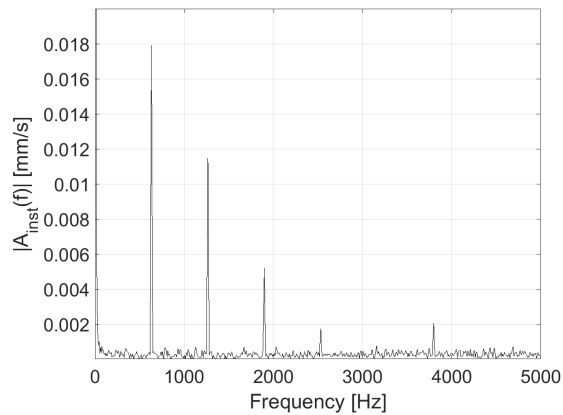

 (c) Fourier spectrum of $A_{inst}(t)$ for a gain of 1.

 (d) Fourier spectrum of $A_{inst}(t)$ for a gain of 2.

Figure 4.4: The instantaneous amplitude $A_{inst}(t)$ for a pump gain of 1 (a) and 2 (b) of the bandpass filtered velocity response $v_{bp}(t)$ measured at location $(x, y) = (106, 155)$. The Fourier spectra (c) and (d) reveal the frequency content of $A_{inst}(t)$.

When the frequency content of the instantaneous amplitude function for the gain of 1 and 2 is investigated in figure 4.4(c) and 4.4(d), the pump frequency and its higher harmonics can be clearly distinguished. The instantaneous amplitude function of figure 4.4(b) seems to be more harmonic and the excitation pump frequency of 633 Hz is more dominant with the higher pump excitation force. A possible explanation that also explains the higher pump amplitude for the higher gain, can be that the opening and closing behavior of the delamination is more prominently present. It is expected that for increasing pump excitations the amplitude of the pump frequency

will increase relatively more than the amplitude of the sidebands due to the more pronounced opening and closing behavior of the delamination. Note that the total energy of figure 4.4(d) should be roughly twice the amount of figure 4.4(c). The latter also indicates that figure 4.4(b) is more harmonic than figure 4.4(a).

When comparing the amount of amplitude modulations with the results of Ooijevaar [3], the obtained amplitude modulations of Ooijevaar are a factor 5 greater. The magnitude of the pump frequency in the instantaneous amplitude from figure 4.4(c) and 4.4(d) are respectively a factor 200 and 30 greater in the work of Ooijevaar. The amplitude of the higher harmonics compared to the pump frequency amplitude in the current research is however much stronger than in the research by Ooijevaar [3]. The difference between his study and this study can possibly be in the magnitude of the pump excitation, the type of structure (T-beam versus plate) and the damage type (skin-stiffener debonding versus artificial delamination). It is possible that the pump wave cannot cause the opening and the closing of the delamination as strong in this study compared to the work of Ooijevaar [3]. Another reason for the difference could be that the carrier wave is too weak for proper excitation of the delaminated face in this study. Also the layout and shape of the delamination can be different than the intended circular shape and can have influence on the damage behavior and the resulting signal modulations in this study.

The pump amplitude is not restricted by the shaker but by the capabilities of the laser vibrometer, with a too high excitation amplitude the laser is not capable of measuring the high velocities due to the high displacements. The carrier amplitude is currently restricted by the output voltage of the data acquisition system.

4.1.3 Pump wave selection

The optimal pump wave for the VAM-method has a relative high amount of (amplitude) modulations in the damaged area compared to the undamaged area. This can however not be checked in this thesis due to the limited amount of measuring points. Therefore the pump frequency of 633 Hz with the highest amount of modulations in the damaged location $(x, y) = (106, 155)$ mm, and the expected clapping behavior, is used for the further VAM-experiments. Note that the sidebands in figure 4.1 are not an indication of amplitude modulation, since the sidebands can contain both amplitude and frequency modulation.

Based on the results of the damaged location $(x, y) = (106, 155)$ mm, a higher pump excitation amplitude seems to result in a more pronounced opening and closing behavior of the delamination. The pump excitation frequency will be more pronounced in the frequency content of the instantaneous amplitude for these higher excitation amplitudes and results in a more harmonic instantaneous amplitude function. Since it is expected that the damaged location can be better identified for the higher amplitude modulations values, it is recommended that the pump excitation force has to be as high as possible. This will also result in a relative high pump frequency amplitude compared to the higher harmonic amplitudes in the Fourier spectrum of the instantaneous amplitude. Note that the pump excitation force will not become too high since it is expected that a limit on the amount of amplitude modulation is expected for increasing pump excitation forces and that the elastic behavior will transform into plastic behavior. The latter is not desirable ofcourse. For the following VAM-experiments the pump frequency of 633 Hz is used with the pump excitation amplitude also used in figure 4.4(b) and 4.4(d).

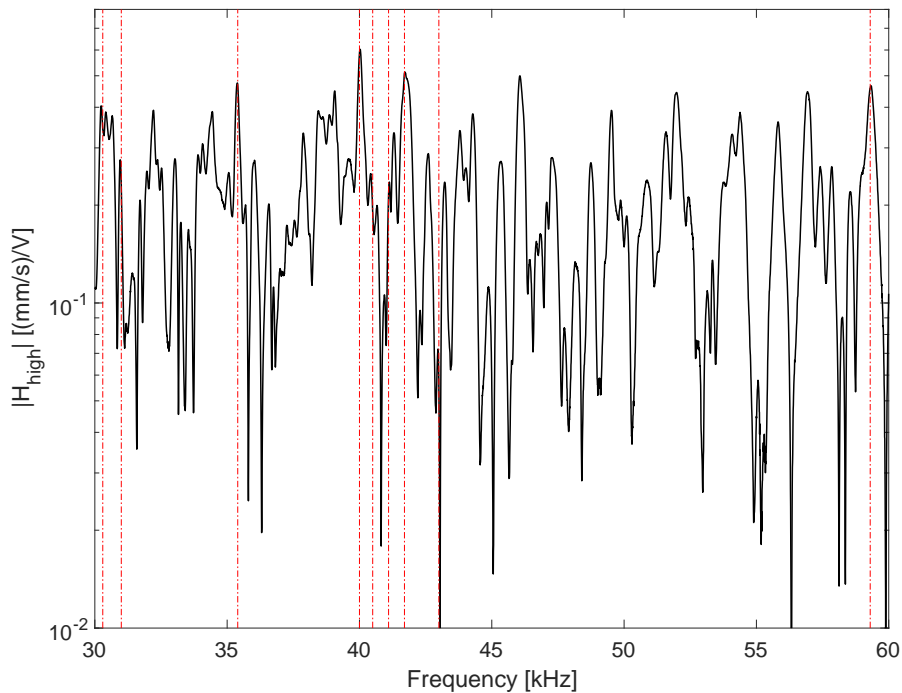
4.2 Carrier wave

The parameters for the pump wave are selected in the previous section such that the carrier frequency can be investigated in this section. The excitation force of the carrier wave is chosen constant for all the VAM-experiments in this thesis. The shaker connection is reattached for the measurements in this section and since this location will have influence on the obtained results, they cannot be compared to the results from the previous section directly.

Table 4.1: The different carrier frequencies and their ‘nature’ on location $(x, y) = (106, 155)$.

Nature	f_c [kHz]
Local natural frequency	30.3
Local natural frequency	31.0
Local natural frequency	35.4
Global natural frequency	40.0
Global natural frequency	40.5
‘Random’ frequency: $41.7 - f_p$	41.1
Global natural frequency	41.7
‘Random’ frequency: $41.7 + 2f_p$	43.0
Local natural frequency	59.3

The frequencies used as carrier frequency are listed in table 4.1. This list contains four (possible) local natural frequencies, 3 three global natural frequencies and 2 frequencies that are a global natural frequency plus or minus a twofold of the pump frequency. The frequency response function for the considered location $(x, y) = (106, 155)$ mm in this section is given in figure 4.5, in which the different carrier frequencies are also highlighted. With the results of these different carrier frequencies, a lot of observations can be made. These are discussed in the following subsections. First the Fourier spectra of the bandpass filtered response are discussed followed by the instantaneous amplitude functions.


Figure 4.5: The magnitude of the frequency response function at location $(x, y) = (106, 155)$ mm. The carrier frequencies are highlighted by the red and dashed vertical lines.

4.2.1 Bandpass frequency spectra

Four different bandpass velocity responses $v_{bp}(t)$ for different carrier frequencies are shown in figure 4.6. Only these four frequencies are discussed in this subsection because they gave the most interesting results.

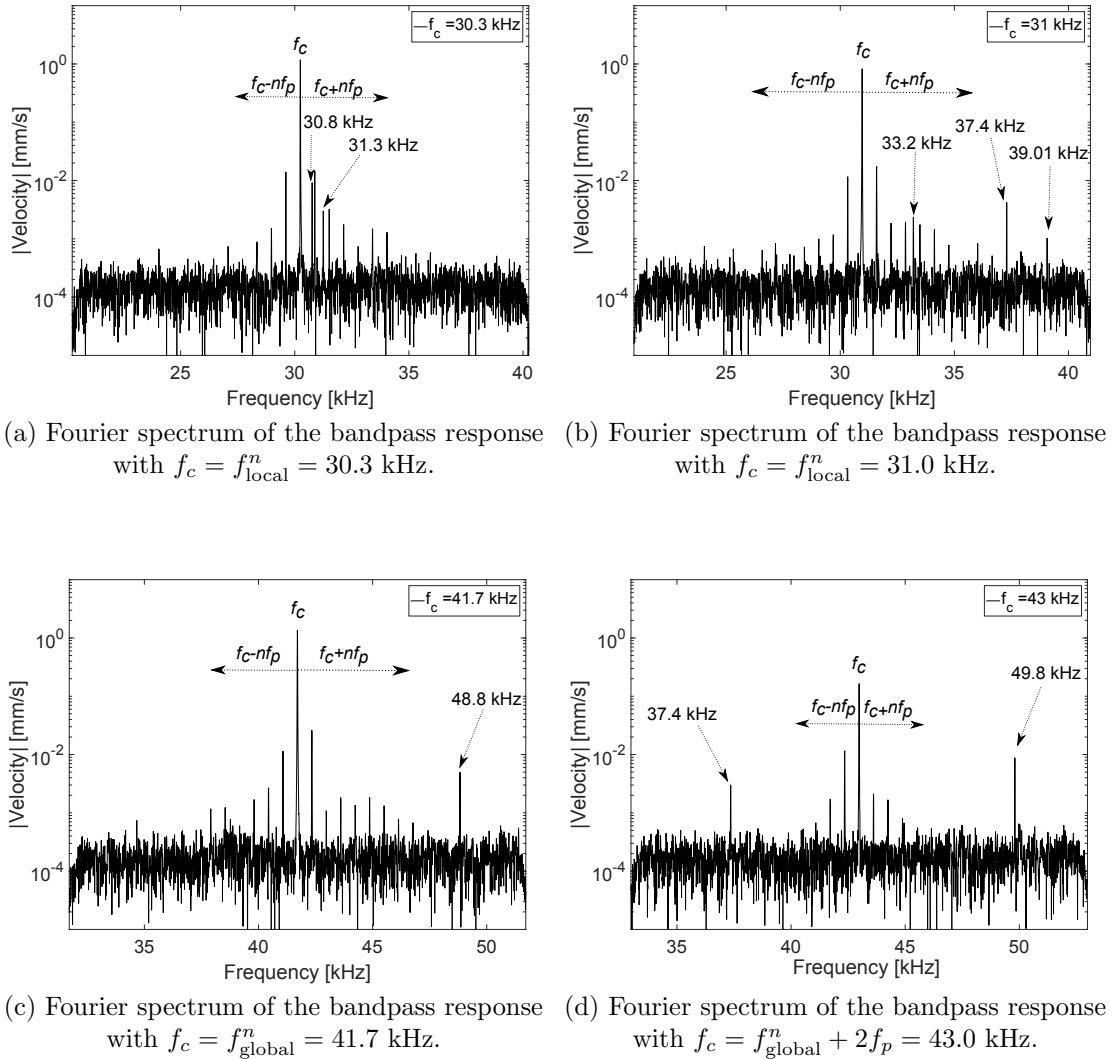


Figure 4.6: The bandpass filtered velocity response within a $f_c \pm 10$ kHz frequency range for a specific time window for a pump frequency of 633 Hz with a carrier frequency of 30.3 kHz (a), 31.0 kHz (b), 41.7 kHz(c) and 43.0 kHz (d) on location $(x, y) = (106, 155)$. The excitation amplitudes are the same $G_p = 2$ and $F_c = 12$ Volt. The frequency ranges in which the sidebands are present and the ‘strange’ frequency components are highlighted.

The carrier frequency used in figure 4.6(a) is 30.3 kHz and corresponds to a local natural frequency. The differences with the Fourier spectra obtained in the previous section is that there are suddenly frequency components at $f_c + 519$ Hz (30.8 kHz) and $f_c + 1007$ Hz (31.3 kHz) and are unequal to an expected sideband frequency. These frequency components do not coincide with a natural frequency in figure 4.5. Considering the frequency differences with the carrier, the frequencies of 519 Hz and 1007 Hz are also not present in the low frequency response of the signal, see figure 4.7. These frequencies differences are also not noticed for the other carrier frequencies. When this frequency deviation is however compared with the natural frequencies obtained in the low frequency regions it seems that this 519 Hz corresponds well with the fourth torsion mode. The small deviation of 4 Hz can be explained due to limited frequency resolution of the FFT. The fact that this frequency is not noticed in figure 4.7 could be due to the ODS of this mode. There is nodal point near the location where the velocity responses are obtained.

A similar ‘strange’ frequency component is also present between the sidebands in figure 4.6(b). This frequency of 33.2 kHz ($f_c + 2240$ Hz) is unequal to an expected sideband frequency but it could possibly correspond with a natural frequency, even though it has a low structural response

(0.18 (mm/s)/V) on the considered location. For this carrier no further explanation for the frequency deviation of 2240 Hz can be given looking at the frequency response function.

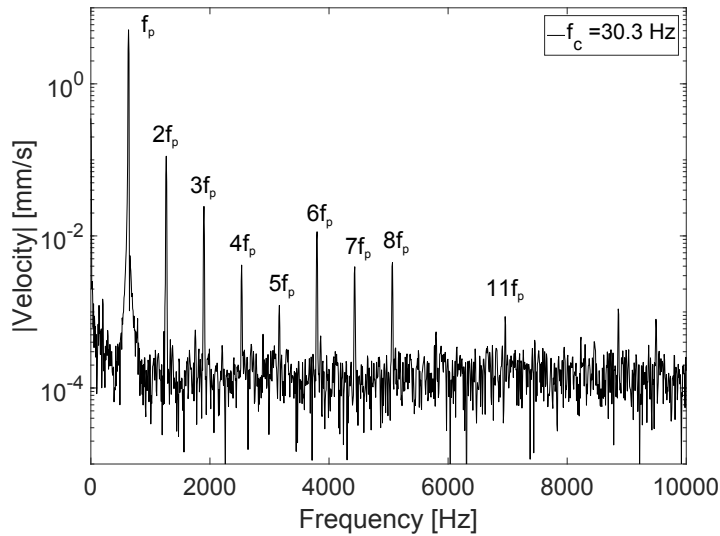


Figure 4.7: Fourier spectrum of the lower frequency region of the response signal on location $(x, y) = (106, 155)$ with $f_p = 633$ Hz and $f_c = 30250$ Hz.

In figure 4.6(b) and 4.6(d) there is a mutual frequency component at 37.4 kHz present relatively far apart from the central carrier frequency that is not equal to the carrier frequency plus or minus a multiple of the pump frequency. This frequency has a relatively low structural response (0.15 (mm/s)/V) and does not correspond with a natural frequency as can be seen in figure 4.5. The other sideband around 49.8 kHz in figure 4.6(d) corresponds with a possible global natural frequency, but again it has a relatively low structural response (0.20 (mm/s)/V). The central carrier frequency as well as the direct sidebands in this figure have a lower magnitude compared to the figures 3.10(a), (b) and (c). Also the number of sidebands are clearly less in figure 4.6(d). This is due to the fact that the carrier frequency of 43.0 kHz does not correspond with a natural frequency of the structure. Note that a sideband at $43.0 - 2f_p = 41.7$ kHz is not stronger in magnitude than the other sidebands, even though 41.7 kHz corresponds with a possible global natural frequency. This can probably be explained by the relative low structural response at this frequency.

The sideband of $43.0 - f_p = 41.7 + f_p = 42.3$ kHz is however relatively strong in magnitude compared to its carrier in both figure 4.6(c) and (d), even though the sideband has a value of 0.026 mm/s in figure 4.6(c) and of 0.009 mm/s in figure 4.6(d). The latter could indicate that the sidebands are not only a function of the underlying structural response of the structure independent on the choice of the carrier frequency, but that the magnitude of the sidebands are also a dependent on the carrier frequency. A possible relation was already given in equation (2.19) analytically.

In figure 4.6(b) there is a frequency component at 39.01 kHz and in figure 4.6(c) there is also a frequency component at 48.8 kHz. Again, these do correspond well with a global natural frequency of the structure both with a structural response of respectively 0.45 (mm/s)/V and 0.27 (mm/s)/V.

From the previous results and observations it can be concluded that there is variation in the ‘creation’ of sidebands. The response signal will be more modulated for choosing a global or local natural frequency as carrier frequency, i.e. the amount of sidebands does increase. The magnitude of a sideband seems to have a relation with the underlying structural response of the structure and the selected carrier excitation but this relation is not always consistent. Especially the frequency components highlighted with a specific value in figure 3.10 are ‘strange’. They cannot

be explained since they are not equal to the carrier frequency plus or minus a multiple of the pump frequency and these frequencies do not (all) coincide with a natural frequency. Note that these frequencies are present in the narrow band response signal and will therefore have influence on the instantaneous properties discussed in the following sections for only those four carrier frequencies. Finally it has to be stated that these frequencies for a specific carrier frequency are present in multiple measurements, these unexpected frequencies are therefore probably not the cause of ‘noise’.

Yoder et al. [29] have already stated that there is a strong correlation between the amplitude of the carrier sidebands and the magnitude of the underlying spectral response of the damaged structure. Theoretical derivations from section 2.3 and the results from this section support this claim.

4.2.2 Instantaneous amplitude

The Fourier spectra of the bandpass filtered velocity responses are discussed in the previous section. This and the following section will discuss the instantaneous amplitude and frequency functions obtained with the Hilbert Transform, as was described in section 2.5 and appendix C.

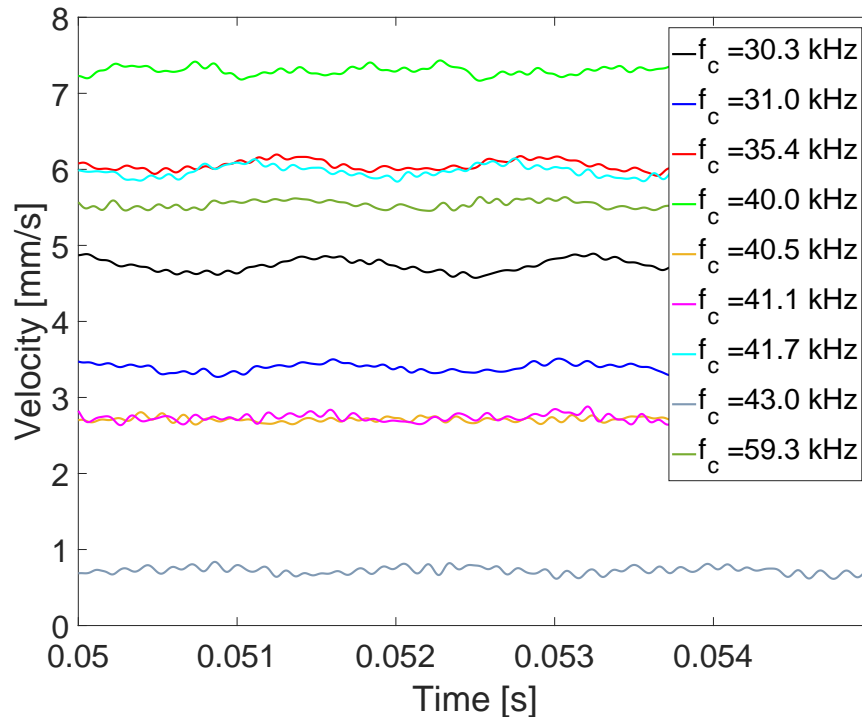


Figure 4.8: Instantaneous amplitude for different carrier frequency on the location $(x, y) = (106, 155)$. The excitation parameters $f_p = 633$ Hz, $G_p = 2$ and $F_c = 12$ Volt are kept constant.

The instantaneous amplitudes are illustrated in figure 4.8. Note that the phase differences between the different instantaneous functions cannot be discussed due the ‘random’ activation of the shaker for the pump excitation. The nature of the carrier frequencies and their accompanied amplitude and frequency modulation are given in table 4.2. The structural response obtained from figure 4.5 is also listed and finally the data of the different carrier frequencies is ranked on descending average envelope.

Table 4.2: The carrier frequencies used for the VAM-experiments in this section with their average magnitude of the instantaneous amplitude function $A_{inst}(t)$. The structural response of these frequencies is obtained from the frequency response function at location $(x, y) = (106, 155)$. The amplitude M_a [mm/s] and frequency M_f [Hz] modulation values are also given.

Nature	f_c [kHz]	Structural response $H(\omega)$ [(mm/s)/V]	$A_{inst}^{Avg}(t)$ [mm/s]	M_f [Hz]	M_a [mm/s]	$R = \frac{A_{inst}^{Avg}(t)}{H(\omega)}$ [V]	$R_2 = \frac{R}{M_a}$ [V/(mm/s)]
G	40.0	0.61	7.29	109.77	0.21	11.95	56.9
L	35.4	0.48	6.06	173.27	0.28	12.63	45.1
G	41.7	0.52	5.96	182.01	0.29	11.46	39.5
L	59.3	0.47	5.56	170.15	0.18	11.83	65.7
L	30.3	0.41	4.72	138.43	0.33	11.51	34.9
L	31.0	0.28	3.38	249.95	0.26	12.07	46.4
R	41.2	0.18	2.74	396.97	0.19	15.66	80.1
G	40.5	0.16	2.71	278.35	0.14	16.94	121.0
R	43.0	0.07	0.72	1580.82	0.29	10.29	35.5

The first observation from figure 4.5 is that the magnitude of the instantaneous amplitude $A_{inst}(t)$ functions differs a lot. The envelope has a clear relation with the magnitude of the frequency response function from the measured location, see table 4.2. The carrier frequency of 40.0 kHz has the highest magnitude of the instantaneous amplitude functions, this corresponds with figure 4.5 in which the frequency 40.0 kHz has the highest structural response (0.61 (mm/s)/V). This conclusion also holds for the results of Ooijevaar [3]: the magnitude of the instantaneous amplitude clearly increases if the carrier frequency has a higher structural response in the frequency response function. The exact values are not known but there is a clear difference in the magnitude of the FRF's of Ooijevaar even though the difference is minimal.

The ratio R between the structural response for a specific carrier frequency and the average instantaneous amplitude is calculated and given in table 4.2. The excitation amplitude of 12 V is clearly reflected. The ratios R belonging to the carrier frequencies 41.2 kHz and 40.5 kHz are however higher than 12 V and indicate that the actual response is higher than expected, the exact relation is not found.

This relation does however not explain the different obtained amplitude modulations for varying carrier frequencies. The small parametric study of Ooijevaar on the variation of the carrier frequency of 48, 50 and 52 kHz already shows high variation in the obtained amplitude modulations. The phase and magnitude of the instantaneous amplitude differ between the 3 situations. The frequency content of the instantaneous amplitude functions $A_{inst}(t)$ is not investigated and therefore no further conclusions can be drawn from the study by Ooijevaar [3].

Taking into account the previously determined local natural frequencies of the delamination, some local natural frequencies of the delamination show a higher amplitude modulation. This can be seen in table 4.2. The relatively high amplitude modulations of the carrier frequency 43.0 kHz can possibly be explained by the sidebands discussed in the previous section that appeared at 'random' frequencies relative far away from the carrier frequency. A second ratio R_2 is calculated by dividing the previously obtained ratio R by the acquired amplitude modulation M_a . This ratio R_2 indicates how sensitive the actual structural VAM-response for a specific carrier frequency is to amplitude modulation, i.e. lower values indicate more amplitude modulation for a specific structural response. The local carrier frequency of 30.3 kHz shows to have the best amount of amplitude modulation. Only the R_2 ratio of the carrier frequency of 43.0 kHz is unexpected high, caused by the relative high amount of amplitude modulation.

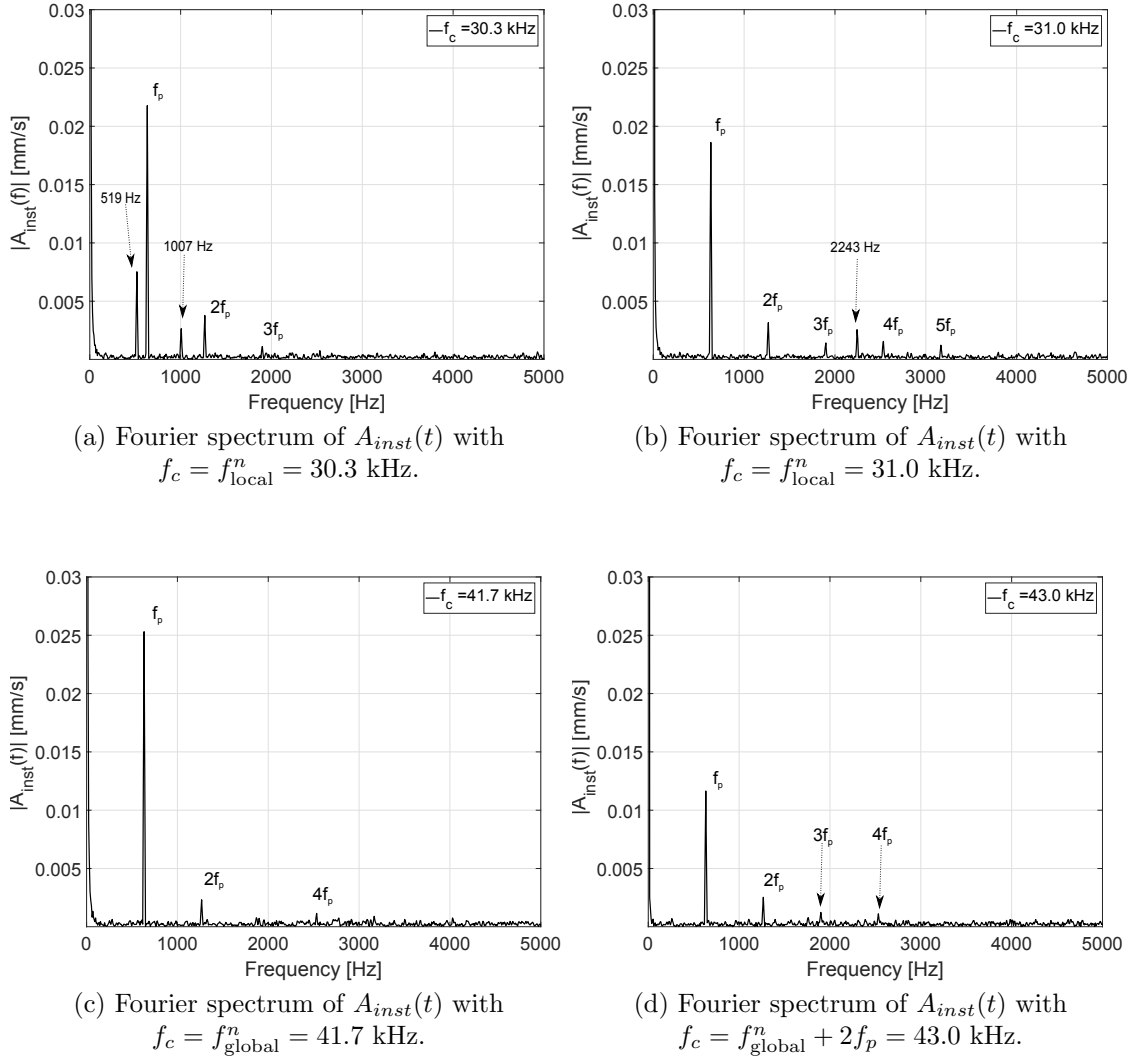


Figure 4.9: $A_{inst}(t)$ for a pump frequency of 633 Hz with a carrier frequency of 30.3 kHz (a), 31.0 kHz (b), 41.7 kHz(c) and 43.0 kHz (d) on location $(x, y) = (106, 155)$. The excitation amplitudes are the same $G_p = 2$ and $F_c = 12$ Volt.

When the frequency content of the instantaneous amplitude is investigated, especially those of 30.3 kHz and 31.0 kHz are interesting since there are extra frequency components present next to the frequencies equal to the pump and higher harmonics, see figure 4.9(a) and 4.9(b). The Fourier spectrum in figure 4.9(a) shows frequencies at 519 Hz and 1007 Hz that are already noticed in the Fourier spectrum of the bandpass filtered response in section 4.2.1. In figure 4.9(b) there is clearly a frequency present at 2243 Hz next to the pump frequency and multiple higher harmonics. The frequency content of the envelope functions from the 41.7 kHz and 43.0 kHz are similar, however they only contain the expected pump frequency and higher harmonic(s), see figure 4.9(c) and 4.9(d).

From these observations it can be concluded that using a local or global natural frequency as carrier increases the magnitude of the pump frequency in the frequency content of the instantaneous amplitude. Furthermore for only the two specific local natural frequencies (30.3 kHz and 31.0 kHz), there are unexpected frequencies present. Even though they the presence frequencies cannot be explained in this thesis, they could be used for improving and understanding the VAM-method. As can be seen in table 4.2, the carrier frequency of 30.3 kHz has to most amplitude modulation, most probably due to this ‘extra’ frequency content.

The acquired amplitude modulation and frequency content of the instantaneous amplitude functions in this section are different compared to section 4.1.2. Comparing the frequency content

of the instantaneous amplitude in figure 4.9(a), (b), (c) and (d) to figure 4.4(c) and (d), the differences are considerable. The pump frequency increased in magnitude in figure 4.9(a), (b) and (c) compared to 4.4(d), however the magnitude of these higher harmonic frequencies decreased considerable. This is most probably caused due to changes in the original velocity response $v(t)$ in this section. The number of higher harmonics are decreased and the actual higher harmonic magnitudes are a factor 20 lower, see figure 4.1 and figure 4.7. This is likely caused due to the relocation of the attachment of the shaker. This location determines the magnitude of the lower frequency response, actuation closer to a nodal point will for example result in a smaller response. This was also noticed during these VAM-experiments, the ‘noise’ was slightly lower than with the previous experiments.

4.2.3 Instantaneous frequency

The instantaneous frequency functions are illustrated in figure 4.10 and these functions fluctuate around the carrier frequency. The nature of the excitation carrier frequencies and their accompanied amplitude and frequency modulation are given in table 4.2.

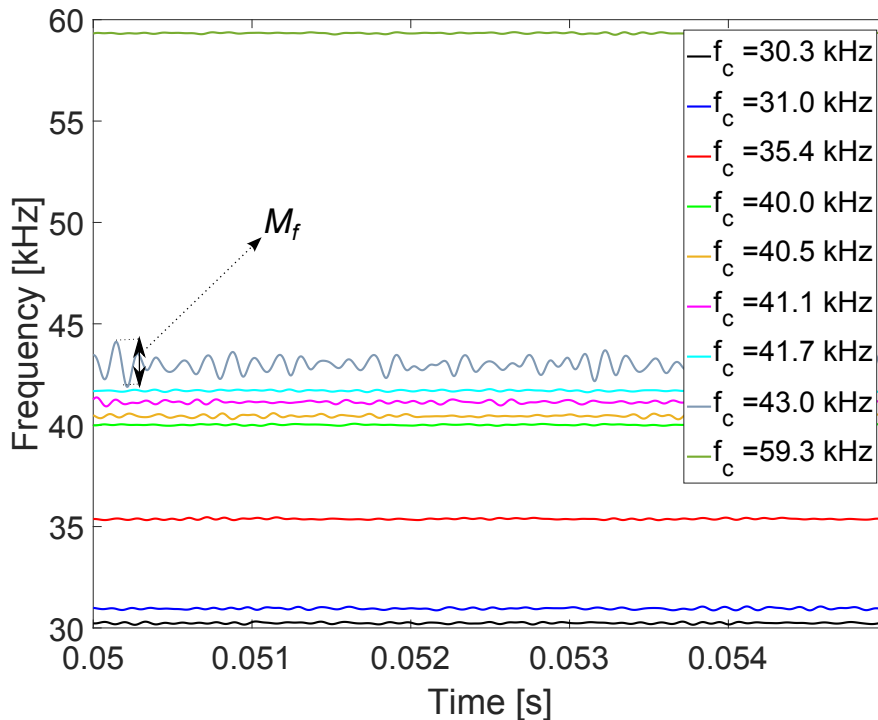


Figure 4.10: Instantaneous frequency for different carrier frequency on the location $(x, y) = (106, 155)$. The excitation parameters $f_p = 633$ Hz, $G_p = 2$ and $F_c = 12$ Volt are kept constant.

As can be seen in figure 4.10, the frequency modulation (peak-to-peak value) is clearly the highest for the carrier frequency of 42.0 kHz. The dominant frequency of the frequency modulation phenomena is again the pump excitation frequency $f_p = 633$ Hz. For the previously considered carrier frequencies of $f_c = 30.3, 31.0, 41.7$ and 43.0 kHz this can be seen respectively in figure 4.11(a), (b), (c) and (d). The ‘strange’ frequencies of 519 Hz and 1007 Hz are again present for the carrier frequency of $f_c = 30.3$ kHz in figure 4.11(a). This is also the case for the carrier frequency of $f_c = 31.0$ kHz where the frequency of 2243 Hz is present next to the expected pump and higher harmonic frequencies, see figure 4.11(b). The frequency content of figure 4.11(a), (b) and (c) shows to consist of more higher harmonics than in the frequency content of the instantaneous amplitude in figure 4.9(a), (b) and (c). The first higher harmonic $2f_p$ has a smaller magnitude in the frequency content of the instantaneous frequency functions and is even not present for the carrier frequency of $f_c = 31.0$ kHz.

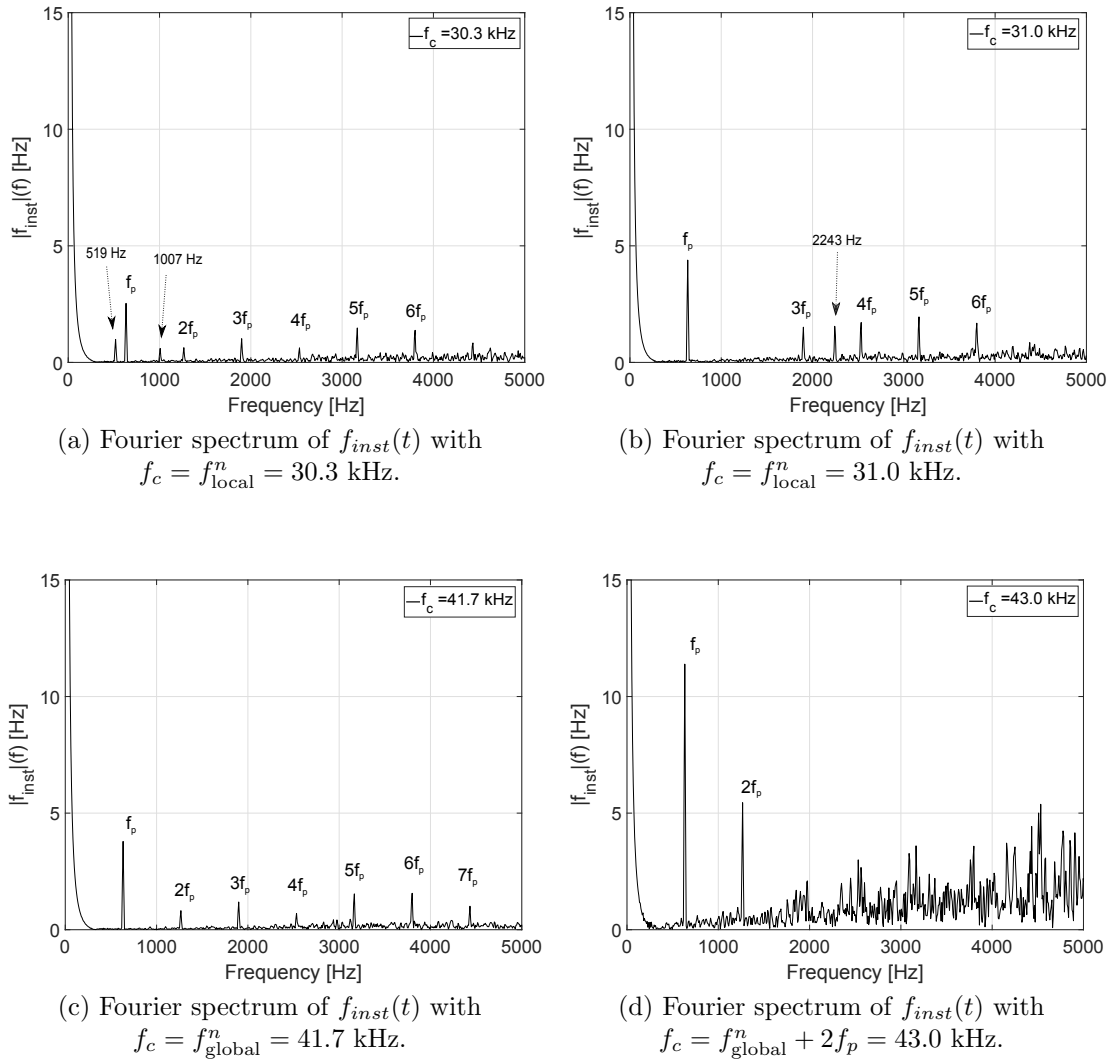


Figure 4.11: $f_{inst}(t)$ for a pump frequency of 633 Hz with a carrier frequency of 30.3 kHz (a), 31.0 kHz (b), 41.7 kHz (c) and 43.0 kHz (d) on location $(x, y) = (106, 155)$. The excitation amplitudes are the same $G_p = 2$ and $F_c = 12$ Volt.

The Fourier spectrum in figure 4.11(d) differs a lot from the other Fourier spectra. A more dominant pump frequency and 1st higher harmonic are present for the carrier excitation of $f_c = 43.0$ kHz. There is however also more ‘noise’ present. The frequency modulation of all the carrier excitation frequencies is listed in table 4.2. The frequencies are listed on descending instantaneous amplitude averages. The very high frequency modulation for the carrier excitation of $f_c = 43.0$ kHz is likely related to the relative low amplitude of the bandpass filtered time response around the carrier frequency. Ooijevaar [3] already stated that poor estimations of the frequency modulation are obtained where the envelope of the response approaches zero. These points are likely to correspond with a nodal point in the ODS of the carrier excitation combined with a relatively large amount of amplitude modulation, almost leading to over-modulation effects which are discussed in section 2.1.1. Even though the envelope does not approach zero, there seems to be a relation in the magnitude of the envelope function and the amount of frequency modulation. This relation is most likely caused by taking the derivative of the experimental data and/or by the dynamic behavior of the specific carrier frequency in that location. It has already been stated that sidebands containing amplitude and frequency modulation do not give a good representation of the severity of the damage [21]. The Fourier spectrum of the instantaneous frequency can be checked to judge the useability of the carrier signal. When the ‘noise’ ratio is relative high, most probably the carrier frequency is not chosen correctly.

4.2.4 Carrier wave selection

The optimal carrier wave selection for damage localization results in a relative high amount of (amplitude) modulation in the damaged area compared to the undamaged area. Ooijevaar [3] concluded for his composite skin-stiffener structure that amplitude modulations can be used for damage localization and that increasing the excitation amplitude of the carrier wave results in overall stronger amplitude modulations. In this thesis the carrier frequency is varied to investigate the resulting signal modulations for a constant carrier excitation amplitude of 12 Volts only in a damaged location. When the carrier frequency is equal to a local or global natural frequency of the structure the amplitude modulations do not seem to depend on the fact whether or not the dynamic behavior is only local or global. However when using a local natural frequency as carrier frequency, the frequency contents of the instantaneous amplitude contains ‘extra’ frequencies next to the expected pump and higher harmonics most likely caused by the clapping behavior. Even though these frequencies cannot be explained, they seem to increase the amount of amplitude modulation. Moreover assuming that those effects do not occur outside the delaminated area and that the structural frequency response of those frequencies is much lower outside the delaminated area, since they are not a local natural frequency over there, would probably result in relative higher amplitude modulations in the delaminated area compared to undamaged areas. This would only hold for choosing a local natural frequency of the delamination as carrier frequency. However for conformation of this conclusion more measuring location inside and outside the damaged area have to be done. Finally it can be concluded that the instantaneous frequency is inconsistent for varying carrier frequencies. It follows from the results that a low structural response of the carrier frequency results in high frequency modulation. This can be explained by the analytical difficulties of determining the instantaneous frequency from the experimental data or by the actual frequency content of the instantaneous frequency for such a carrier frequency. From the results in this thesis it can be concluded that a carrier frequency with a higher structural frequency response is most probably more desirable because either in these frequency ranges the signal modulations are more pure in amplitude or at least the frequency modulation is more ‘trustworthy’, i.e. there is less noise in the frequency content of the instantaneous frequency.

4.3 Higher frequency ranges

The (steady state) VAM-method technique focuses on the frequency response content around the excitation carrier frequency. However certain excitation carrier frequencies modulate the response signal in such a way that frequency content in the Fourier spectrum around two times the carrier frequency is noticed. This could be categorized as the first higher harmonic of the carrier frequency $2f_c$ and is theoretically also shown by Sohn et al [19]. This higher harmonic of the carrier frequency is clearly noticeable for some carrier frequencies, see figure 4.12. Note that also accompanied sidebands of $2f_c \pm nf_p$ (with $n = 1, 2, 3\dots$) can be seen in figure 4.12. Although these components are much weaker in magnitude than the previously discussed sidebands around the carrier frequency, they are again indicative for a nonlinear response. The first eight sidebands are clearly distinguishable from the ‘noise’ level as indicated by the highlighted gray area in figure 4.12. The carrier frequency is equal to a local natural frequency of the structure and has a relative high structural response, see table 4.2.

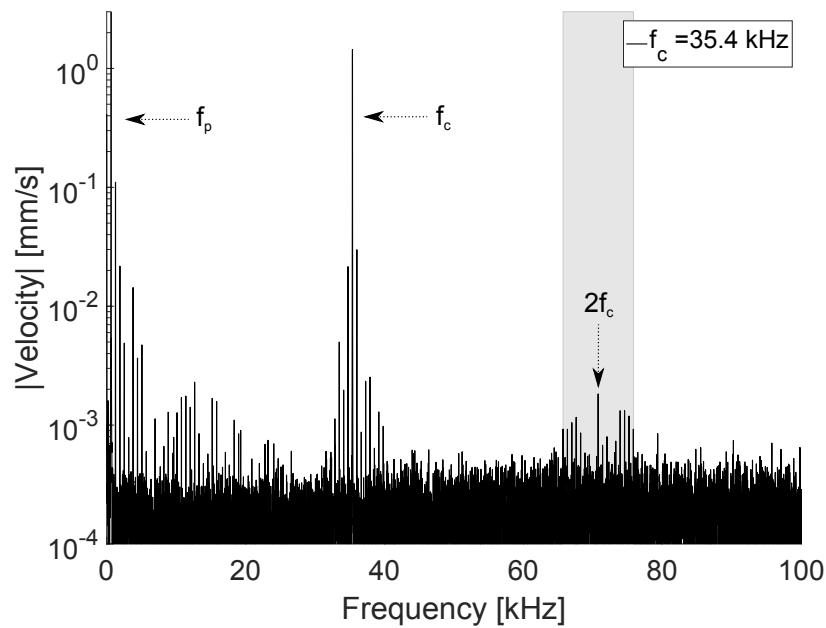


Figure 4.12: The Fourier spectra up to 100 kHz of the velocity responses with $f_p = 633$ Hz and $f_c = 35.4$ kHz on location $(x, y) = (106, 155)$.

This higher harmonic of the carrier frequency and its respective sidebands are only present in the total velocity response signal when the carrier frequency f_c has an absolute velocity response in the Fourier spectrum of at least 1 (mm/s). So the occurrence of a carrier higher harmonic directly depends on whether the carrier frequency is chosen equal to a local or global natural frequency of the structure. The carrier frequencies of 30.3 kHz, 35.4 kHz, 40.0 kHz and 41.7 kHz all show clear sidebands frequencies around $2f_c$. If the magnitude of central carrier frequency in the Fourier spectrum is not that severe, the higher harmonic of the carrier frequency is not that distinguishable anymore from the ‘noise’ level, see figure 4.13. A carrier frequency of 31.0 kHz is used for this VAM-experiment and the highlighted area consist of $2f_c \pm 8f_p$ again.

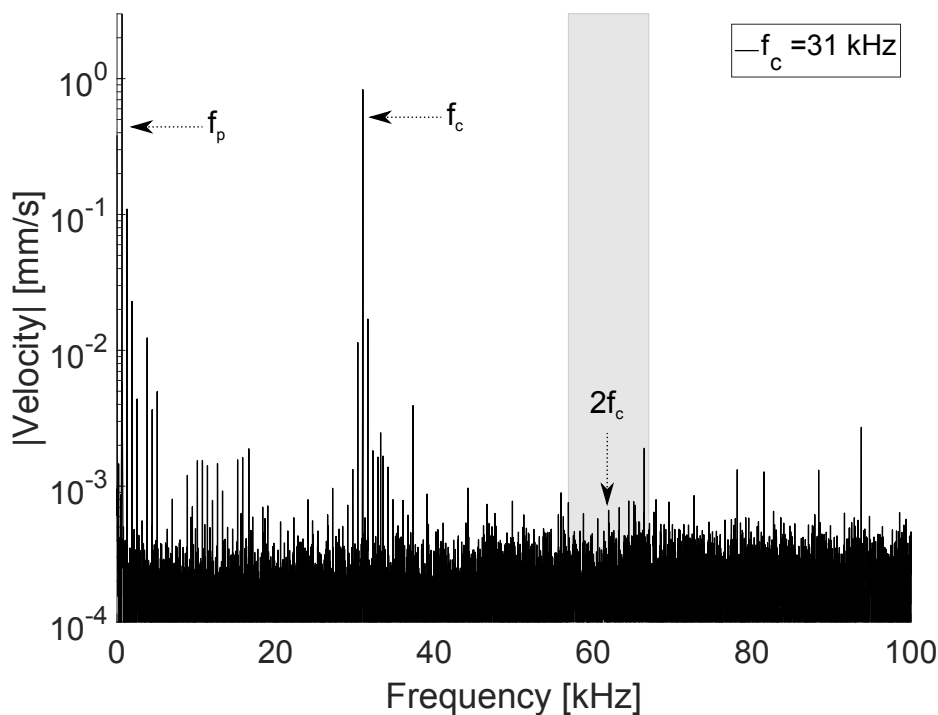


Figure 4.13: The Fourier spectra up to 100 kHz of the velocity responses with $f_p = 633$ Hz and $f_c = 31.0$ kHz on location $(x, y) = (106, 155)$.

4.4 Practical application

The results in this chapter indicate that different pump and carrier excitations result in different acoustic modulations caused by the damaged introduced nonlinearities. The occurring signal modulations in the frequency and time domain are an indication for damage, even though a pristine structure has not been tested in this research. This has already been stated in the literature [3, 19, 29]. The experimental research of these studies [3, 19, 29] and of the current master thesis is however all been done on laboratory controlled test-specimens. Therefore the underlying vibrational characteristics of the damaged test-specimen can be easily determined before performing the actual VAM-experiments. The final goal of VAM is to apply it on practical applications for SHM purposes. It is mostly not practical to determine the natural frequencies and accompanied operational deflection shapes of a structure for a VAM-test at any given time instance. Operational conditions and possible damage scenarios will influence the dynamic characteristics of the structure. Moreover complex shapes of a structure are an obstruction for easily determining those characteristics in the first place. Note that it is even more difficult to determine the local dynamic characteristics of a possible damage scenario since the location, type and severity of the damage are unknown.

In a short amount of time VAM has to interrogate a structure thoroughly to be a robust SHM method. Swept excitations frequencies could therefore help the practical application of VAM. For example when only a fixed excitation frequency is used that has a nodal point in the ODS on the measured damaged location, the signal modulations will be minimal in that location even though there is damaged present. This section discusses a possible application of the considered VAM-method using the obtained results from this master research. A schematic flow chart of this possible application is given in figure 4.14.

Performing a swept pump excitation is not practical. A solution would be to determine the natural frequencies and operational deflection shapes of the pristine structure before it goes into operation. A limited amount of interesting pump frequencies can be selected beforehand based

on sensitive damage locations. When there are possible damages present in the structure, the dynamic behavior is likely to change and the pump frequencies will not coincide perfectly with the actual natural frequencies. It is however assumed that this difference is of minimal influence. In section 2.3 it has already been shown that a frequency deviation is most probably of less importance for the pump excitation.

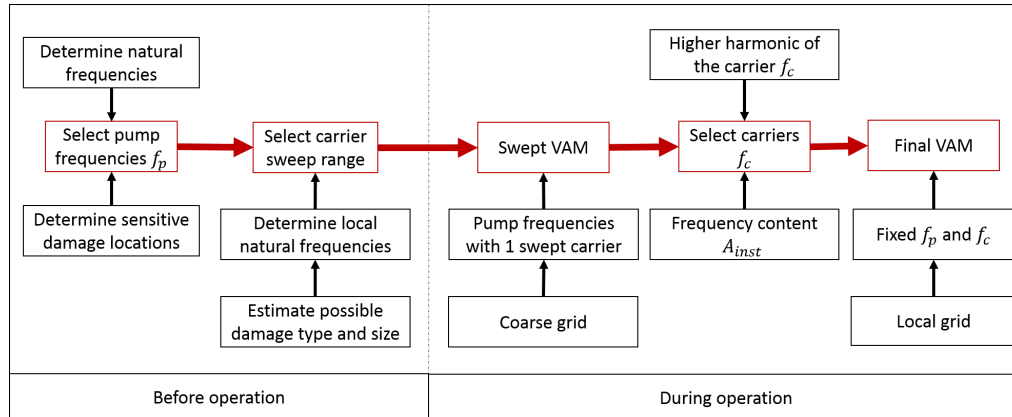


Figure 4.14: A flow chart with the different steps for a possible practical application of VAM, based on the results in this master thesis.

Now that the interesting pump frequencies are selected, the carrier frequencies have to be determined. For the carrier frequency it is interesting to perform a swept excitation on a coarse grid for the previously selected pump frequencies, as will be made clear in the remainder of this section. The excitation frequency window is still an unknown that can be estimated by (numerically) calculating the local natural frequencies of the most likely occurring damages scenarios. When performing a swept carrier excitation, the sidebands in traditional frequency domain analysis cannot be used anymore for damage identification since the sidebands will be overshadowed by the excitation frequency range. A possible solution is to use a short-time Fourier transform to transform the response into the time-frequency domain. The first higher harmonic of the excitation carrier frequency and its sidebands, discussed in section 4.3, can be used as an indicator for damage detection. These specific carrier frequencies with a lot of signal modulations can be selected for a final VAM test. A possible local natural frequency is excited when the unexplained 'extra' frequencies are present between the sidebands around the carrier frequency.

A different approach that still uses the specific pristine pump excitations, can be to extract the signal modulation in the time domain using the Hilbert transform. The frequency content of the instantaneous amplitude can be extracted using the short-time Fourier transform. Modulation can then be detected through the presence of energy at specific frequencies as can already been seen in figure 4.9. These frequencies mostly correspond with the (suitable) pump frequency and its higher harmonics. A possible local natural frequency is excited when there are 'extra' frequencies present in the Fourier spectrum.

The ability of determining which frequencies correspond to high modulation levels on specific coarse grid points can be used for damage identification on the adjacent local area. When good combinations of a pump and a carrier frequency are selected these can be used on a finer grid to localize damage. Especially, local natural frequencies as carrier would help to map the location of the damage with the obtained amplitude modulations as seen in figure 2.3

This section has proposed a practical application for the VAM-method. Even though there are still a lot of unknowns, some steps towards a more practical application have been taken. More research is however still needed and the proposed method in this section should first be tested. Note that measuring the responses in a practical application is also still a challenging point of attention.

Chapter 5

Conclusions and recommendations

The objective of this research was to analyze whether the excitations of the steady state vibro-acoustic modulation method can be optimized to increase the damage identification capabilities. This is done by getting more insight on the modulation phenomena. Steady state VAM-experiments were performed by simultaneously applying a low-frequency pump signal and a higher frequency carrier signal. These frequencies were varied together with the pump excitation force. The Fourier spectra of the total and bandpass velocity response were extracted to analyze the magnitude response of the frequency content. This narrow-band velocity response around the carrier frequency is used to extract the instantaneous amplitude and frequency.

5.1 Conclusions

The answers to the research questions from section 1.4 are answered in this chapter. The conclusions are based on the results obtained in this master thesis on the composite plate structure with an artificial circular delamination. Note that the measuring location was fixed on a single point due to problems with the experimental setup, such that not all research questions could be answered completely.

- The number and magnitude of higher harmonics and sidebands are dependent on the underlying structural response of the structure for the pump and carrier frequency. The ODS and excitation amplitude of the pump wave also affect the signal modulations. When the carrier frequency is equal to a certain local natural frequency of the delamination, unexpected frequencies are present in the narrow band frequency content. See section 4.1 and 4.2.
- The instantaneous amplitude and frequency are dependent on the selection of the carrier excitation frequency and the introduced sidebands. The excitation carrier frequency determines the average magnitude of the instantaneous amplitude by the underlying structural response of this frequency, however this relation is not consistent. The amplitude modulation is also not directly dependent on this average magnitude of the instantaneous amplitude. The frequency content of the instantaneous amplitude consisting of the pump frequency and its higher harmonics increases in magnitude for using a natural frequency. The extra frequencies present in the Fourier spectrum most possibly result in more amplitude modulation for specific local natural frequencies. See section 4.2.
- A relation between the amount of frequency modulation and the carrier frequency is not found on the current structure. Relative high amounts of frequency modulation are acquired for a carrier frequency that results in a small envelope of the bandpass filtered response. Poor estimations of the frequency modulation indicate that it is not as suitable

as amplitude modulation for damage identification. Similar conclusions have also been made by Ooijevaar [3].

- The magnitude of the frequency and amplitude modulations cannot be compared directly to Ooijevaar [3]. However the results from this study indicate that using a local natural frequency as carrier enhances the localization capabilities of VAM. A practical application has been proposed in section 4.4.

Finally, the main research question from section 1.4 is repeated and answered accordingly:

How can an optimal selection of the pump and carrier frequency be achieved for efficient damage identification using VAM and can the obtained modulations be understood?

The optimal pump excitation is equal to a global natural frequency with sufficient elastic displacement that causes the opening and closing behavior of the delamination. The accompanied carrier frequency has to coincide with a local natural frequency of the delamination, such that the amplitude modulations in the damaged area will increase more than in the undamaged area. This can be used for a more efficient damage identification and the present thesis proposes a practical application, see section 4.4. The frequency modulation is inconsistent, i.e. it has no relation with the damage and/or it cannot be flawlessly calculated from the experimental data. Most obtained signal modulations in the frequency domain can be related to the underlying frequency response of the considered structure but are also dependent on the carrier frequency.

5.2 Recommendations

The current study shows the importance of separating the local dynamic behavior of the delamination and the global dynamic behavior of the structure. However due to limitations on the experimental equipment this could not be fully exploited. The following recommendations should therefore be considered:

- The attachment of the shaker should be fixed to one location of the structure. Also the attachment of the piezoelectric transducer should be investigated more thoroughly.
- A new cable will result in higher resolution measurements and will enable the ability for a larger measurement grid. Such a larger grid results in the better separation of the local dynamic effects from the global dynamic characteristics.
- In-cooperate the control of the shaker in the Matlab scripts. The results can then also be investigated on phase differences.
- The location and the severity of the damage should be checked, even though a damage has to be present that causes the nonlinearities.
- A data acquisition upgrade: the current sample rate is sufficient however the data storage is limited with ‘only’ 128 000 samples.

For following research the following recommendations should be considered:

- Measuring the VAM-response on more locations such that damage localization can be realized. The relative signal modulations between the damaged and undamaged area are interesting for varying carrier frequencies.
- Experimentally investigating the influence of choosing the excitation frequency with a specific offset of a natural frequency. It has been concluded that the carrier frequency should be closer to a natural frequency than the pump frequency, see section 2.3.
- Executing and analyzing the capabilities of the considered practical application from section 4.4.
- More research is needed on the understanding of the ‘extra’ frequency content in the narrowband frequency spectra for some local natural frequencies as carrier. (Section 4.2.1).

Bibliography

- [1] C. Boller, “Structural health monitoring an introduction and definitions”, in *Encyclopedia of Structural Health Monitoring*, 2009, ch. 1, pp. 1–23.
- [2] S. Yashiro, K. Ogi, A. Yoshimura, and Y. Sakaida, “Characterization of high-velocity impact damage in cfrp laminates : part ii prediction by smoothed particle hydrodynamics”, *Composites Part A*, vol. 56, pp. 308–318, 2014.
- [3] T. H. Ooijevaar, “Vibration based structural health monitoring of composite skin-stiffener structures”, PhD thesis, University of Twente, Enschede, 2014.
- [4] H. Kim, J. C. Halpin, and G. K. DeFrancisci, “Impact damage of composite structures”, in *Long-Term Durability of Polymeric Matrix Composites*, 2012, pp. 143–180.
- [5] J. Baaran, “Visual inspection of composite structures”, European Aviation Safety Agency (EASA), Tech. Rep., 2009.
- [6] S. Dowling, “What caused the space shuttle columbia disaster?”, *BBC*, 2015.
- [7] K. V. Jata, A. Roy, and T. A. Parthasarathy, “Chapter 10 failure modes of aerospace materials”, *Encyclopedia of Structural Health Monitoring*, pp. 1–18,
- [8] L. Pieczonka, A. Martowicz, and W. Staszewski, “Nonlinear vibroacoustic wave modulations for structural damage detection : an overview”, *Optical engineering*, vol. 55, 1 2016.
- [9] D. Garcia, R. Palazzetti, I. Trendafilova, C. Fiorini, and A. Zucchelli, “Vibration-based delamination diagnosis and modelling for composite laminate plates”, *Composite Structures*, vol. 130, pp. 155–162, 2015.
- [10] N. A. Chrysochoidis, A. K. Barouni, and D. A. Saravanos, “Delamination detection in composites using wave modulation spectroscopy with a novel active nonlinear acousto-ultrasonic piezoelectric sensor”, *Journal of Intelligent Material Systems and Structures*, vol. 22, no. 18, pp. 2193–2206, 2011.
- [11] N. A. Chrysochoidis, T. T. Assimakopoulou, and D. A. Saravanos, “Nonlinear wave structural health monitoring method using an active nonlinear piezoceramic sensor for matrix cracking detection in composites”, *Journal of Intelligent Material Systems and Structures*, vol. 26, no. 15, pp. 2108–2120, 2014.
- [12] F. Aymerich and W. Staszewski, “Impact damage detection in composite laminates using nonlinear acoustics”, *Composites Part A: Applied Science and Manufacturing*, vol. 41, no. 9, pp. 1084–1092, 2010.
- [13] W. Fan and P. Qiao, “Vibration-based damage identification methods : a review and comparative study”, *Structural Health Monitoring*, vol. 10, no. 1, pp. 83–111, 2011.
- [14] K. Worden and M. I. Friswell, “Modal vibration-based damage identification”, in *Encyclopedia of Structural Health Monitoring*, 2009, pp. 1–37.
- [15] D. M. Donskoy, “Nonlinear acoustic methods”, in *Encyclopedia of Structural Health Monitoring*, vol. 1, 2009, pp. 1–12.
- [16] K. Worden, C. Farrar, J. Haywood, and M. Todd, “A review of nonlinear dynamics applications to structural health monitoring”, *Structural Control and Health Monitoring*, vol. 15, pp. 540–567, 2007.

- [17] A. Klepka, M. Strczkiewicz, L. Pieczonka, W. J. Staszewski, L. Gelman, F. Aymerich, and T. Uhl, "Triple correlation for detection of damage-related nonlinearities in composite structures", *Nonlinear Dynamics*, pp. 453–468, 2015.
- [18] K. Zacharias, E. Balabanidou, I. Hatzokos, I. T. Rekanos, and A. Trochidis, "Microdamage evaluation in human trabecular bone based on nonlinear ultrasound vibro-modulation (nuvm).", *Journal of biomechanics*, vol. 42, no. 5, pp. 581–586, 2009.
- [19] H. Sohn, H. J. Lim, M. P. Desimio, K. Brown, and M. Derriso, "Nonlinear ultrasonic wave modulation for online fatigue crack detection", *Journal of Sound and Vibration*, vol. 333, no. 5, pp. 1473–1484, 2014.
- [20] M. Venterink, "Literature study on the vibro-acoustic modulation method(s)", University of Twente, Department of Applied Mechanics (AM), Tech. Rep., Sep. 2016.
- [21] H. F. Hu, W. J. Staszewski, N. Q. Hu, R. B. Jenal, and G. J. Qin, "Crack detection using nonlinear acoustics and piezoceramic transducers instantaneous amplitude and frequency analysis", *Smart Materials and Structures*, vol. 19, no. 6, 2010.
- [22] T. Trojnar, A. Klepka, L. Pieczonka, and W. J. Staszewski, "Fatigue crack detection using nonlinear vibro-acoustic cross-modulations based on the luxemburg-gorky effect", *Health Monitoring of Structural and Biological Systems*, vol. 9064, 2014.
- [23] K. Y. Jhang, "Nonlinear ultrasonic techniques for non-destructive assessment of micro damage in material : a review", *International Journal of Precision Engineering and Manufacturing*, vol. 10, no. 1, pp. 123–135, 2009.
- [24] D. Broda, W. Staszewski, A. Martowicz, T. Uhl, and V. Silberschmidt, "Modelling of nonlinear crackwave interactions for damage detection based on ultrasound a review", *Journal of Sound and Vibration*, vol. 333, no. 4, pp. 1097–1118, 2014.
- [25] I. Solodov, D. Döring, and G. Busse, "New opportunities for ndt using non-linear interaction of elastic waves with defects", *The 10th International Conference of the Slovenian Society for Non-Destructive Testing*, pp. 1–16, 2009.
- [26] C. Pecorari and I. Solodov, "Nonclassical nonlinear dynamics of solid surfaces in partial contact for nde applications", in *Universality of Nonclassical Nonlinearity*, 2006, pp. 309–326.
- [27] A. Klepka, W. Staszewski, R. Jenal, M. Szewdo, J. Iwaniec, and T. Uhl, "Nonlinear acoustics for fatigue crack detection - experimental investigations of vibro-acoustic wave modulations", *Structural Health Monitoring*, vol. 11, no. 2, pp. 197–211, 2012.
- [28] M. Meo and G. Zumpano, "Nonlinear elastic wave spectroscopy identification of impact damage on a sandwich plate", *Composite Structures*, vol. 71, pp. 469–474, 2005.
- [29] N. C. Yoder and D. E. Adams, "Vibro-acoustic modulation utilizing a swept probing signal for robust crack detection", *Structural Health Monitoring*, vol. 9, no. 3, pp. 257–267, 2010.
- [30] A. W. Leissa, "Vibration of plates", *NASA office of technology utilization*, no. NASA-SP-160, p. 101, 1969.
- [31] C. N. Della, D. W. Shu, and C. N. Della, "Vibration of delaminated composite laminates : vibration of delaminated composite laminates : a review", *Applied Mechanics reviews, ASME*, vol. 60, no. Jan. 2007, 2007.
- [32] I. Senjanović, N. Hadžić, N. Vladimir, and D. Cho, "Natural vibrations of thick circular plate based on the modified mindlin theory", *Arch. Mech.*, vol. 66, no. 6, pp. 389–409, 2014.
- [33] M. A. Okeson, K. G. Kellogg, and A. R. Kallmeyer, "Impact damage growth in fiber-glass/epoxy laminates subjected to moisture and low temperature thermal cycling", *International Journal of Offshore and Polar Engineering*, pp. 1–8, 2006.
- [34] *Duraact patch transducer*, P-876.SP1, PI Ceramic, Feb. 2015.
- [35] I. Mueller, A. Shpak, M. V. Golub, and C.-P. Fritzen, "Effects of debonding of pw as on the wave propagation and the electro-mechanical impedance spectrum", *EWSHM 2016*, vol. 8, no. July, pp. 5–8, 2016.

-
- [36] I. Bueche and C.-P. Fritzen, “Investigation on sensor fault effects of piezoelectric transducers on wave propagation and impedance measurements”, *Proceedings of the 2013 COMSOL Conference*, 2013.
- [37] I. Bueche, B. Eckstein, and C.-p. Fritzen, “Model-based detection of sensor faults under changing temperature conditions”, *Structural Health Monitoring*, vol. 13(2), pp. 109–119, 2014.
- [38] T. G. Overly, G. Park, K. M. Farinholt, and C. R. Farrar, “Piezoelectric active-sensor diagnostics and validation using instantaneous baseline data”, *Structural Health Monitoring*, vol. 9, no. 11, pp. 1414–1421, 2009.
- [39] A. N. R. G. Park, Charles R. Farrar, Amanda C. Rutherford, “Piezo-sensor self-diagnostics using electrical impedance measurements”, *Adaptive Structures and Technologies*, 2004.
- [40] *Strain gage adhesive*, M-Bond 200, Micro Measurements, a VPG brand, Jul. 2014.
- [41] *Epoxy adhesive*, EA 9466, Loctite, Sep. 2014.
- [42] T. Wandowski, J. Moll, P. Malinowski, S. Opoka, and W. Ostachowicz, “Assessment of piezoelectric sensor adhesive bonding”, *Journal of Physics*, vol. 628, 2015.

Appendix A

Frequency modulation

This appendix holds the derivation of a frequency modulated signal with the Single-tone Modulation method. Frequency modulation (FM) is a specific case of phase modulation (PM). The input carrier signal can be expressed as:

$$q(t) = A_c \cos(\omega_c t + \phi_c) \quad (\text{A.1})$$

An angle modulated signal can be represented as:

$$q(t) = A_c \cos(\omega_c t + \theta(t) + \phi_c) \quad (\text{A.2})$$

in which $\phi(t) = \omega_c t + \theta(t) + \phi_c$ is the instantaneous phase. The function $\theta(t)$ is the phase modulation signal. The instantaneous angular frequency of the modulated signal is defined as:

$$\omega(t) = \frac{d}{dt}[\omega_c t + \theta(t) + \phi_c] = \omega_c + \frac{d(\theta(t))}{dt} \quad (\text{A.3})$$

in which $\frac{d(\theta(t))}{dt}$ is the instantaneous frequency. The instantaneous phase of the carrier $\phi(t)$ is related to the frequency modulating signal m_f . Depending on the the relationship between $\phi(t)$ and m_f , different forms of angle modulation can exist. The frequency deviation of the carrier signal caused by the modulation signal m_f , can be expressed as:

$$\frac{d(\theta(t))}{dt} = k_f m_f(t) \quad (\text{A.4})$$

where k_f is a frequency deviation constant. This total expression for the instantaneous phase can be expressed as:

$$\phi(t) = k_f \int_0^t (m_f(\tau) d\tau) + \omega_c t + \phi_c \quad (\text{A.5})$$

When $m_f(t)$ is considered to be a sinusoidal, the instantaneous frequency deviation of the angle-modulated signal is sinusoidal. This is named the Single-tone Modulation method and the response spectrum can be analytically obtained for this case.

$$m_f(t) = A_p \cos \omega_p t + \phi_p \quad (\text{A.6})$$

$$\int_0^t m_f(\tau) d\tau = \frac{A_p}{2\pi f_p} \cos(2\pi f_p t + \phi_p) = \frac{A_p}{\omega_p} \cos(\omega_p t + \phi_p) \quad (\text{A.7})$$

The instantaneous phase deviation of the modulated signal will result in:

$$\phi(t) = \frac{k_f A_p}{\omega_p} \sin(\omega_p t + \phi_p) + \omega_c t + \phi_c \quad (\text{A.8})$$

The instantaneous frequency can be calculated as:

$$f(t) = \frac{1}{2\pi} \frac{d\phi(t)}{dt} \quad (\text{A.9})$$

The total response of the modulated signal can be expressed as:

$$q(t) = A_c \cos(\omega_c t + \frac{k_f A_p}{\omega_p} \cos(\omega_p t + \phi_p) + \phi_c) \quad (\text{A.10})$$

The frequency modulation index is defined as:

$$\beta_{FM} = \frac{k_f A_p}{\omega_p} = \frac{f_\Delta |m_f(t)|}{f_{max}} \quad (\text{A.11})$$

in which $k_f A_p$ is the maximum frequency deviation of the instantaneous frequency from the carrier frequency f_c and ω_p is the largest frequency f_m present in the modulation signal $m_f(t)$, which is used as scaling.

Equation (A.10) results in a total response signal of:

$$q(t) = A_c \cos(\omega_c t + \phi_c) \cos(\beta_{FM} \sin \omega_p t + \phi_p) - A_c \sin(\omega_c t + \phi_c) \sin(\beta_{FM} \cos \omega_p t + \phi_p) \quad (\text{A.12})$$

When the parameter β_{FM} is assumed to be very small, a narrow band approach around the carrier frequency can be used and the equation for the modulated signal reduces to:

$$q(t) = A_c \cos(\omega_c t + \phi_c) - A_c \beta_{FM} \sin(\omega_c t + \phi_c) \cos(\omega_p t + \phi_p) \quad (\text{A.13})$$

And this again can be rewritten with trigonometry in the original signal with 2 different sideband frequencies:

$$q(t) = A_c \cos(\omega_c t) - \frac{k_f A_c A_p}{2\omega_p} [\sin((\omega_c - \omega_p)t + \phi_c - \phi_p) + \sin((\omega_c + \omega_p)t + \phi_c + \phi_p)] \quad (\text{A.14})$$

Appendix B

Perturbation Technique

A generalized quasi-harmonic nonlinear multi-DOF system can be described by a differential equation [3]. The first part contains linear terms and the second part contains nonlinear terms:

$$\ddot{\mathbf{q}} + \omega_{n,0}^2 \mathbf{q} = -\epsilon f(\mathbf{q}, \dot{\mathbf{q}}), \quad (\text{B.1})$$

in which $\ddot{\mathbf{q}}$, $\dot{\mathbf{q}}$ and \mathbf{q} are the acceleration, velocity and displacement vectors. Note that the eigenfrequency ω_0 is a scalar. There are however multiple solutions for the eigenvalue problem; the number of eigenfrequencies n corresponds to the number of independent equations of the system n . The nonlinear function $f([\mathbf{q}], [\dot{\mathbf{q}}])$ is controlled by the parameter ϵ . For a weak nonlinear system, the parameter ϵ is relative small and the total solution of the system can be approximated by using a perturbation technique based on a power series:

$$\mathbf{q}(t) = \mathbf{q}_0(t) + \epsilon \mathbf{q}_1(t) + \epsilon^2 \mathbf{q}_2(t) + \dots \quad (\text{B.2})$$

In this appendix an undamped system containing a quadratic velocity nonlinearity is considered with two tones forced excitation. The steady state response will be expressed of this system to illustrate the modulation effects. This quadratic velocity nonlinearity system is expressed as:

$$\ddot{\mathbf{q}} + \omega_{n,0}^2 \mathbf{q} = -\epsilon \dot{\mathbf{q}}^2 + F_p \cos(\omega_p t + \phi_p) + F_c \cos(\omega_c t + \phi_c), \quad (\text{B.3})$$

where F_p and F_c are the amplitudes, ω_p and ω_c ($\omega_p \ll \omega_c$) the angular frequencies and ϕ the phases.

Separating the different orders of magnitude from this total solution in equation (B.2), results in expressions for every order:

$$O(\epsilon^0) : \quad \ddot{\mathbf{q}}_0 + \omega_{n,0}^2 \mathbf{q}_0 = F_p \cos(\omega_p t + \phi_p) + F_c \cos(\omega_c t + \phi_c) \quad (\text{B.4})$$

$$O(\epsilon^1) : \quad \ddot{\mathbf{q}}_1 + \omega_{n,0}^2 \mathbf{q}_1 = -\dot{\mathbf{q}}_0^2 \quad (\text{B.5})$$

$$O(\epsilon^2) : \quad \ddot{\mathbf{q}}_2 + \omega_{n,0}^2 \mathbf{q}_2 = -2\dot{\mathbf{q}}_0 \dot{\mathbf{q}}_1 \quad (\text{B.6})$$

$$O(\epsilon^3) : \quad \ddot{\mathbf{q}}_3 + \omega_{n,0}^2 \mathbf{q}_3 = -\dot{\mathbf{q}}_1^2 - 2\dot{\mathbf{q}}_0 \dot{\mathbf{q}}_2 \quad (\text{B.7})$$

$$\dots : \quad \dots = \dots \quad (\text{B.8})$$

$$(\text{B.9})$$

The solution of equation (B.5) will be:

$$\mathbf{q}_0(t) = \frac{F_p}{\omega_{n,0}^2 - \omega_p^2} \cos(\omega_p t + \phi_p) + \frac{F_c}{\omega_{n,0}^2 - \omega_c^2} \cos(\omega_c t + \phi_c) \quad (\text{B.10})$$

The derivative can expressed as:

$$\dot{\mathbf{q}}_0(t) = -\frac{\omega_p F_p}{\omega_{n,0}^2 - \omega_p^2} \sin(\omega_p t + \phi_p) - \frac{\omega_c F_c}{\omega_{n,0}^2 - \omega_c^2} \sin(\omega_c t + \phi_c) \quad (\text{B.11})$$

The equation (B.11) can be used to express the right hand-side of equation (B.5) as following:

$$\begin{aligned}
-\mathbf{q}_0^2 &= \frac{\omega_p^2 F_p^2}{2(\omega_{n,0}^2 - \omega_p^2)^2} \cos(2\omega_p t + 2\phi_p) + \frac{\omega_c^2 F_c^2}{2(\omega_{n,0}^2 - \omega_c^2)^2} \cos(2\omega_c t + 2\phi_c) \\
&+ \frac{\omega_p \omega_c F_p F_c}{(\omega_{n,0}^2 - \omega_p^2)(\omega_{n,0}^2 - \omega_c^2)} \cos((\omega_c + \omega_p)t + \phi_c + \phi_p) - \frac{F_p^2 \omega_p^2}{2(\omega_{n,0}^2 - \omega_p^2)^2} \\
&- \frac{\omega_p \omega_c F_p F_c}{(\omega_{n,0}^2 - \omega_p^2)(\omega_{n,0}^2 - \omega_c^2)} \cos((\omega_c - \omega_p)t + \phi_c - \phi_p) - \frac{F_c^2 \omega_c^2}{2(\omega_{n,0}^2 - \omega_c^2)^2}
\end{aligned} \tag{B.12}$$

The following expressions are used for simplifications:

$$A_{p,n} = \frac{F_p}{\omega_{n,0}^2 - \omega_p^2} \quad A_{c,n} = \frac{F_c}{\omega_{n,0}^2 - \omega_c^2} \tag{B.13}$$

Substituting in equation (B.2) and rearranging gives:

$$\begin{aligned}
\ddot{\mathbf{q}}_1 + \omega_{n,0}^2 \mathbf{q}_1 &= -\frac{\omega_p^2 A_{p,n}^2}{2} - \frac{\omega_c^2 A_{c,n}^2}{2} \\
&+ \frac{A_{p,n}^2 \omega_p^2}{2} \cos(2\omega_p t + 2\phi_p) + \frac{A_{c,n}^2 \omega_c^2}{2} \cos(2\omega_c t + 2\phi_c) \\
&- A_{p,n} A_{c,n} \omega_p \omega_c \cos((\omega_c - \omega_p)t + \phi_c - \phi_p) + A_{p,n} A_{c,n} \omega_p \omega_c \cos((\omega_c + \omega_p)t + \phi_c + \phi_p),
\end{aligned} \tag{B.14}$$

The response $\mathbf{q}_1(t)$ of equation (B.14) will again be linear combination of harmonic components with frequencies equal to: $2\omega_p, 2\omega_c, \omega_c - \omega_p, \omega_c + \omega_p$ and a constant term. The response in equation B.10 and that of $\mathbf{q}_1(t)$ have to be combined in equation (B.2), to obtain the first order nonlinear solution of equation (B.3).

$$\begin{aligned}
\mathbf{q}_{\text{total}}(t) &= A_{p,n} \cos(\omega_p t + \phi_p) + A_{c,n} \cos(\omega_c t + \phi_c) - \frac{\epsilon}{2\omega_{n,0}^2} (A_{p,n}^2 \omega_p^2 + A_{c,n}^2 \omega_c^2) \\
&- \frac{\epsilon}{2(\omega_{n,0}^2 - 4\omega_p^2)} A_{p,n}^2 \omega_p^2 \cos(2\omega_p t + 2\phi_p) - \frac{\epsilon}{2(\omega_{n,0}^2 - 4\omega_c^2)} A_{c,n}^2 \omega_c^2 \cos(2\omega_c t + 2\phi_c) \\
&+ A_{sb1,n} \omega_p \omega_c \cos((\omega_c - \omega_p)t + \phi_c - \phi_p) + A_{sb2,n} \omega_p \omega_c \cos((\omega_c + \omega_p)t + \phi_c + \phi_p),
\end{aligned} \tag{B.15}$$

in which:

$$A_{sb1,n} = \frac{-\epsilon A_{p,n} A_{c,n}}{\omega_{n,0}^2 - (\omega_c - \omega_p)^2} \quad A_{sb2,n} = \frac{-\epsilon A_{p,n} A_{c,n}}{\omega_{n,0}^2 - (\omega_c + \omega_p)^2}. \tag{B.16}$$

When only a narrow band response around the carrier frequency is considered, this can be expressed as:

$$\begin{aligned}
\mathbf{q}_{\text{bp}}(t) &= A_{c,n} \cos(\omega_c t + \phi_c) + A_{sb1,n} \omega_p \omega_c \cos((\omega_c - \omega_p)t + \phi_c - \phi_p) \\
&+ A_{sb2,n} \omega_p \omega_c \cos((\omega_c + \omega_p)t + \phi_c + \phi_p),
\end{aligned} \tag{B.17}$$

When the present multi-DOF system is summed to obtain the total narrow band response, it results in:

$$\begin{aligned}
q_{\text{totalbp}}(t) &= \sum_{k=1}^n (A_{c,n} \cos(\omega_c t + \phi_c) + A_{sb1,n} \omega_p \omega_c \cos((\omega_c - \omega_p)t + \phi_c - \phi_p) \\
&+ A_{sb2,n} \omega_p \omega_c \cos((\omega_c + \omega_p)t + \phi_c + \phi_p)),
\end{aligned} \tag{B.18}$$

where $k = 1, 2, 3, \dots, n$ are the degrees of freedom with n the total amount of DOF's. When it is assumed that the terms with a certain frequency (ω_p, ω_c and the sidebands ($\omega_c \pm \omega_p$)) will only

contribute to the total response when their frequency corresponds with a eigenfrequency of the structure ($\omega_{p,0}, \omega_{c,0}$ and the sidebands ($\omega_{(c\pm p),0}$), the total narrow-band response will become:

$$q_{totalbp}(t) = A'_c \cos(\omega_c t + \phi_c) + A'_{sb1} \omega_p \omega_c \cos((\omega_c - \omega_p)t + \phi_c - \phi_p) + A'_{sb2} \omega_p \omega_c \cos((\omega_c + \omega_p)t + \phi_c + \phi_p) \quad (\text{B.19})$$

in which:

$$A'_{sb1} = \frac{-\epsilon A'_p A'_c}{\omega_{(c-p),0}^2 - (\omega_c - \omega_p)^2}, \quad A'_c = \frac{F_c}{\omega_{c,0}^2 - \omega_c^2},$$

$$A'_{sb2} = \frac{-\epsilon A'_p A'_c}{\omega_{(c+p),0}^2 - (\omega_c + \omega_p)^2}, \quad A'_p = \frac{F_p}{\omega_{p,0}^2 - \omega_p^2}.$$

Appendix C

Hilbert Transform

The Hilbert Transform is a often used tool to obtain the instantaneous modulation characteristics. For any narrow-band signal $q(t)$, the HT can be defined as:

$$H[q(t)] = \hat{q}(t) = \frac{1}{\pi} P \int_{-\infty}^{+\infty} \frac{x(\tau)}{t - \tau} d\tau \quad (\text{C.1})$$

where P is the Cauchy principal value. The original signal $q(t)$ and the HT $\hat{q}(t)$ can be used to obtain the analytical signal defined as:

$$z(t) = q(t) + i\hat{q}(t) = A_{inst}(t)e^{i\phi(t)} \quad (\text{C.2})$$

where $A_{inst}(t)$ and $\phi(t)$ are respectively the envelope and the instantaneous phase given as:

$$A_{inst}(t) = \sqrt{q^2(t) + \hat{q}^2(t)} \quad (\text{C.3})$$

$$\phi_{inst}(t) = \arctan \frac{\hat{q}(t)}{q(t)} \quad (\text{C.4})$$

The envelope function is a smooth curve which joins local maxima of the original signal. The amplitude modulation signal in amplitude modulation is represented by this curve. The calculation process used to obtain the instantaneous frequency often uses the Fourier transform Ψ (FT) to obtain the HT. The instantaneous phase from equation C.4 can be expressed as:

$$\phi_{inst}(t) = \Psi \ln(z(t)) \quad (\text{C.5})$$

The instantaneous frequency, representing the frequency modulation signal in angular frequency, can be obtained using equation (A.9):

$$\omega_{inst}(t) = \frac{d\phi_{inst}(t)}{dt} = \Psi \frac{d}{dt} \ln(z(t)) = \Psi \frac{1}{z} \frac{dz(t)}{dt} \quad (\text{C.6})$$

Appendix D

Hilbert-Huang Transform

The HTT is a time-frequency empirical analysis method suitable for non-linear and non-stationary signal processing. This transform method is not restricted to a narrow-band signal and the signal can be both amplitude- and frequency modulated. Two different procedures are used, the empirical mode decomposition (EMD) and the HT. The EMD is used to decompose the signal into several intrinsic mode functions (IMFs). The procedure is explained in detail in [21]. After the different IMFs are created, the HT is used on these IMFs to get the instantaneous frequencies and amplitudes for the mono-component signals.

The original signal can be represented with the HTT as:

$$q(t) = \sum_{i=1}^n c_i + r_n \quad (\text{D.1})$$

The IMFs c_1, c_2, \dots, c_n include the different frequency bands from high to low. The frequency components present in each frequency band are different and will not overlap each other. The composition of each frequency band will change when the signal $x(t)$ changes. The component r_n represents the central characteristics of the original signal $x(t)$. The instantaneous frequency and amplitude functions for each frequency band can be obtained from equation D.1 with the HT as discussed in section C.

Appendix E

Eigenfrequencies of a circular plate

This appendix lists the eigenfrequencies of two different sized circular plates with a clamped and a simply supported boundary condition. The diameters of the composite thermoplastic PEKK/AS4D circular plates are 50 mm and 100 mm for respectively the fabricated plate 1 and plate 2 and have a thickness of 0.26 mm with a [0,90] lay-up. The eigenfrequencies of plate 1 are given in table E.1 and the eigenfrequencies of plate 2 are given in table E.2.

Table E.1: Eigenfrequencies for 2 clamped circular plates with a diameter of 50 mm (plate 1) and 100 mm (plate 2) and thickness of 0.26 mm. The mode i refers to the number of circular nodes j of the circular plate and the number of nodal diameters k .

Eigenfrequencies		[kHz]	[kHz]	[kHz]	[kHz]
Mode $i (j, k)$		1	2	3	4
1	Plate 1	11.8	24.4	40.2	58.8
	Plate 2	2.9	6.1	10.0	14.7
2	Plate 1	45.6	70.1	97.5	128.0
	Plate 2	11.5	17.5	24.4	32.0
3	Plate 1	102.7	138.5	177.3	219.4
	Plate 2	25.7	34.6	44.3	54.9
4	Plate 1	182.4	229.4	279.0	333.2
	Plate 2	45.6	57.4	69.8	83.3

Table E.2: Eigenfrequencies for 2 simply supported circular plates with a diameter of 50 mm (plate 1) and 100 mm (plate 2) and thickness of 0.26 mm. The mode i refers to the number of circular nodes j of the circular plate and the number of nodal diameters k .

Eigenfrequencies		[kHz]	[kHz]	[kHz]	[kHz]
Mode $i (j, k)$		1	2	3	4
1	Plate 1	5.7	16.1	29.5	46.1
	Plate 2	1.4	4.0	7.4	11.5
2	Plate 1	34.3	55.9	80.1	109.0
	Plate 2	8.6	14.0	20.2	27.3
3	Plate 1	85.5	118.5	154.8	194.5
	Plate 2	21.4	29.6	38.7	48.6
4	Plate 1	159.4	203.8	251.6	302.6
	Plate 2	39.9	51.0	62.9	75.7

Appendix F

Ultrasonic C-scans

The ultrasonic C-scans of the composite structures used for the experimental work are presented in this appendix. The ultrasonic C-scan of the front- and back-side of laminate 1 can be seen in figure F.1(a) and F.2(a). The thickness distribution of laminate 1 obtained with the delamination facing up and down can be seen in figure F.1(b) and F.2(b). The location of the delamination is for all the figures in this appendix the same as in figure F.3(a). Note that the delamination in figure F.1 and F.2 has the same intended center point but has a radius of $R = 25$ mm instead of $R = 50$ mm.

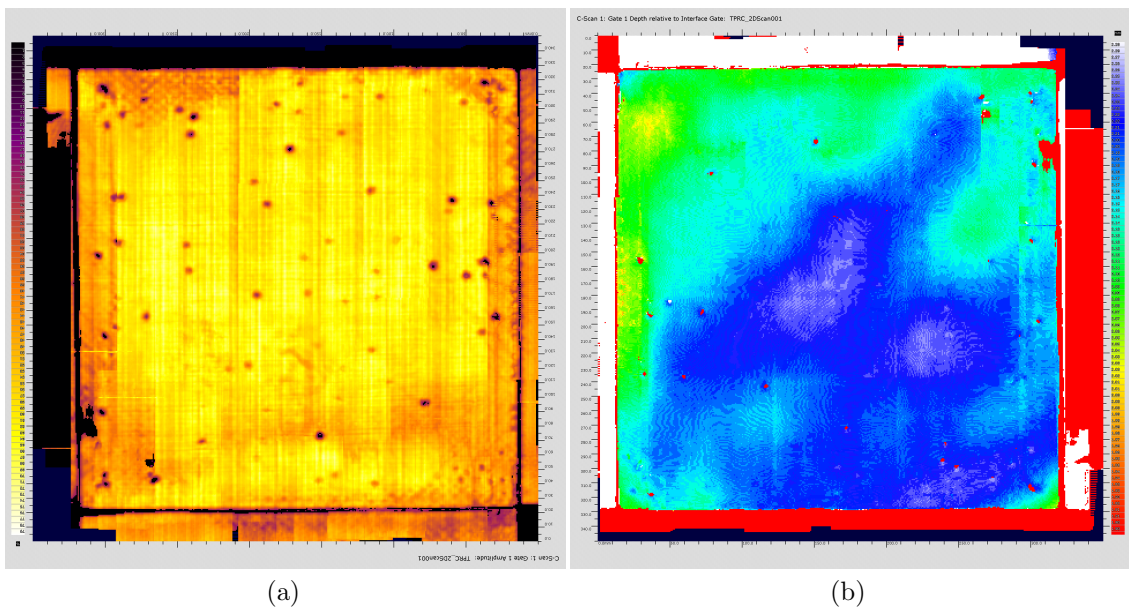


Figure F.1: Ultrasonic C-scan of laminate 1 (a) with a delamination of $R = 25$ mm and the thickness distribution (b) of Laminate 1.

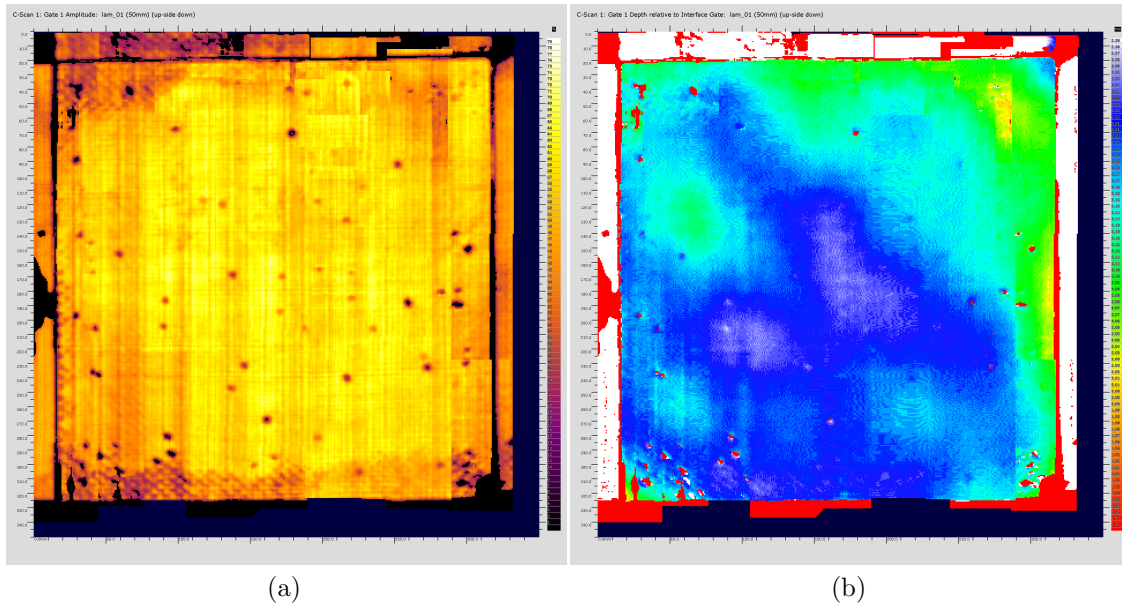


Figure F.2: Ultrasonic C-scan of laminate 1 (a) with a delamination of $R = 25$ mm and the thickness distribution (b) of Laminate 1. Both obtained when the delamination is faced downwards.

The ultrasonic C-scan of laminate 2 with the delamination facing upwards can be seen in figure F.3(a). The thickness distribution of laminate 2 obtained with the delamination facing up can be seen in figure F.3(b).

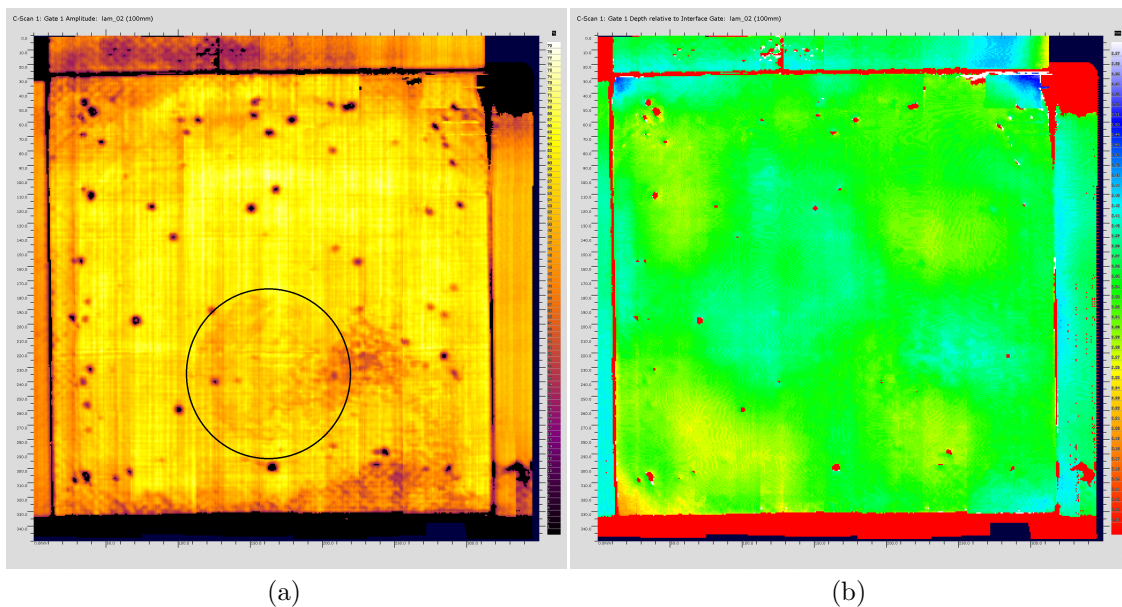


Figure F.3: Ultrasonic C-scan of laminate 2 (a) with a delamination of $R = 50$ mm and the thickness distribution (b) of Laminate 2.

Appendix G

Impedance Measurements

Traditional piezoelectric transducers (PZTs) are used for the permanent and direct attachment to an inspection structure. These are the most widely used sensors for structural health monitoring due to their low cost, low weight and convenience for majority of damage detection applications. The piezoelectric effect is an electric polarization effect that converts electric energy into mechanical strains and vice versa. So when a stress is applied on the material, an electrical charge can be found on its surface. This phenomenon has also an opposite effect, namely when a voltage is applied on the piezoelectric material, mechanical strains are generated. The transducer P-876.sp1 DuraAct Patch of Pi Ceramic used in this thesis can be seen in figure piezofig [34].

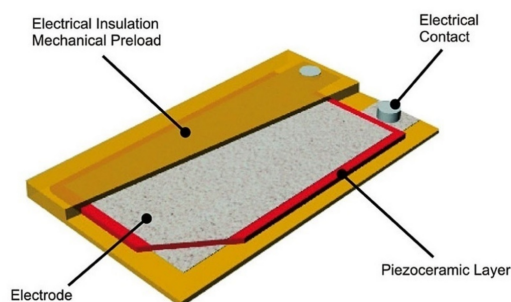


Figure G.1: PI Ceramic P-876.sp1 DuraAct patch transducer [34].

A piezoelectric sensor self-diagnostic procedure based on electrical impedance measurements can be used to judge the quality of the bond between transducer and structure [35, 36, 37, 38, 39]. The basis of this procedure is to track the changes in the capacitive value of piezoelectric materials, which is manifested in the imaginary part of the measured electrical admittances (inverse of impedance) [39]. By monitoring the imaginary part of the admittances, it is possible to quantitatively assess the breakage or degradation of the mechanical/electrical properties of the PZT sensors and the integrity of the bonding condition between a PZT and a host [39]. The susceptance spectrum which is the imaginary part of the admittance spectrum can also be used to judge the quality of the bond between transducers and structure in SHM systems [35, 36, 37, 38]. The focus in this thesis will be on the susceptance spectrum.

Reference data is made available by NLR that can be compared to the data obtained from the impedance measurements on the two different plates. The same piezoelectric transducers (PI P-876.SP1) are used by NLR, though the composite structure and the glue-process are different. The first adhesive used on the first panel is M-Bond 200, which is an alkyl-cyanoacrylate adhesive with operating temperatures below 70 degrees Celsius. This adhesive is primarily used for strain gages and polymerizes relatively fast. M-bond 200 has a low shearing strength in case a piece needs to be sheared off later, acetone and warm soapy water can also be used for softening cured cyanoacrylate. A different type of glue and structure will possibly have influence on the obtained impedance and susceptance spectra compared to the reference data of the NLR. The obtained susceptance spectra of the NLR reference data (black lines) and the susceptance spectrum of

plate 1 (red line) can be seen in figure G.2. Extra resonances can be seen around 0.5 MHz, which can be an indication of debonding [35, 42]. In the low frequency range 0.2-0.35 MHz noise can be seen, which is odd since noise for a broken transducer would normally occur in the higher frequency ranges. There is also an extra resonance here. These difference can also be caused due to the different composite structures, the different glue or a broken transducer. The latter is checked by capacity measurements and this is not the case.

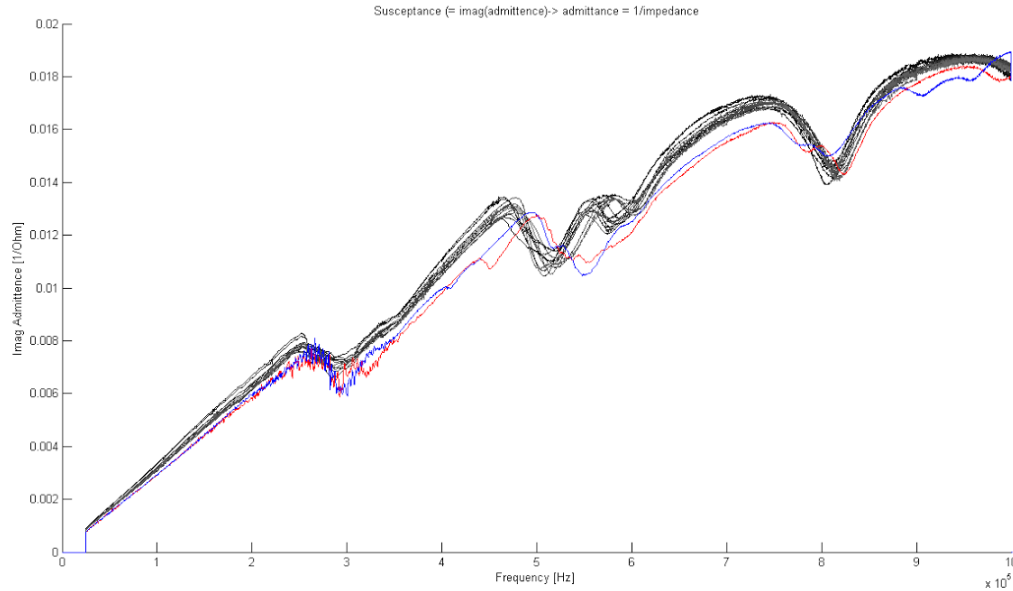


Figure G.2: Susceptance of the reference data (black), and of plate 1 (red) and 2 (blue).

For the second panel, the same glue (Loctite Hysol 9466) also used in the reference Data of the NLR is chosen. This is a 2 components epoxy-glye. The fixation time is a lot longer (180 minutes), such that a pressure can be applied on the piezoelectric transducer such that all the air in the glue layer can escape. The shear strength of $37 \frac{\text{N}}{\text{mm}^2}$ is higher compared to the M200 (around $20 \frac{\text{N}}{\text{mm}^2}$). These bonding strengths are dependent on the used substrates (materials), temperature and time and are therefore only a rough indication for our case. The obtained susceptance spectra of the NLR reference data (black lines) and the susceptance spectrum of plate 1 (red line) and 2 (blue line) can all be seen in figure G.2. The extra resonances around 0.3 MHz and 0.5 MHz is mostly gone and the line shifted towards the reference data. From this it can be concluded that the bonding on plate 2 is better than on plate 1, even though around 0.95 MHz the susceptance of plate 2 shows a different behavior than the reference data and the data of plate 1. Further research is needed to get a better understanding of the obtained results.

Appendix H

Dynamic characterization

The natural frequencies of two composite plate structures and the operational deflection shapes of some specific frequencies will be presented in this appendix. Not all the natural frequencies are determined due to limitations of the experimental equipment, the fixed excitation position and the limited amount of measuring points. The natural frequencies are listed in table H.1. Plate 1 has an artificial delamination with a diameter of 50 mm and plate 2 has an artificial delamination with a diameter of 100 mm. The latter is also the plate that is used in this master thesis.

Table H.1: Natural frequencies of two identical composite PEKK/AS4D plates $[0/90/45/-45]_{2,s}$ with two different artificial delamination sizes. In plate 1 the delamination has diameter of 50 mm and in plate 2 100 mm.

Mode	Exp f_B^n [Hz]		Exp f_T^n [Hz]	
n	Plate 1	Plate 2	Plate 1	Plate 2
1	-	-	-	-
2	-	-	-	-
3	365	356	464	501
4	389	425	485	523
5	427	457	783	855
6	583	633	904	965
7	642	685	-	-
8	-	-	-	-
9	757	812	-	-
10	1030	1110	-	-

The operational deflection shapes of the natural frequencies 523 Hz and 633 Hz of plate 2 are respectively given in figure H.1 and figure H.2.

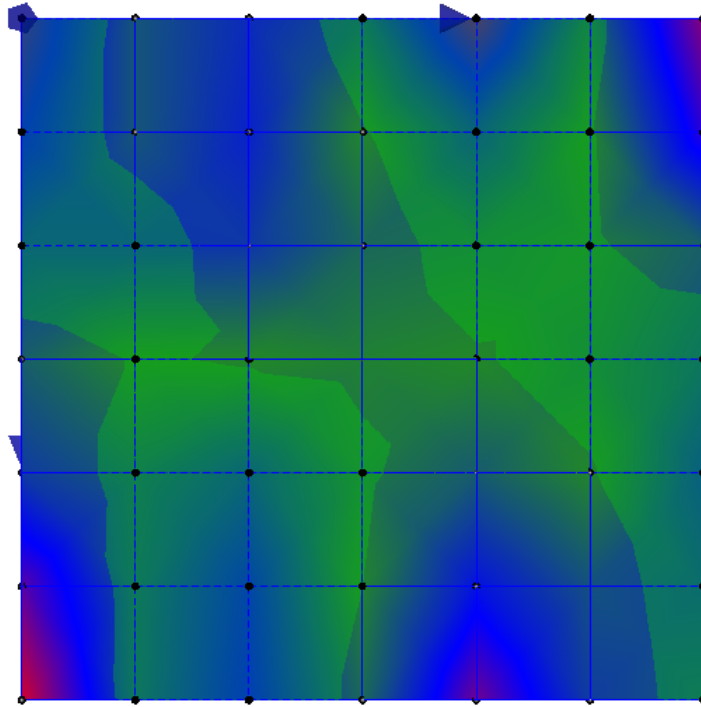


Figure H.1: Operational deflection shape of the natural frequency 523 Hz of plate 2.

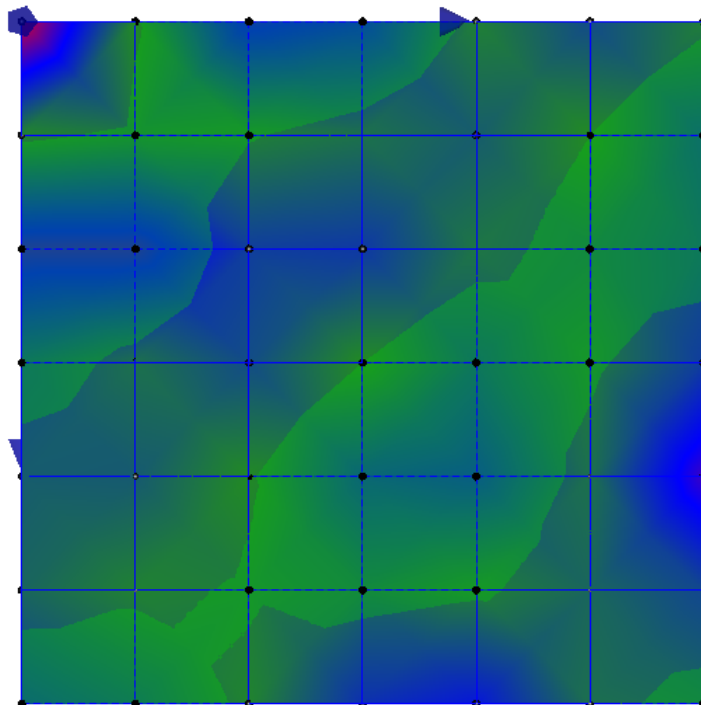


Figure H.2: Operational deflection shape of the natural frequency 633 Hz of plate 2.